**Intrinsic Electroresistance and Time Dependent Transport in Some Perovskite Manganites**

by

Shaikh Tawhid Mahmud

A thesis submitted in partial fulfillment of the requirements for the degree of

Doctor of Philosophy

Department of Physics

University of Alberta

# Abstract

This thesis studies the intrinsic disorder effects and the electro- and magneto-transport properties of some perovskite manganites. Recently reported colossal electro-resistance (ER) (a relative change in resistance with electric field /current ) in manganites, analogous to their respective colossal magnetoresistance (CMR) behavior, demonstrates another way of controlling the transport properties of manganites directly by using the electric current. In the last few years, there is considerable debate regarding the origin of this ER. In order to better understand this effect in some manganites, a technique for precisely measuring the intrinsic ER of a material has been developed and the technique has been utilized to measure the ER of polycrystalline $Sm_{0.60}Sr_{0.40}MnO_3$ and $Sm_{0.55}Sr_{0.45}MnO_3$ manganites. In this technique, the contribution of Joule heating to the ER has been successfully eliminated. It is found that the changes of the intrinsic ER with current density are much more significant in $Sm_{0.60}Sr_{0.40}MnO_3$ compared to $Sm_{0.55}Sr_{0.45}MnO_3$. We have also tuned the existing disorders/inhomogeneity in $Sm_{0.60}Sr_{0.40}MnO_3$ (SSMO) by Fe doping in Mn site to probe the possible mechanisms responsible for ER. It is found that ER increases with Fe doping and it is strongly suppressed by an applied dc magnetic field. A discussion of the mechanism behind these phenomena is presented.

We have investigated the time dependence of the electrical resistivity in the $Sm_{0.60}Sr_{0.40}Mn_{1-x}Fe_xO_3$, (1-$y$) $Sm_{0.60}Sr_{0.40}$ $MnO_3$ +$y$$BaTiO_3$ and $(Sm_{0.5}Gd_{0.5})_{0.55}$

$Sr_{0.45}Mn_{1-z}Ru_zO_3$ manganites by doping with Fe, $BaTiO_3$ and Ru to understand better the origin of relaxation effects and to learn how to control it. It is found that the relaxation effects strongly depend on the relative fraction of coexisting phases (for instance, ferromagnetic metallic (FMM), antiferromagnetic (AF) insulating with charge-orbital ordered (CO/OO) state, paramagnetic, etc.). We have shown that the relaxation effect in manganites can be controlled by using the doping element. The relaxation effects are enhanced due to both the Fe and $BaTiO_3$ doping in SSMO; however, they are suppressed by Ru substitution in $(Sm_{0.5}Gd_{0.5})_{0.55}Sr_{0.45}MnO_3$. The mechanism behind these changes in the relaxation effects is discussed.

We have also investigated the effect of strain induced disorder on the physical properties of $BaTiO_3/La_{0.66}Ca_{0.34}MnO_3$ heterostructure grown on a $SrTiO_3$ substrate where very thin (16 nm) $La_{0.66}Ca_{0.34}MnO_3$ films grown on $SrTiO_3$ are normally subjected to tensile strain. We found that this strain sensitive heterostructure has significant magnetocapacitance effect which is important for technological applications. A discussion of the mechanism behind this magnetocapacitance effect is introduced.

# Preface

The research presented in this thesis was carried out by me (**S. T. Mahmud**) in the Department of Physics at the University of Alberta under the supervision of Professors K. H. Chow and J. Jung.

Unless otherwise stated, all the material presented in this dissertation are based on my original work. Chapter 4 of this thesis has been published as **S. T. Mahmud**, M. M. Saber, H. S. Alagoz, R. Bouveyron, J. Jung, and K. H. Chow, "Intrinsic electroresistance of $Sm_{0.60}Sr_{0.40}MnO_3$ and $Sm_{0.55}Sr_{0.45}MnO_3$", Appl. Phys. Lett. **100**, 072404 (2012); **S. T. Mahmud**, M. M. Saber, H. S. Alagoz, J. Jung, and K. H. Chow, "Current density and intrinsic electroresistance of the $Sm_{1-x}Sr_xMnO_3$ manganite", Journal of Physics and Chemistry of Solids, **74**, 1865 (2013). Chapter 5 of this thesis has been published as **S. T. Mahmud**, M. M. Saber, H. S. Alagoz, K. Biggart, R. Bouveyron, Mahmud Khan, J. Jung, and K. H. Chow, "Disorder enhanced intrinsic electroresistance of $Sm_{0.60}Sr_{0.40}Mn_{1-y}Fe_yO_3$", Appl. Phys. Lett. **100**, 232406 (2012). I was responsible for synthesizing all the samples, making the new setup of the equipment to enable these measurements, writing essentially all of the relevant data acquisition software, collecting and analysing the data as well as the composition of these manuscripts. R. Bouveyron and K. Biggart helped me in pulverizing some solid sintered samples. M. M. Saber, H. S. Alagoz and Mahmud Khan assisted me in making silver contacts on the samples. My supervisors Professors K. H. Chow and J. Jung. were involved with concept formation and manuscript editing.

See Chapter 1 for the full list of publications of the author.

**To my parents and wife**

## Acknowledgements

I express my gratitude to my supervisors Dr. Kim. H. Chow and Dr. J. Jung for their constant direction and inspiration in pursuing the whole investigation of the present research. I am also grateful to Dr. Kim. H. Chow, Dr. J. Jung and Alberta Innovates - Technology Futures and Alberta Advanced Education & Technology for providing the financial grant for this research.

I wish to express my sincere thank to the members of my examining committee, professor Vadim A. Kravchinsky, professor Claire Currie, professor Thomas H. Etsell from University of Alberta, and professor R. Mahendiran from National University of Singapore for their invaluable comments and suggestions to prepare this thesis paper.

It is a pleasure for me to express my great thanks to all my research group members Dr. Mahmud Khan, Dr M. M. Saber, H. S. Alagoz, Jaechun Jeon and Mary Alven Narrato for their friendship, cooperation and helpful discussions.

I would like to thank Mr. Donald Mullin and Mr. Greg Popowich for their valuable technical support. I would like to extend my thanks to all Physics department staff and faculty, who have helped me directly and indirectly during my graduate studies.

Ultimately, I would mention a very special gratefulness for the moral support and sustaining inspiration provided by my wife, my parents and all the members of my family. This dissertation would never have been possible without their love and affection.

# Contents

# List of Figures

# Chapter 1

# Introduction

Manganites are strongly correlated electronic systems. The general formula of a manganite is $ReBO_3$, where Re is the trivalent rare earth element (Re=La, Sm, Pr etc.) and B is Mn. Pure manganites, $ReMnO_3$ are electrical insulators but hole doped manganites $Re_{1-x}Di_xMnO_3$ (where Di is a divalent alkaline earth elements (Ca, Sr etc.)) show fascinating magnetotransport properties such as a metal-insulator transition (MIT) and colossal magnetoresistance (CMR). CMR is a very large change in resistance by an application of external magnetic field and this phenomenon is of tremendous importance, both technologically and in terms of fundamental physics. The strong coupling interaction among spin, charge, lattice and orbital degrees of freedom in hole doped manganites give rise to a rich phase diagram with various types of electric and magnetic phases [1, 2, 3, 4]. Magnetoresistive manganite materials are considered potential candidates in development of next generation magnetic memory devices, magnetic-field sensors, magneto-electronic or spintronic devices [1].

## 1.1 Motivation and Objectives

The term *magnetoresistance* (MR) refers to the change in electrical resistance of a material due to the magnetic field. The relative change in the electrical resistance of a material produced by changing the magnitude of the electric field/current is known as *electroresistance* (ER); it is scientifically interesting and also has ramifications for applications such as those involving non-volatile memory elements [5, 6]. Recently reported Colossal ER in manganites [7], analogous to their respective MR behavior, demonstrates another way of controlling the transport properties of manganites directly by the electric field/current. In the last few years, there has been considerable debate regarding the origin of this ER [7, 8, 9, 10, 11, 12, 13, 14, 15]. This debate and the potential applicable properties of manganites are the primary motivation behind my study of the ER in manganites. By conducting this research I intended to improve the understanding of the origin of ER in some manganites. Secondly, *the time-dependent (relaxation) effect* ( a relative change in electrical resistance with time) in ER or CMR manganites influence their physical properties and may limit their technological applicability. Up to now, the underlying mechanism for controlling the relaxation effect in manganites is still unclear and more detailed understanding of the behavior of the relaxation effect is highly desirable for achieving reliable device operations. So, I also planned to investigate the time-dependent effects in some manganites. In addition, I attempted to synthesize multi-functional materials (for example, multiferroics (described below in section 1.1.3)) by combining manganites and ferroelectrics (described below in section 1.1.3), and investigate its physical properties.

In particular, this thesis concentrated on the effects of intrinsic disorder and the electrical and magnetic properties of some manganites with the objective of understanding the basic properties and controlling the properties which are suitable for applications. In the following sections, we expand on

the motivations behind our studies and discuss the specific objectives of the dissertation:

### 1.1.1 Investigating electroresistance in $Sm_{1-x}Sr_xMnO_3$

Doping $Re_{1-x}Di_xMnO_3$ by various trivalent (Re=La, Sm, Pr etc.) and divalent (Di=Ca, Sr etc.) elements lead to significant changes in their magnetic, electrical, and structural properties (see chapter 2, section 2.1 for details) [1, 2, 3, 4]. Among other manganites, due to the large mismatch in the ionic radii of $Sm^{3+}$ (1.132 Å) and $Sr^{2+}$ (1.310 Å), $Sm_{1-x}Sr_xMnO_3$ (SSMO) possesses a number of unique electronic and magnetic properties that makes it an important compound in the physics of doped manganites. $Sm_{1-x}Sr_xMnO_3$ with $x \sim 0.45$ composition shows the most abrupt metal to insulator transition (MIT), significant low field CMR, large magnetocaloric effects (MCE) and giant magnetostriction, that have made it a prominent candidate for low field magnetoresistive devices, bolometers and magnetic refrigeration [16, 17, 18, 19, 20, 21]. As can be seen in Fig. 1.1, $Sm_{1-x}Sr_xMnO_3$ exhibits a rich multi-critical phase diagram which includes ferromagnetic insulating (FMI), ferromagnetic metallic (FMM), paramagnetic insulating (PMI), antiferromagnetic insulating (AFI) as well as charge ordered/orbital ordered states and provides a natural tendency towards phase separation (PS) /coexistence [2, 22, 23, 24]. *Charge order* (CO) is an arrangement of the $Mn^{3+}$ and $Mn^{4+}$ charges in a periodic fashion (on specific lattice sites) that localizes electrons creating an AFI state [1, 4]. CO usually accompanies the orbital order (OO) (see chapter 2, section 2.5 for details). The *phase separation* (PS) phenomenon in manganites is the coexistence of two or more phases (for example, PMI, FMM and CO/OO AFI) with very different magnetic and transport properties (see chapter 2, section 2.6 for details), resulting from the strong coupling among spin, charge, lattice and orbital degrees of freedom [1, 2, 3, 4]. Depending on the composition ($x$), the dominant type of magnetic order is either ferromagnetic (FM)

($0.16 < x \leq 0.48$) or antiferomagnetic (AF) ($x > 0.48$). The region where the low field CMR effect could be observed accompanied with a MIT is relatively narrow ($0.3 < x < 0.52$). At low temperatures, the $x = 0.40$ sample has a phase-separated FMM ground state with A-type AF and small amounts of CE-type (charge ordered) AF clusters [22, 25, 26] whereas the low temperature ground state for $x = 0.45$ is a homogeneous FMM [22, 26].

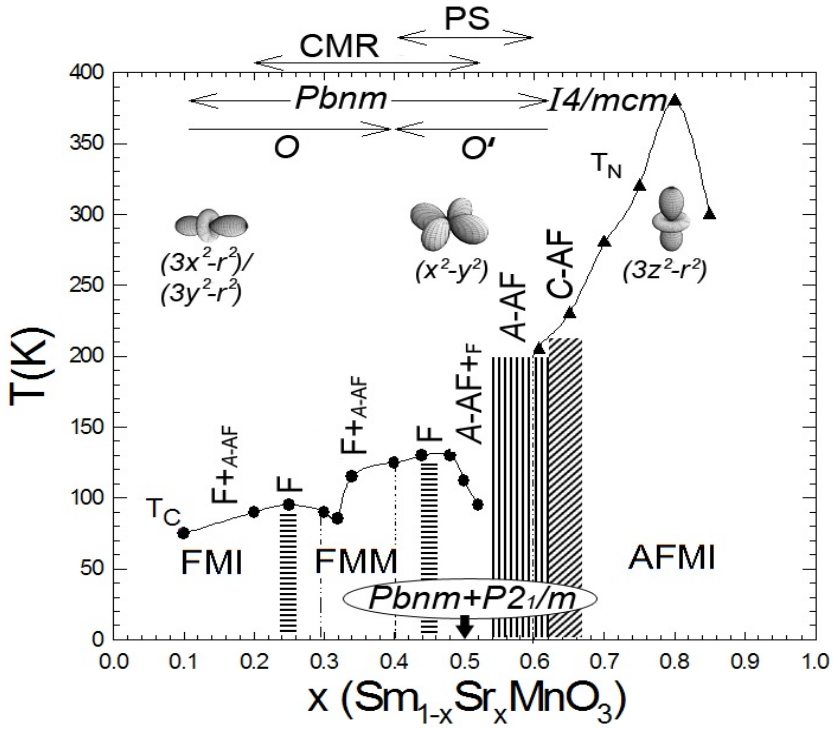


Figure 1.1: Structural and magnetic phase diagram of the $Sm_{1-x}Sr_xMnO_3$ system. Close circles and triangles correspond to the values of Curie temperatures ($T_C$) and Neel temperatures ($T_N$) from [23], respectively. The arrows at the top indicate the region of existence of CMR and phase separation (PS) [23]. The horizontal inscriptions indicate the types of the ground state as derived from macroscopic measurements in [23] ( FMM stands for ferromagnetic (FM) metal ; FMI, for FM insulator; and AFMI, for Antiferromagnetic (AF) insulator). The vertical inscriptions correspond to the neutron diffraction data: F is homogeneous FM; A-AF is A-type homogeneous AF; C-AF is C-type homogeneous AF; and F+$_{A-AF}$ and A-AF+$_F$ are phase separated magnetic systems with a mixture of FM and AF in which the FM and AF phases dominate, respectively. The dashed areas correspond to homogeneous magnetic states: FM (horizontal hatching), A-AF (vertical hatching), and C-AF (diagonal hatching). Different types of crystal structure orthorhombic Pbnm ( O and O$^/$)and tetragonal I4/mcm (at all temperatures) and a mixture orthorhombic Pbnm + monoclinic $P2_1/m$ (only at low temperatures) are also indicated by arrows. The supposed types of orbital ordering in AF phases $d_{3x^2-r^2}$ (or $d_{3y^2-r^2}$), $d_{x^2-y^2}$ and $d_{3z^2-r^2}$ are shown schematically. Figure is reproduced from [22].

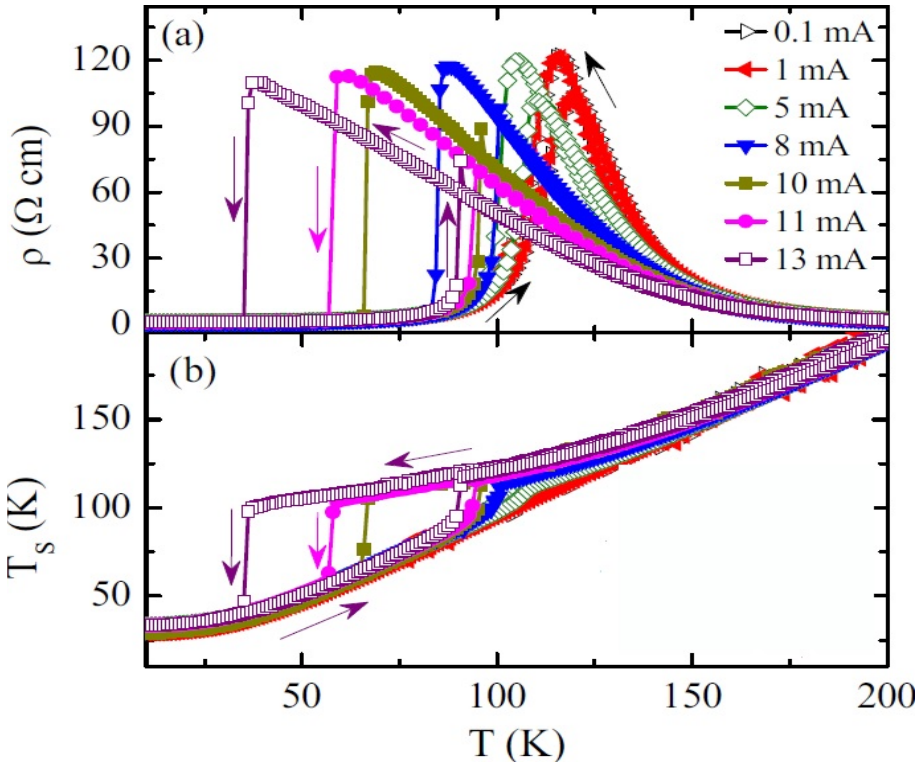


Figure 1.2: Temperature (T) dependence of the (a) resistivity for different dc current strengths (I) in zero magnetic field and (b) corresponding surface temperature $T_S$ of the $Sm_{0.60}Sr_{0.40}MnO_3$ reproduced from Ref. [15]. The arrows indicate the cooling and warming thermal cycles.

Asamitsu et al. [7] reported first the observation of colossal ER in $Pr_{0.70}Ca_{0.30}MnO_3$ (PCMO) charge ordered (CO) insulating sample ( in 1997) upon application of high voltage. Since then, the ER has been studied in various manganites [8, 9, 10, 11, 12, 13, 14, 15, 27, 28, 29, 30, 31, 32] under the electric field / current driven condition. Following the first report [7] related to the high electric field-induced melting of charge ordering in PCMO, several authors [11, 12, 13, 14, 15] suggested that Joule heating is important and could lead to a current-induced ER in manganites. Recently, interesting ER results were obtained by different teams on $Sm_{0.60}Sr_{0.40}MnO_3$ (Ref. [15]) and $Sm_{0.55}Sr_{0.45}MnO_3$ (Ref. [27]). Rebello *et al.* [15] used dc current to investigate polycrystalline $Sm_{0.60}Sr_{0.40}MnO_3$. They observed dramatic changes in the resistivity upon application of high current, including dramatic decreases

of metal to insulator transition temperature ($T_{MIT}$) (accompanied by significant heating at the surface of the sample) and hysteresis upon cooling and warming (see Fig. 1.2). They concluded that their results can be explained primarily by Joule heating. Mohan *et al.* [27] investigated the resistance of polycrystalline $Sm_{0.55}Sr_{0.45}MnO_3$ using pulsed current excitation, where the dc current was applied for a few milliseconds only. This method should drastically reduce any Joule heating [33] and enable measurements of the intrinsic ER. Intriguingly, they observed a giant reduction of the resistance in their sample of up to $\sim 2500\%$ at high currents (see Fig. 1.3), i.e. much higher than previous work on ER in many other manganites, including the investigations of $Sm_{0.60}Sr_{0.40}MnO_3$ described above.

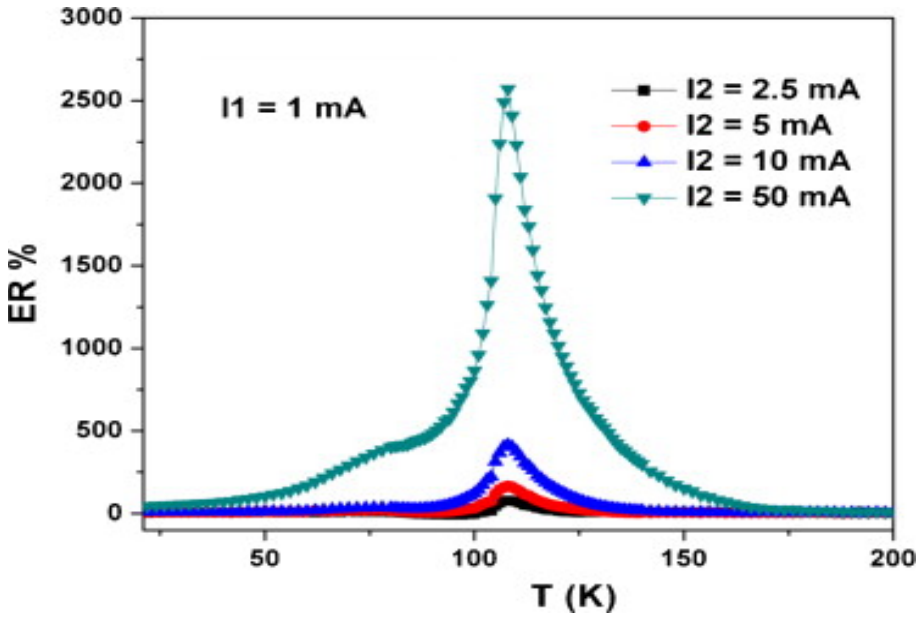


Figure 1.3: Temperature dependence of electroresistance (ER) with various currents for $Sm_{0.55}Sr_{0.45}MnO_3$ reproduced from Ref. [27]. The changes in the ER defined as $[(R(I1) - R(I2))/R(I2)] \times 100\%$.

In this thesis, a technique for precisely measuring the intrinsic ER of a material has been developed and the technique has been utilized to measure the ER of the two compositions of SSMO described above to address the following questions:(i) Are the giant changes of the intrinsic ER reported by Mohan et

al. [27] in $Sm_{0.55}Sr_{0.45}MnO_3$ reproducible? (ii) What is the intrinsic ER of $Sm_{0.60}Sr_{0.40}MnO_3$, i.e. without contribution of Joule heating, which has not yet been measured, and how does it compare with that of $Sm_{0.55}Sr_{0.45}MnO_3$? The knowledge of the values of the intrinsic ER in both compounds are especially relevant if one recognizes that according to recent studies [22, 25, 26] described above, $Sm_{1-x}Sr_xMnO_3$ $x = 0.40$ and 0.45 are believed to have different phase separated magnetic (and hence transport) ground states (see Fig. 1.1 for a phase diagram of $Sm_{1-x}Sr_xMnO_3$), which may, therefore, have noticeably different effects on the intrinsic ER.

As we will discuss in Chapter 4, from the investigations of SSMO [34], we found that the changes of the intrinsic electroresistance with current density are much more significant in $Sm_{0.60}Sr_{0.40}MnO_3$ compared to $Sm_{0.55}Sr_{0.45}MnO_3$, suggesting that spatial inhomogeneities related to the multiphase coexistence are important in determining the intrinsic ER in SSMO. This conclusion led us to initiate more study on the existing disorders/inhomogeneity in $Sm_{0.60}Sr_{0.40}$ $MnO_3$ by chemical doping to further investigate the possible mechanisms responsible for ER. These studies are described in Chapter 5.

### 1.1.2 Investigating relaxation effects

Several authors [35, 36, 37, 38] have observed and studied the temperature dependent relaxation rate of resistivity in various manganite samples (that show MIT). Most of them focused on temperatures around the MIT of samples and reported the observation of strong resistive relaxation (huge increase/decrease of resistivity with time) in this temperature range. Fig. 1.4 (Ref. [36]) is an example of time dependent resistivity measurement at several temperatures carried out on a $Nd_{0.5}Ca_{0.5}Mn_{0.93}Cr_{0.07}O_3$ single crystal. The sample exhibits a pronounced relaxation near the MIT ( $T_{MIT} \sim 145$K), corresponding to a maximum increase of $\sim$ 28% of the initial resistivity (see Fig. 1.4). Carneiro et al. [36] explained that the system can change easily be-

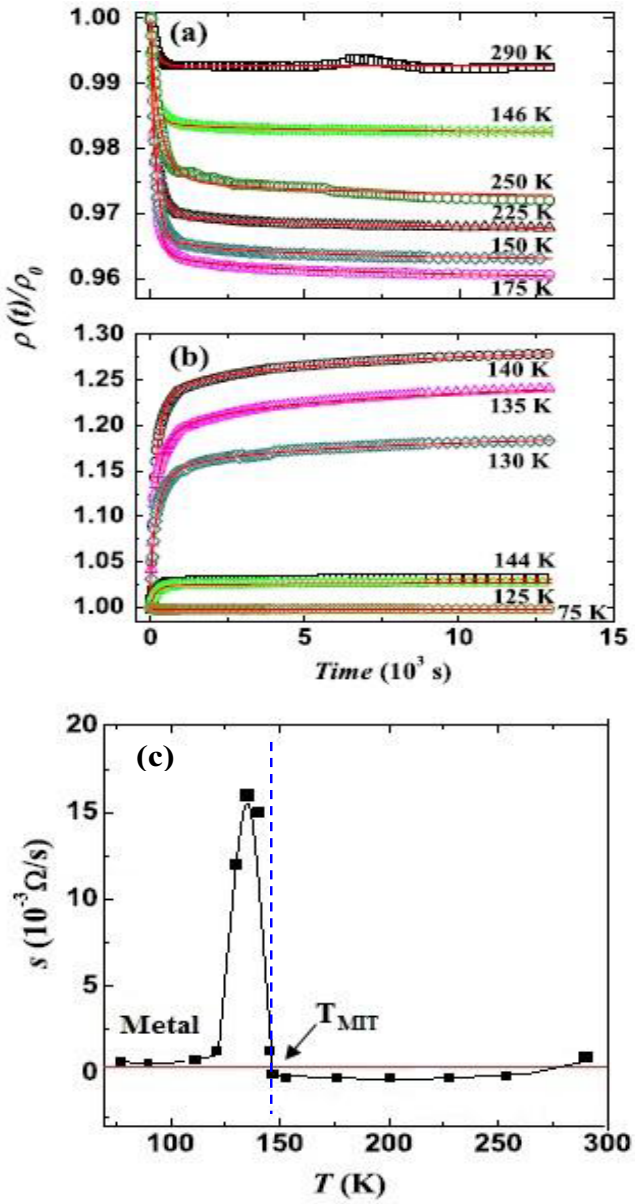


Figure 1.4: (a) and (b): Normalized isothermal electrical resistivity ($\rho(t)/\rho_0$) relaxation versus time (t) of $Nd_{0.5}Ca_{0.5}Mn_{0.93}Cr_{0.07}O_3$ single crystal at several temperatures. $\rho_0$ is the initial electrical resistivity.(c) Temperature dependence of resistive relaxation rate, S(T). The solid lines in Fig. (a) and (b) are the best fittings using equation $\rho(T,t) = \rho_0 + A(1 - exp(-t/\tau(T)) + S(T)ln(t)$,where $A$ is a free parameter, $\tau$ is the temperature-dependent relaxation time and S is relaxation rate of resistivity. The horizontal line (red) in Fig.(c) indicates S= 0. The vertical dotted line (blue) in Fig.(c) separates the S(T) obtained from Fig. (a) and Fig. (b). Figures are reproduced from Ref. [36].

tween both FM and charge ordered (CO) AF phases close to MIT, due to the small energy barrier between them. The sign (positive/negative) of the resistive relaxation determines the dominating electric phases (metallic/insulating). Later Huang et al. [38] reported the observation of intense negative resistive relaxation (resistivity decreases with time) at low temperature (T) in the metallic state of the $La_{0.67}Ca_{0.33}MnO_3/NdGaO_3$ sample as well as positive resistive relaxation (resistivity increases with time) close to the MIT (see Fig. 1.5). They concluded that the mobilities of the phase boundaries in the high temperature range (near the MIT) change the phase fraction and are responsible for strong relaxation in resistivity. However, the origin of these large resistive relaxation in the metallic state for low temperatures ($T \ll T_{MIT}$) is not well understood, and unfortunately, experiments have not confirmed explicitly the mechanism for controlling these relaxation effect in manganites.

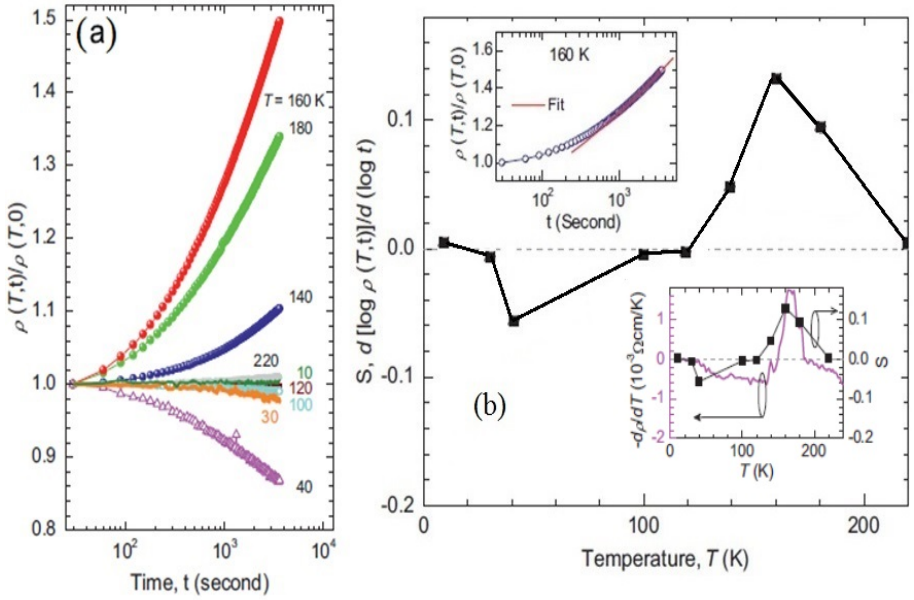


Figure 1.5: (a) The variation of normalized resistivity ($\rho(T,t)/\rho(T,0)$) as a funtion of time (t) for 40 nm $La_{0.67}Ca_{0.33}MnO_3/NdGaO_3$ film for various temperatures. (b) The variation of logarithmic resistive relaxation rate, S (defined as $S(T) = dlog\rho(T,t)/dlog(t)$) as a function of temperature (T), which are derived from the data of Fig.(a). The top inset shows an example for fitting the data at 160K. The bottom inset shows $-d\rho/dT$ and S vs T. Figures are reproduced from Ref. [38].

As discussed in section 1.1.1, SSMO shows some distinct electric and magnetic properties compared to other manganites, which make it an important candidate for many applications. To the best of our knowledge, time dependent electric property has not been studied before for this important composition. In our experiment discussed in this thesis (Chapter 6), we doped SSMO manganite by various chemical elements, and we subsequently studied the relaxation of resistivity of the system including the parent SSMO, to investigate how the doping elements modify the metastability of the SSMO manganite. The chemical doping elements can influence the disorder-induced phase separation and may alter the physical properties of manganites. These relaxation studies and the doping compositions are discussed in more detail in chapter 6.

### 1.1.3 Investigating multiferroic property

*Ferroelectric* materials possess a spontaneous electric polarization (P) that can be reversed hysteretically by an applied electric field (E) , whereas *ferromagnetic* materials possess a spontaneous magnetization (M) that can be reversed hysteretically by an applied magnetic field (H) (see Fig. 1.6). The electric charges of electrons and ions and the spontaneous ordering of electric dipole moments are generally responsible for ferroelectricity, whereas electron spins govern magnetic properties. *Multiferroic* materials exhibit more than one primary ferroic order (such as ferroelectricity and ferromagnetism ) simultaneously. In a multiferroic material a cross-coupling between magnetic and electric orders, the so-called *magneto-electric* (ME) coupling, allows the ferroelectric polarization to be controlled with changes in the magnetic field and vice versa, the magnetization to be controlled with changes in the electric field [39, 40, 41](see Fig. 1.6). Materials that exhibit both ferroelectric and magnetic , i.e. multiferroic, properties are rare. Besides the scientific interest in their physical properties, multiferroics are potential candidates for new applications/devices, including sensors, data storage, transducers, multistate

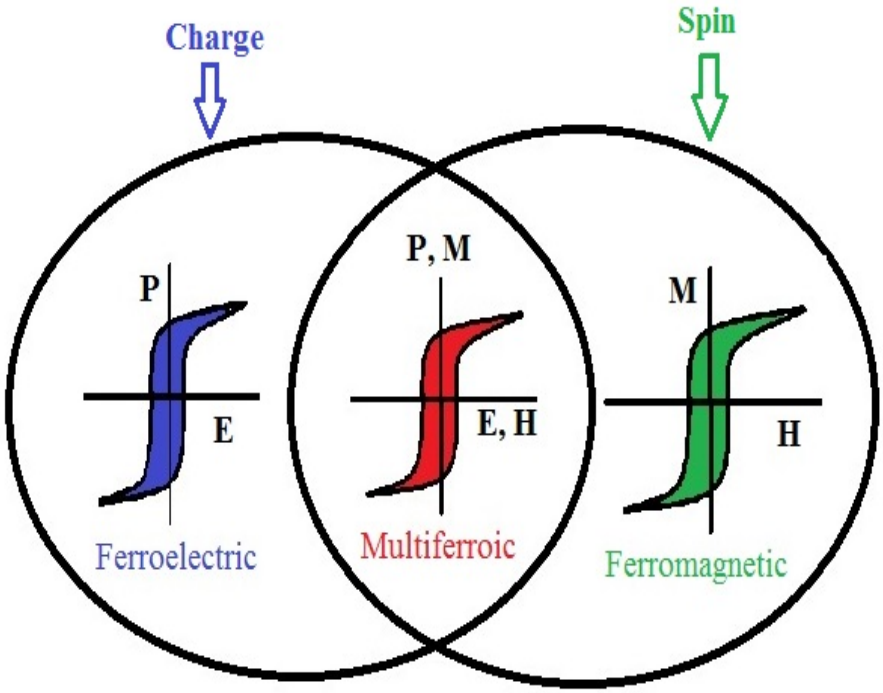


Figure 1.6: Schematic diagram: polarization (P) vs electric field (E) hysteresis loop (blue) for ferroelectric material, and magnetization (M) vs magnetic field (H) (green) for ferromagnetic material. Multiferroics (red) combine the properties of ferroelectrics and ferromagnetics. In multiferroic material, the electric polarization can be controlled by the application of magnetic field or vice versa, the magnetization can be modified by the electric field. See text for detail.

memories, or memories with dual read-write mechanism [39, 40, 41, 42, 43].

The single-phase multiferroics exhibit weak ME effects [41, 44]. However, the ME effects may be significantly enhanced in the composites of ferromagnetic and ferroelectric phases [43]. Barium titanate ($BaTiO_3$) is a lead (Pb) free non-toxic and very widespread room temperature ferroelectric material often used as a dielectric material in capacitors and energy storage devices owing to its low loss and high dielectric constant ($\varepsilon \sim 4 \times 10^3$)(The ratio between the capacitance of a material (C) and the capacitance of a vacuum ($C_0$) is called the *dielectric constant* ($\varepsilon = C/C_0$))[45, 46, 47]. Moreover, the $BaTiO_3$ ferroelectic has a simple perovskite structure that can be a promising candi-

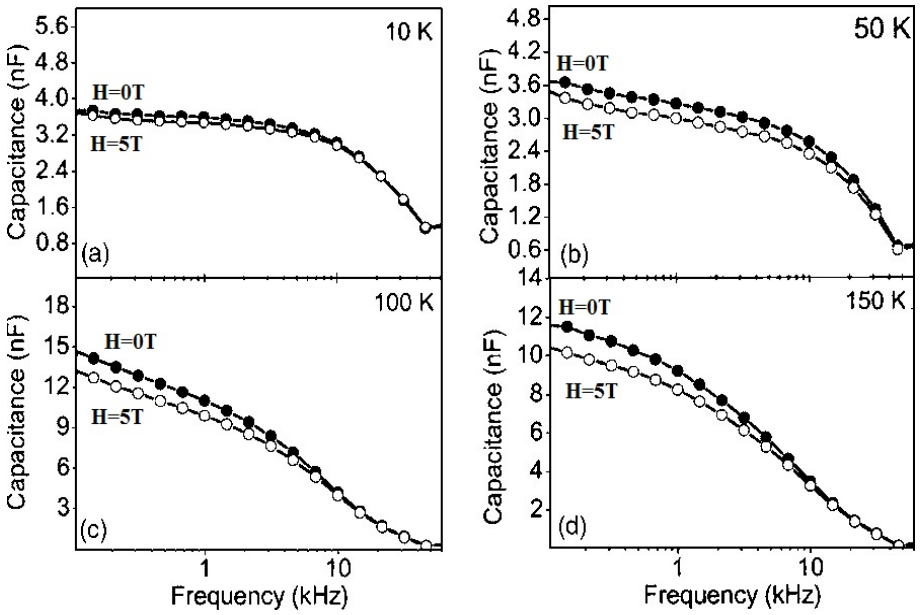


Figure 1.7: Capacitance (C) vs frequency with applied magnetic field (H) of a $BaTiO_3/La_{0.70}Ca_{0.30}MnO_3$ superlattice at (a) 10 K, (b) 50 K, (c) 100 K, and (d) 150 K. Full dots: H= 0 T, open dots: H= 5 T. Figures are reproduced from Ref. [48].

date for multiferroic heterostructure composed of ferroelectric and perovskite manganite. Singh et al. [48] investigated the magnetoelectrical properties of $BaTiO_3/La_{0.70}Ca_{0.30}MnO_3$ superlattices grown on an $SrTiO_3$ substrate. Note that a ferroelectic sample (for example, $BaTiO_3$) does not show any change in capacitance with an applied magnetic field. *The change in capacitance (or dielectric constant) due to the magnetic field is called the magnetocapacitance* [48, 49] of the sample, and this magnetocapacitance effect is usually used to determine whether or not a material is a multiferroic. They observed a negative magnetocapacitance (MC) effect (see Fig. 1.7) as well as negative magnetoresistance (MR) upon application of magnetic field (where MC and MR are calculated using the formula $MC(\%) = ((C(H) - C(H = 0T))/(C(H = 0T)) \times 100\%$ and $MR(\%) = ((R(H) - R(H = 0T))/R(H = 0T)) \times 100\%$, C(H) and R(H) are the capacitance and resistance measured with magnetic field (H) respectively). They concluded that the coupling between magnetic and dielec-

tric orders gave rise to this negative MC effect in the superlattice-based oxide multiferroic.

Later, Catalan et al.[49] reported that large MC effects can be achieved by combining $BaTiO_3$ with manganite layers through a combination of magnetoresistance and the Maxwell-Wagner effect (Charge can build-up at the two material interfaces due to different permitivity and conductivity with different relaxation times. When an alternating electromagnetic field is applied to the system, an extra dielectric relaxation is caused by the oscillatory shifts of these charge carriers inside the system, known as the *Maxwell-Wagner effect* [50]). Fig. 1.8 presents a brief description accompanying an illustration for Maxwell-Wagner (M-W) equivalent circuit model of a heterogeneous lossy dielectric. The possibility of a sizable magnetocapacitance in the magnetoresistive multilayers (artificial multiferroics) can make it a potential candidate for multifunctional sensors. They also reported (based on M-W theoretical model: two leaky capacitors in series with one of the leakage components being magnetically tunable) that negative magnetoresistive manganite layer can produce positive MC effect for the sample combining $BaTiO_3$ (BTO) and ferromagnetic manganite layers (see Fig. 1.8), which is opposite in sign to the result (MC effect) reported by Singh et al [48]. This contradictory results and potential applications of multiferroics, therefore, motivate us to synthesize and investigate the physical properties of strain sensitive nanometer (nm) thick epitaxial BTO-manganite multilayers that display significant multiferroic properties. These are discussed in more detail in chapter 7.

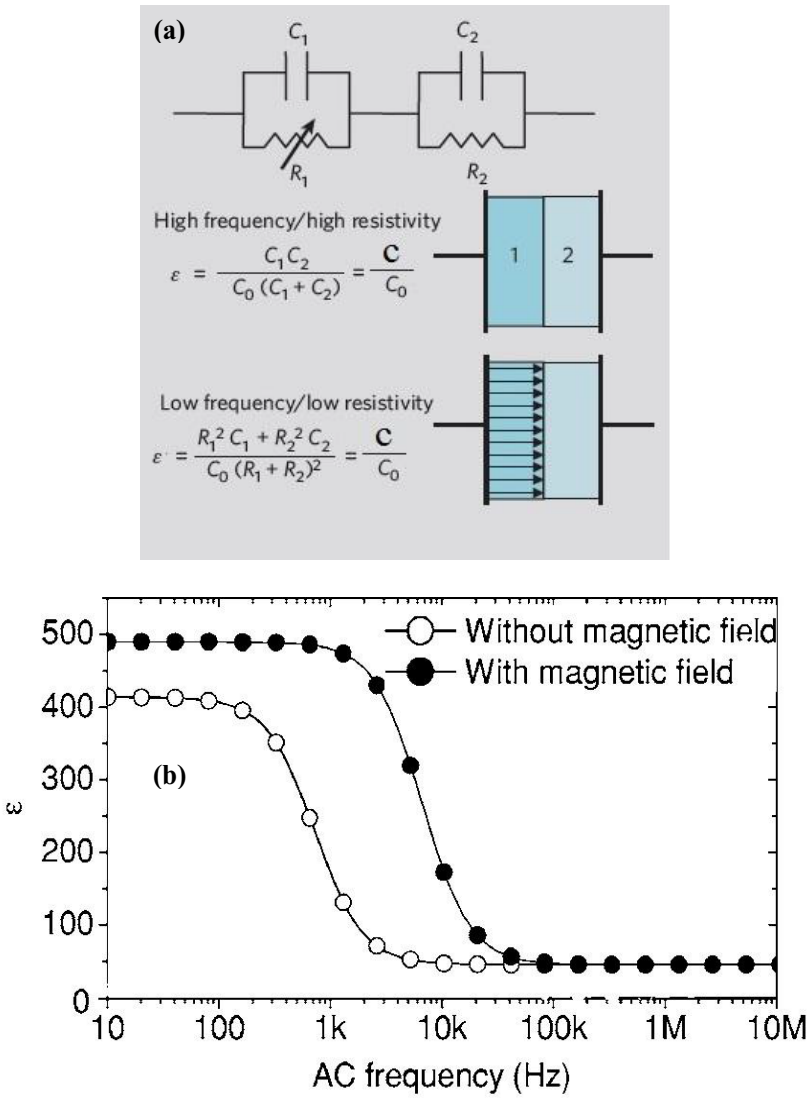


Figure 1.8: (a) Capacitor system with magnetoresistive Maxwell-Wagner behavior: two leaky capacitors in series with one of the leakage components being magnetically tunable. The model shows approximated equations for the apparent dielectric constant ($\varepsilon = C/C_0$) at high and low frequencies of alternating current. C is the measured capacitance of the materials and $C_0$ is the capacitance of vacuum. At high frequencies, the two types of region act as two capacitors ($C_1$ and $C_2$ ) in series . The effect of lowering the frequency is the same as that of decreasing the resistance (R) of one of the two components: it allows the current (arrows) to flow through, reducing the apparent thickness and increasing the measured capacitance (C). In the superlattice consisting of ferroelectric $BaTiO_3$ and a magnetoresistive manganite, applying a magnetic field has the same effect on capacitance as reducing the frequency. (b) Calculated dielectric constant, $\varepsilon$, as a function of frequency for a superlattice consisting of ferroelectric $BaTiO_3$ and a magnetoresistive manganite. Figures are reproduced from Ref. [49, 51].

## 1.2 Thesis organization

The format of the thesis is as follows:

*Chapter 1* describes the motivation and goals of this dissertation.

*Chapter 2* gives a brief overview of manganite materials.

*Chapter 3* describes the details of samples preparation method and the experimental-setup.

*Chapter 4* describes a technique for measuring the intrinsic ER and the way the technique is applied to measure the ER properties of $Sm_{0.60}Sr_{0.40}MnO_3$ and $Sm_{0.55}Sr_{0.45}MnO_3$. The experimental results for these two compositions are discussed. The controlling parameter for analyzing intrinsic ER is also discussed.

*Chapter 5* describes tuning the inhomogeneity/disorder in these manganites to probe the possible mechanisms responsible for ER.

*Chapter 6* deals with the disorder controlled time dependent electrical transport in doped $Sm_{0.60}Sr_{0.40}MnO_3$ and $(Sm_{0.5}Gd_{0.5})_{0.55}Sr_{0.45}MnO_3$ manganites.

*Chapter 7* describes the magnetocapacitance in the epitaxial $BaTiO_3/La_{0.66}Ca_{0.34}MnO_3$ heterostructure.

The conclusions drawn from the experimental results and discussion are presented in *Chapter 8*.

## 1.3 List of Publication

1. **S. T. Mahmud**, M. M. Saber, H. S. Alagoz, J. Jung, and K.H. Chow, *Current density and intrinsic electroresistance of the $Sm_{1-x}Sr_xMnO_3$ manganite*, Journal of Physics and Chemistry of Solids, **74**, 1865 (2013).

2. **S. T. Mahmud**, M. M. Saber, H. S. Alagoz, K. Biggart, R. Bouveyron, Mahmud Khan, J. Jung, and K.H. Chow, *Disorder enhanced intrinsic electroresistance of $Sm_{0.60}Sr_{0.40}Mn_{1-y}Fe_yO_3$*, Appl. Phys. Lett. **100**, 232406 (2012).

3. **S. T. Mahmud**, M. M. Saber, H. S. Alagoz, R. Bouveyron, J. Jung, and K.H. Chow, *Intrinsic electroresistance of $Sm_{0.60}Sr_{0.40}MnO_3$ and $Sm_{0.55}Sr_{0.45}MnO_3$*, Appl. Phys. Lett. **100**, 072404 (2012).

4. H. S. Alagoz, J. Jeon, **S. T. Mahmud**, M. M. Saber, B. Prasad, , M. Egilmez, K. H. Chow and J. Jung, *Recovery of oscillatory magneto-resistance in phase separated $La_{0.3}Pr_{0.4}Ca_{0.3}MnO_3$ epitaxial thin films*, Appl. Phys. Lett. **103**, 232402 (2013).

5. H. S. Alagoz, I. Zivkovic, **S. T. Mahmud**, M. M. Saber, G. Perrin, J. Shandro, Mahmud Khan, Y. Zhang, M. Egilmez, J. Jung, and K. H. Chow, *Competing A-site and B-site doping effects on magneto-transport of $RE_{0.55}Sr_{0.45}Mn_{1-x}Ru_xO_3$ manganites in the vicinity of the SGI and FMM border*, Physica Status Solidi B, **250**, 2158 (2013).

6. H. S. Alagoz, Mahmud Khan , M. M. Saber , **S. T. Mahmud**, K. H. Chow, and J. Jung, *Influence of A-site doping and strain on the relationship between the AMR and charge localization in films of $La_{0.7-x}Pr_xCa_{0.3}MnO_3$ manganites*, Appl. Phys. Lett. **102**, 242406 (2013).

7. A. K. M. Akther Hossain, T. S. Biswas, **S. T. Mahmud**, Takeshi Yanagida, Hidekazu Tanaka, and Tomoji Kawai, *Enhancement of initial permeability due to Mn substitution in polycrystalline $Ni_{0.5-x}Mn_xZn_{0.5}Fe_2O_4$*, Journal of Magnetism and Magnetic Materials **321**, 81 (2009).

8. A. K. M. Akther Hossain, T. S. Biswas, **S. T. Mahmud**, Takeshi Yanagida, Hidekazu Tanaka, and Tomoji Kawai, *Influence of Mg and Cr substitution on structural and magnetic properties of* $Ni_{0.5}Zn_{0.5-x-y}Mg_xCr_yFe_2O_4$, Materials Chemistry and Physics **113**, 172 (2009).

9. A. K. M. Akther Hossain, **S. T. Mahmud**, M. Seki, T. Kawai, and H. Tabata, *Structural, Electrical transport and Magnetic Properties of* $Ni_{1-x}Zn_xFe_2O_4$, Journal of Magnetism and Magnetic Materials **312**, 210 (2007).

10. **S. T. Mahmud**, A. K. M. Akther Hossain, A. K. M. Abdul Hakim, M. Seki, T. Kawai, and H. Tabata, *Influence of microstructure on the complex permeability of spinel type Ni-Zn ferrite*, Journal of Magnetism and Magnetic Materials **305**, 269 (2006).

11. M. L. Rahman, M. H. R. Khan, **S. T. Mahmud**, and A. K. M. Akther Hossain, *Sintering temperature dependent permeability of nanocrystal line* $Ni_{0.20}Cu_{0.30}Zn_{0.50}Fe_2O_4$ *ferrite*, Journal of Bangladesh Academy of Sciences, **35**, 67 (2011).

12. M. L. Rahman, **S. T. Mahmud**, and A. K. M. Akther Hossain, *X-ray Studies and Magnetic Properties of Ni-Cu-Zn Ferrite*, BRAC University Journal, **7**, 9 ( 2010).

13. **S. T. Mahmud**, A. K. M. A. Islam, and F. N. Islam, $VB_2$ *and* $ZrB_2$*: a density functional study*, Journal of Physics: Condensed Matter **16**, 2335 (2004).

# Bibliography


[1] T. Chatterji, Colossal Magnetoresistive Manganites, Kluwer Academic Publishers, (2004).

[2] Y. Tokura, Rep. Prog. Phys. **69** 797 (2006).

[3] E. Dagotto, T. Hotta, and A. Moreo, Phys. Rep. **344**, 1 (2001).

[4] C. N. R. Rao and P. V. Vanitha, Curr. Opin. Solid State Mater. Sci. **6**, 97 (2002).

[5] A. Odagawa, T. Kanno, H. Adachi, H. Sato, I. H. Inoue, H. Akoh, M. Kawasaki, and Y. Tokura, Thin Solid Films **486**, 75 (2005).

[6] Y. Nishi, Current Applied Physics **11**, e101 (2011).

[7] A. Asamitsu, Y. Tomioka, H. Kuwahara, and Y. Tokura, Nature **388**, 50 (1997).

[8] Y. Yamato, M. Matsukawa, Y. Murano, R. Suryanarayanan, S. Nimori, M. Apostu, A. Revcolevschi, K. Koyama, and N. Kobayashi, Appl. Phys. Lett. **94**, 092507 (2009).

[9] H. Jain and A. K. Raychaudhuri, Appl. Phys. Lett. **93**, 182110 (2008).

[10] A. Rebello and R. Mahendiran, Appl. Phys. Lett. **94**, 112107 (2009).

[11] A. A. Wagh, P. S. A. Kumar, H. L. Bhat, and S. Elizabeth, J. Appl. Phys. **108**, 063703 (2010).

[12] Y. F. Chen, M. Ziese, and P. Esquinazi, Appl. Phys. Lett. **88**, 222513 (2006).

[13] A. S. Carneiro, R. F. Jardim, and F.C. Fonseca, Phys. Rev. B **73**, 012410 (2006).

[14] S. Mercone, R. Frésard, V. Caignaert, C. Martin, D. Saurel, C. Simon, G. André, P. Monod, and F. Fauth, J. Appl. Phys. **98**, 023911 (2005).

[15] A. Rebello and R. Mahendiran, Appl. Phys. Lett. **96**, 152504 (2010).

[16] S. T. Mahmud, M. M. Saber, H. S. Alagoz, J. Jung, and K. H. Chow, J. Phys. Chem. Solids **74**, 1865 (2013).

[17] M. Egilmez, M. Abdelhadi, Z. Salman, K. H. Chow, and J. Jung, Appl. Phys. Lett. **95** 112505 (2009).

[18] N. S. Bingham, P. J. Lampen, T. L. Phan, M. H. Phan, S. C. Yu, and H. Srikanth, J. Appl. Phys. **111** 07D705 (2012).

[19] M. K. Srivastava, M. P. Singh, A. Kaur, F. S. Razavi, and H. K. Singh, J. Appl. Phys. **110** 123922 (2011).

[20] A. Rebello, and R. Mahendiran, Appl. Phys. Lett. **93** 232501 (2008).

[21] A. I. Abramovich, L. I. Koroleva and A. V. Michurin, J. Phys.: Condens. Matter **14** L537 (2002).

[22] A. I. Kurbakov, J. Magn. Magn. Mater. **322**, 967 (2010); A. I. Kurbakov, A.V. Lazuta, and V. A. Ryzhov, J. Phys.: Conf. Ser. **200**, 012099 (2010).

[23] C. Martin, A. Maignan, M. Hervieu, and B. Raveau, Phys. Rev. B **60**, 12191 (1999).

[24] M. K. Srivastava, M. P. Singh, P. K. Siwach, A. Kaur , F. S. Razavi , H. K. Singh, Solid State Commun., **152** 138 (2012).

[25] I. D. Luzyanin, V. A. Ryzhov, D. Yu. Chernyshov, A. I. Kurbakov, V. A. Trounov, A. V. Lazuta, V. P. Khavronin, I. I. Larionov, and S. M. Dunaevsky, Phys. Rev. B **64**, 094432 (2001).

[26] A. I. Kurbakov, A. V. Lazuta, V. A. Ryzhov, V. A. Trounov, I. I. Larionov, C. Martin, A. Maignan, and M. Hervieu, Phys. Rev. B **72**, 184432 (2005).

[27] R. Mohan, N. Kumar, B. Singh, N. K. Gaur, S. Bhattacharya, S. Rayaprol, A. Dogra, S. K. Gupta, S. J. Kim, and R. K. Singh, J. Alloys and Compd. **508**, L32 (2010).

[28] P. S. Devi, A. Kumar, D. Bhattacharyay, S. Karmakar, and B. K. Chaudhuri, Jpn. J. Appl. Phys. **49** 083001 (2010).

[29] S. Y. Wang, and J. Gao, EPL **97** 57009 (2012).

[30] R. A. Lewis, Appl. Phys. Lett. **92** 184102 (2008).

[31] A. Kumar and J. Dho, J. Appl. Phys. **110**, 093901 (2011).

[32] N. Kambhala, P. Viswanath, and S. Angappane, Appl. Phys. Lett. **103** 102408 (2013).

[33] B. Fisher, J. Genossar, K. B. Chashka, L. Patlagan, and G. M. Reisner, Appl. Phys. Lett. **88**, 152103 (2006).

[34] S.T. Mahmud. M. M. Saber, H. S. Alagoz, R. Bouveyron, J. Jung, and K.H. Chow, Appl. Phys. Lett. **100**, 072404 (2012).

[35] X. J. Chen, H.-U. Habermeier, and C. C. Almasan, Phys. Rev. B **68**, 132407 (2003).

[36] A. S. Carneiro, F. C. Fonseca, T. Kimura, and R. F. Jardim, J. Phys.: Condens. Matter **20**, 215203 (2008).

[37] M. Quintero, F. Parisi, G. Leyva1, and L. Ghivelde, J. Phys.: Condens. Matter **20**, 345204 (2008).

[38] Z. Huang, G. Gao, F. Zhang, X. Feng, L. Hu, X. Zhao, Y. Sun, W. Wua, J. Magn. Magn. Mater. **322** 3544 (2010).

[39] R. Ramesh, and N. A. Spaldin, Nature Mater. **6**, 21 (2007).

[40] C. A. F. Vaz, J. Phys.: Condens. Matter. **24**, 333201 (2012).

[41] S.-W. Cheong, and M. Mostovoy, Nature Mater.**6**, 13 (2007).

[42] H. Béa, M. Gajek, M. Bibes, and A. Barthélémy, J. Phys.: Condens. Matter. **20**, 434221 (2008).

[43] G. Srinivasan, E. T. Rasmussen, J. Gallegos, R. Srinivasan, Yu. I. Bokhan, and V. M. Laletin, Phys. Rev. B **64**, 214408 (2001).

[44] J. Ma , J. M. Hu , Z. Li , and C.-W. Nan, Adv. Mater.**23**, 1062 (2011).

[45] M. M. Vijatović, J. D. Bobić, B. D. Stojanović, Science of Sintering, **40**, 235 (2008).

[46] G. H. Kwei, A. C. Lawson, S. J. L. Billinge and S.-W. Cheong, J. Phys. Chem. **97**, 2368 (1993).

[47] K. Kinoshita, and A. Yamaji, J. Appl. Phys. **47**, 371 (1976).

[48] M. P. Singh, W. Prellier, Ch. Simon, and B. Raveau, Appl. Phys. Lett. **87**, 022505 (2005).

[49] G. Catalan, Appl. Phys. Lett. **88**, 102902 (2006).

[50] M. Clausse, Colloid & Polymer Sci. **253**, 1020 (1975).

[51] G. Catalan, and J. F. Scott, Nature **448**, doi:10.1038/nature06156 (2007).

# Chapter 2

# Brief Overview of Manganites

In this chapter, we will briefly describe the perovskite manganites and some mechanisms used to explain the fascinating magneto-transport properties of hole doped manganites.

## 2.1 Perovskite manganites

Manganites ( $Re_{1-x}Di_xMnO_3$, Re and Di are trivalent rare earth and divalent alkaline earth elements respectively) that show colossal magnetoresistance are members of the perovskite family, which has the general formula $ABO_3$. The large sized $Re^{3+}$ and $Di^{2+}$ ions are distributed randomly over the A-sites in the crystal, and the smaller Mn ions occupy the B-site at the center of the unit cell (See Fig. 2.1). Each Mn ions is surrounded by the six oxygen ions and form the $MnO_6$ octahedron pattern (See Fig. 2.1). The structure of manganites is close to that of the cubic perovskite. The tilting and stretching of $MnO_6$ octahedra around Mn ions, due to the doping in manganites, creates the rhombohedral or orthorhombic lattice structure. Another possible origin of the deformation of the $MnO_6$ octahedron is the Jahn-Teller effect (as will be discussed later). The structure of manganites is governed by the tolerance factor $f = (r_A + r_O)/(\sqrt{2}(r_B + r_O))$, where $r_A$, $r_B$ and $r_O$ are the (averaged)

ionic radii of A, B (Mn) site cations and O anion, respectively [1, 2, 3]. The perovskite structure is stable for $0.89 < f < 1.02$ ($f = 1$ corresponding to the ideal cubic closely packed structure [2, 3]).

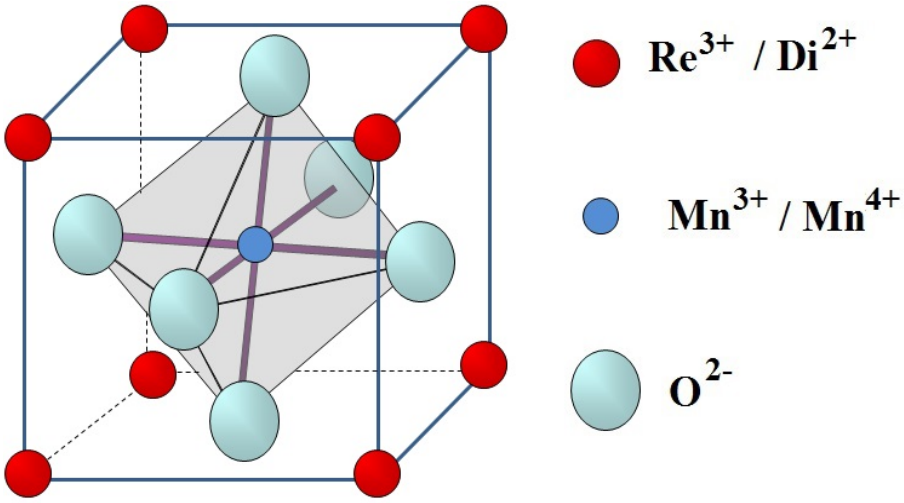


Figure 2.1: Schematic diagram of the perovskite manganite structure ($ABO_3$). A=$Re^{3+}$/$Di^{2+}$ and B=Mn, where Re (=La, Sm, Pr, Nd etc.) and Di (=Sr, Ca etc.) are the trivalent rare earth and divalent alkaline earth elements, respectively. The shaded sketch shows the $MnO_6$ octahedron pattern.

The physical properties of perovskite-type manganites mainly depends on two parameters: the doping level ($x$), and the average size of the cations A, $r_A$. Depending on the doping level, the perovskite manganite shows various magnetic and electric phases such as ferromagnetic metallic, antiferromagnetic, paramagnetic insulating, as well as charge/orbital ordered states (see chapter1, Fig. 1.1). In undoped manganites ($ReMnO_3$), all manganese (Mn) ions exist in a +3 state ($Mn^{3+}(3d^4)$). The doping level $x$ introduces $Mn^{4+}(3d^3)$ ions with an empty d orbital (a hole), and controls the ratio of $Mn^{3+}$ and $Mn^{4+}$ ions in manganites. The charge carriers (holes or electrons) then can move between different Mn ions. On the other hand, the decrease of $r_A$ due to smaller ions doping leads to an increasing distortion of the crystal structure and decreasing tolerance factor ($f < 1$) from the ideal cubic. The resulting reduction of Mn-O-Mn angle from $180^0$ to a smaller value weakens the ferromagnetic double

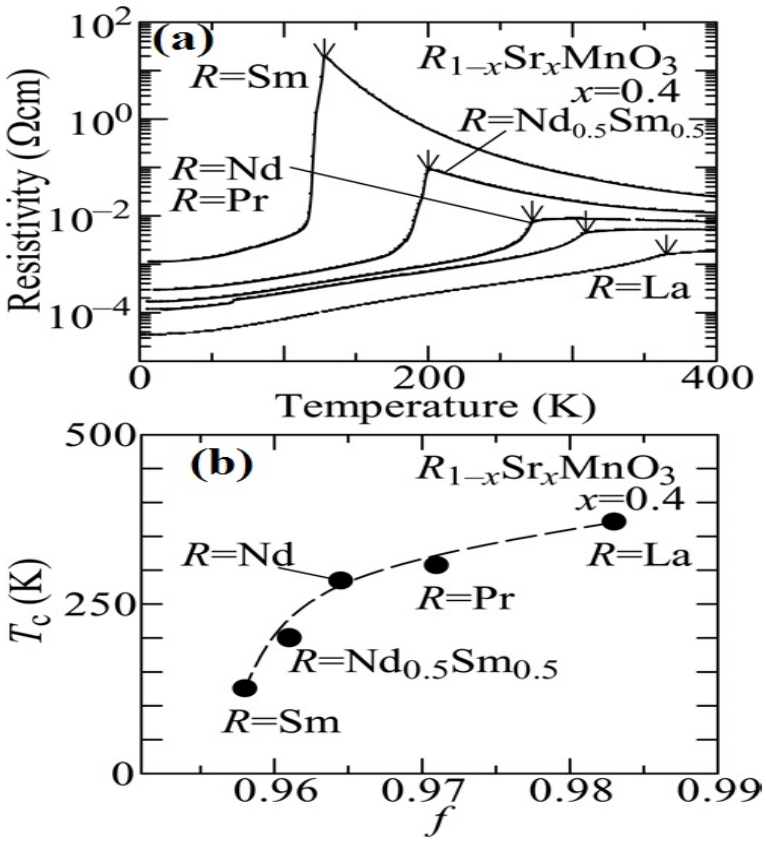


Figure 2.2: (a) The temperature dependence of resistivity for crystals of $R_{0.60}Sr_{0.40}MnO_3$ (R=La, Pr, $Nd_{0.5}Sm_{0.5}$ and Sm). The arrows indicate Curie temperatures ($T_C$). (b) The $T_C$ as a function of tolerance factor($f$) for $R_{0.60}Sr_{0.40}MnO_3$ crystals. The dotted thin line is a guide to the eyes. Figures are reproduced from Ref.[1].

exchange (as will be discussed later) and increases the tendency to localize the charge carriers [1]. Fig. 2.2 [1] shows an example for the variation of tolerance factor/lattice distortions and the electric and magnetic transport properties in the $Re_{0.60}Sr_{0.40}MnO_3$ (Re=La, Pr, $Nd_{0.5}Sm_{0.5}$ and Sm) manganite system. The resistivity increases, and the Curie temperature ($T_c$) decreases, with smaller ions doping in A site.

The strong coupling interaction between charge, spin, orbital, and lattice in hole doped perovskite manganites produces fascinating transport properties including a metal to insulator transition (MIT) that can be tuned by impurity doping and by the application of external stimuli including magnetic field,

pressure, laser and x-ray irradiation, electric field or electric current [1, 2, 3, 4, 5, 6]. The physical properties of these strongly correlated electronic materials are influenced by a combination of many mechanisms, such as double exchange, Jahn-Teller distortions, electron phonon coupling and phase separation, as will be discussed in this chapter.

## 2.2 Crystal field theory and Jahn-Teller effect

Crystal field theory is an important model for perovskite manganites that describes the breaking of degeneracies of electronic d orbital states of Mn ions, due to a static electric field produced by surrounding O anions (or charge distribution). For an isolated Mn ion, five degenerate orbital states are available to the 3d electrons. In the perovskite manganite, each Mn ion is surrounded by an oxygen octahedron. The hybridization and electrostatic interaction with O 2p electrons create a crystal field effect for the outer 3d electrons in $Mn^{3+}$ ion. This crystal field lifts the fivefold degeneracy of d electrons by splitting the energy levels and forming lower lying triply degenerate $t_{2g}$ states ($d_{xy}$, $d_{yz}$ and $d_{zx}$ ) and higher doublet $e_g$ states ( $d_{x^2-y^2}$ and $3d_{z^2-r^2}$) [1] (see Fig. 2.3). The $t_{2g}$ orbitals are less hybridized with O 2p states and considered as localized electrons. The $e_g$ electrons can hop between different Mn ions. The $e_g$ electrons become localized when the hopping interaction is relatively small. One of the causes of the $e_g$ electron localization is Jahn-Teller coupling of the $e_g$ electron with the surrounding oxygen displacement [1]. On account of $e_g$ as well as $t_{2g}$ levels being degenerate in the $Mn^{3+}$ ion and the $e_g$ orbital having an unoccupied state, an energetically favorable geometrical distortion of the $MnO_6$ octahedron occurs by further splitting of the d orbitals [1], as shown in Fig. 2.3. This lifting of degeneracy due to the orbital-lattice interaction is called the Jahn-Teller (JT) distortion/effect. The distortion of the $MnO_6$ octahedron is co-operative: if one occurs in a particular octahedron it will af-

fect the neighbours. Pure manganites, $Re^{+3}Mn^{+3}O_3^{-2}$ are electrical insulators. Pure manganite contains Mn in the $Mn^{+3}$ state which is JT ion. In all $Mn^{3+}$ ($3d^4$:$t_{2g}^3e_g^1$) based manganites, the $e_g$ electrons tend to be localized by accompanying lattice distortions that lead to the formation of an insulating state. The divalent ions doping (for example, Ca $^{2+}$ or $Sr^{2+}$ doping) in manganites corresponds to the creation of non-JT $Mn^{4+}$($3d^3$:$t_{2g}^3e_g^0$) ions, which break the long-range Jahn-Teller coupling [1]. Doping with divalent ion also produces a vacancy (hole) in the $e_g$ electron state at the Mn-site. The $e_g$ electrons then can be itinerant and play the role of conduction electrons.

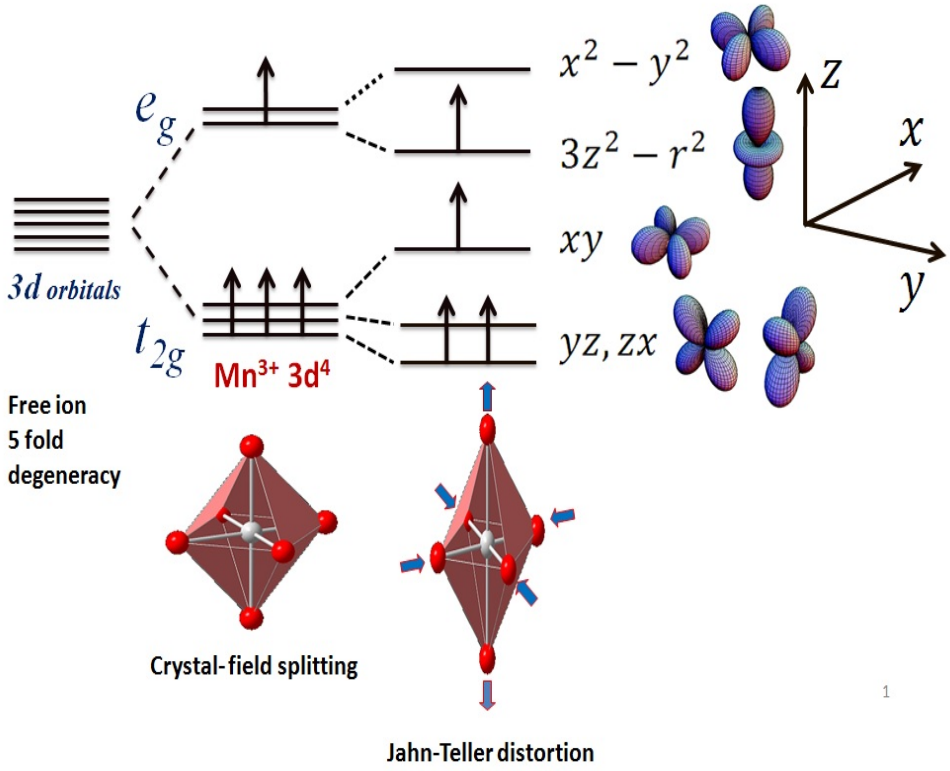


Figure 2.3: Crystal-field splitting of the five-fold degenerate atomic 3d levels into lower $t_{2g}$ (triply degenerate) and higher $e_g$ (doubly degenerate) levels. The JahnTeller distortion of the $MnO_6$ octahedron further lifts each degeneracy. After Ref.[1].

## 2.3 Double exchange mechanism

Colossal magnetoresistance (CMR) effect in perovskite manganite can be qualitatively understood in the framework of the double exchange (DE) interaction model. When the rare earth site (A site) in $ReMnO_3$ is doped with a divalent ion, a proportional number of JT $Mn^{3+}$ ions are converted into $Mn^{4+}$ (non-JT) ions , and the mobile $e_g$ electrons are introduced in the manganite system. Due to the strong intra-atomic Hunds coupling, all electrons of $Mn^{3+}(3d^4{:}t_{2g}^3e_g^1)$ and $Mn^{4+}(3d^3{:}t_{2g}^3e_g^0)$ are aligned parallel in the ground state, leading to a total spin of S= 2 and S= 3/2, respectively. The hopping of the $e_g$ electrons between two partially filled d orbitals of Mn ions via O 2p orbitals, as shown in Fig. 2.4(a), is called the double exchange mechanism [7]. This mechanism favors the ferromagnetic metallic phase below $T_c$ and the paramagnetic insulating state above the $T_c$. The electron transfer between neighboring Mn ions depends on the angle between their magnetic moments. The hopping probability ($t$) can be written as $t = t_0 cos(\theta/2)$ [1], where $t_0$ is the maximum value of hopping parameter and $\theta$ is the angle between the neighboring magnetic moments (See Fig. 2.4(b)). Thus, according to the DE mechanism, the $e_g$ electron transfer probability is maximum for ferromagnetically aligned spin ($\theta = 0$), and electrical resistivity of the sample should have a minimum value. Therefore, ferromagnetism and metallicity are intimately linked. For antiferromagnetic spin coupling, the $e_g$ electrons transfer are forbidden, and thus the system is insulating. At around the $T_c$, their is a maximum in the resistance since the alignment of the magnetic moments of Mn ions is destroyed. The magnetic field aligns the core spin and therefore increase the conductivity via DE interaction, especially in the vicinity of $T_c$. The materials therefore show extremely large magnetoresistance near the $T_c$ under the magnetic field.

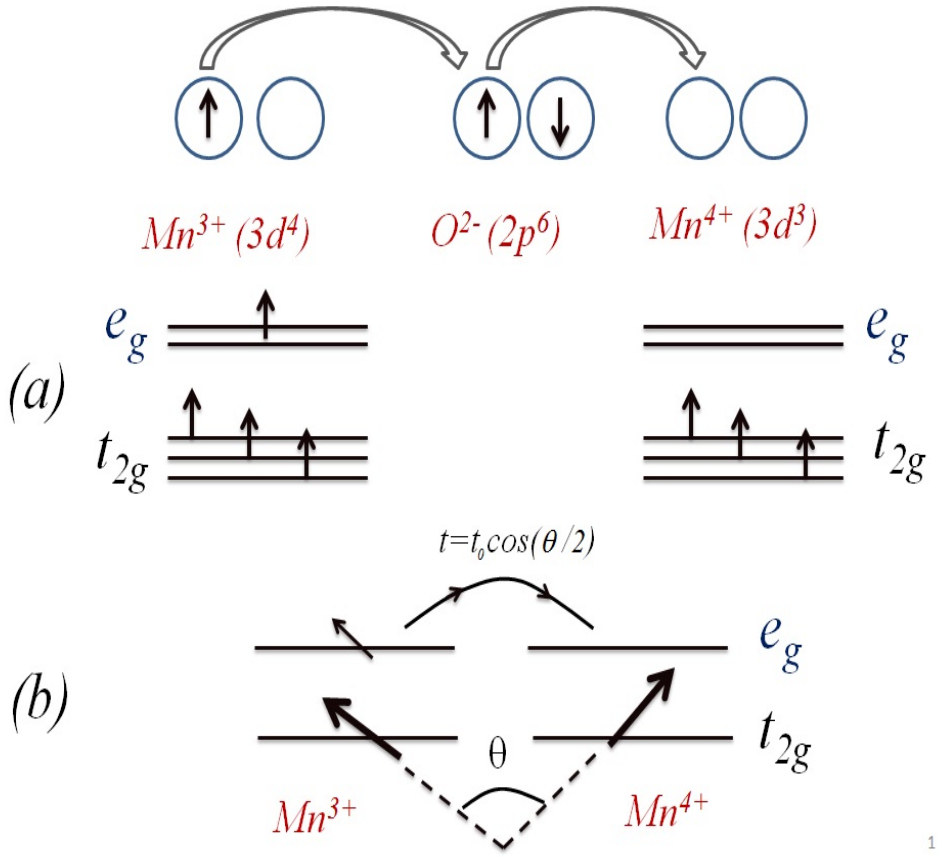


Figure 2.4: (a) Schematic representation of double exchange mechanism (where two electrons having the same spin direction hop from $Mn^{3+}$ to $O^{2-}$ and from $O^{2-}$ to $Mn^{4+}$ simultaneously). (b) sketch representing the probability of $e_g$ electron transfer ($t$) between neighboring Mn ions. The hopping exchange integral, $t = t_0 cos(\theta/2)$ [1, 2], where $\theta$ is the angle between the neighboring magnetic moments.

## 2.4 Electron phonon coupling

Double Exchange (DE) has been agreed as being crucial for CMR but insufficient to explain the physical properties of manganites completely. Millis et al.[8] pointed out that in addition to DE the strong electron-phonon coupling should be taken into account to explain the dramatic change of resistivity in the CMR effect and the resistivity values in the paramagnetic state. Later several experimental observations [9, 10, 11, 12, 13] accepted the importance of electron-phonon coupling for explaining the distinctive properties of perovskite

manganites. The strong electron phonon coupling in perovskite manganites is mainly caused by the Jahn-Teller effect of $Mn^{3+}$ ions [9]. For localized $e_g$ electrons, the Jahn-Teller distortions of oxygen octahedra around $Mn^{3+}$ ions are static and usually collective. These distortions become dynamic when $e_g$ electrons move. The polaron-like transport behavior in temperature dependent resistivity observed for temperatures above $T_c$, indicates that polarons are the predominant high-temperature type of charge carriers in manganites [5]. The $e_g$ electrons accompanied by lattice distortion are called lattice polarons or Jahn-Teller polarons. This transport of lattice and spin distortions is also called a magnetic polaron. At low temperatures, the competition between DE and JT typically leads to ordered phases. DE can win the competition and delocalize the $e_g$ electrons when the core spins are well aligned.

To explain the properties of doped perovskite manganites, Alexandrov et al.[14] proposed a different theory/model based on the idea of current carrier density collapse (CCDC) due to pairing of polaronic carriers. When two polarons are nearby, they can lower their energy by sharing the same distortions, which give rise to an effective attraction between the polarons. If the interaction is adequately large, then that attraction induces a bound bipolaron. Pairing of oxygen p holes into heavy bipolarons ( a local bound pair of two polarons) in the paramagnetic (PM) phase and their magnetic pair breaking in the ferromagnetic (FM) phase (the so-called CCDC) are responsible for the insulator-metal transition and CMR in doped manganites according to Alexandrov et al [14, 15]. The main concept behind the CCDC theory is that in the PM phase a large fraction of polarons are bound into immobile bipolarons. As temperature decreases within the PM phase, the density of these pairs increases, resulting in fewer charge carriers (mobile polarons), and hence, the resistivity quickly increases with the reduction in the carrier density. Below $T_c$, the binding of polarons into pairs competes with the FM exchange interaction which tends to align the polaron moments and, therefore, breaks

those pairs ( immobile bipolarons) apart and increases the density of charge carriers. These competing interactions and the density of current carriers lead to a peak in resistivity of CMR materials near the $T_c$. The application of an external magnetic field also causes a break up of bipolarons resulting in large negative magnetoresistance near the $T_c$ [14].

## 2.5 Charge and Orbital ordering

Charge ordering (CO) is the opposite of double exchange, since it localizes electrons creating an antiferromagnetic insulating state. Doping of perovskite $Re^{+3}Mn^{+3}O_3^{-2}$ with divalent ions (such as $Ca^{2+}$ and $Sr^{2+}$) results in a fraction of the Mn ions occurring in the +4 state, giving rise a new electronic order, charge order, wherein the $Mn^{3+}$ and $Mn^{4+}$ charges are arranged in a periodic fashion (See Fig. 2.5 (a)). The superstructures of localized charge carriers (charge order) usually accompany the orbital order (OO) [1]. The CE-type CO/OO antiferromagnetic (see Fig. 2.5 (a)) are typically associated with the $x = 1/2$ manganites, where the numbers of $Mn^{3+}$ and $Mn^{4+}$ ions are equal and arranged as in a checker board [1, 16, 17, 18]. The $Mn^{3+}$ sites are JT distorted, which localizes the electrons. Orbital ordering (of $d_{3x^2-r^2}$ or $d_{3y^2-r^2}$) occurs without charge ordering in the $x = 0$ $ReMnO_3$ (see Fig. 2.5(c)), which is ferromagnetic in the *ab* planes and antiferromagnetic along the c-axis (see Fig. 2.5(d)) [1]. The A-type antiferromagnetic state is also encountered in some doped $Re_{1-x}Di_xMnO_3$ systems. Here, the $d_{x^2-y^2}$ type orbital is present at the $Mn^{3+}$ site (see Fig. 2.5(b)), and some electron transfer can occur between the Mn cations in the *ab* plane [17]. However, the existence of CO/OO clusters has been seen experimentally in the paramagnetic state of various doped manganites [1]. Even in some doped manganites which are in a ferromagnetic metallic state at low temperatures, CO clusters occur. The sizes of clusters are affected by the carrier concentration or composition, average size of the

A-site cations, temperature and other external factors such as magnetic and electric fields [1, 16, 17, 19, 20]. This coexistence of CO/OO antiferromagnetic insulating and ferromagnetic metallic states in doped perovskite manganites below the magnetic ordering temperature leads to a new scenario of phase separation and percolation to explain the intriguing CMR of manganites.

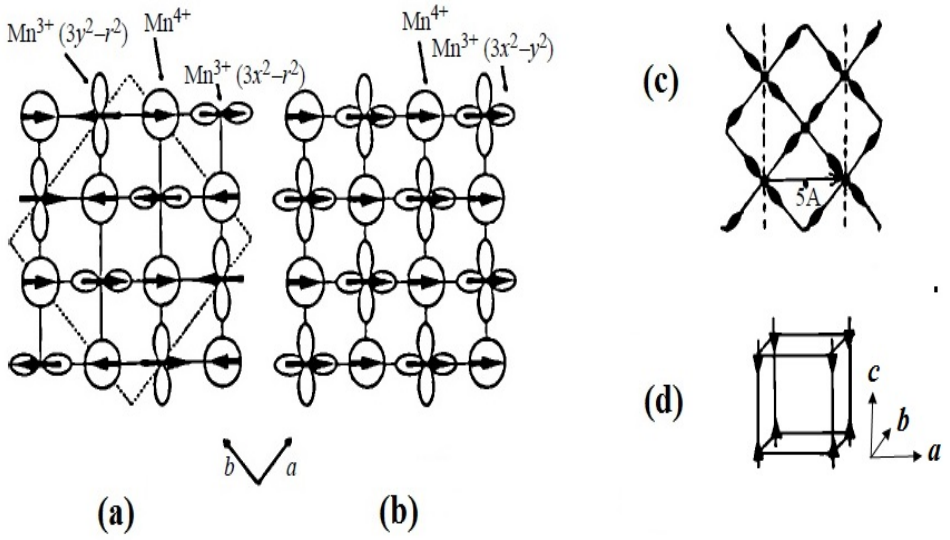


Figure 2.5: Charge, spin and orbital ordering in $ab$ plane of doped $Re_{1-x}Di_xMnO_3$ manganites: (a) CE-type and (b) A-type antiferromagnetic (AF). (c) Orbital ordering in undoped manganites ($x = 0$; for example, $LaMnO_3$ ). (d) A-type AF spin ordering along the $abc$ axes. In (a) and (b) figures, circles correspond to $Mn^{4+}$ ions. The dashed line in Fig. (a) shows the unit cell . Figures are reproduced from Ref.[17].

## 2.6 Percolation in a phase separation scenario

The Double Exchange model (see section 2.3) was based on the assumption that the manganites are uniform and homogeneous without any form of coexisting clusters of competitive phases. But, there is accumulated evidence today that many oxide materials with correlated electrons are not electronically homogeneous. Experimental evidence of inhomogeneous magnetic states, where

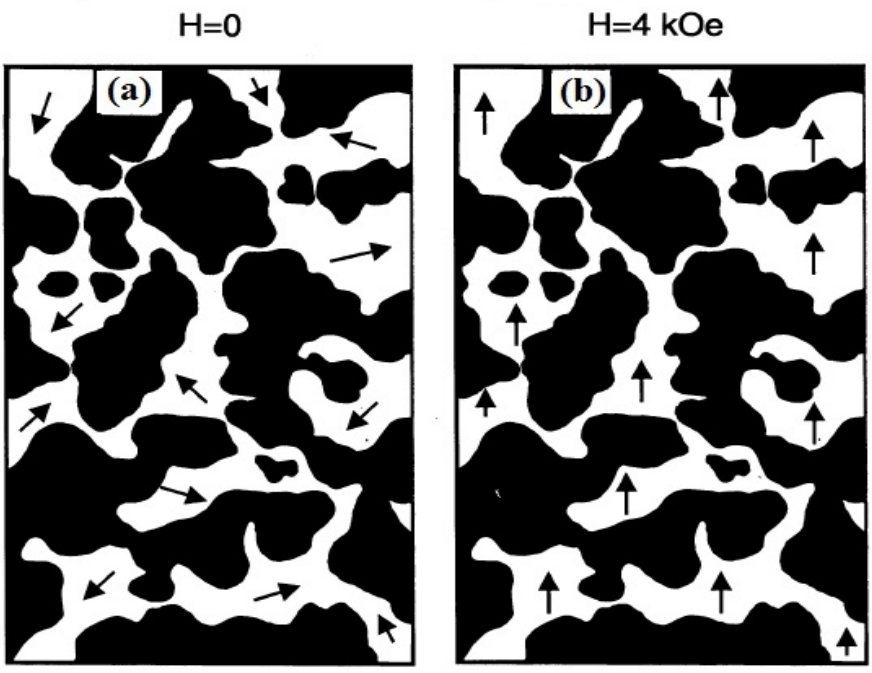


Figure 2.6: (a) and (b) (reproduced from Ref.[22]): Schematic illustration of the sub-micrometer-scale coexistence of the $x = 1/2$-type CO insulating (dark area) and FM metallic (white area) domains in $(La,Pr)_{5/8}Ca_{3/8}MnO_3$. The typical size of domains is $\sim 0.5\mu$m. In zero magnetic field (a), the magnetizations of FM domains are random, but all magnetizations of FM domains can be aligned by applying low magnetic field of about 4 kOe (which is high enough to orient magnetic domains but low enough not to affect the CO phase)(b).

ferromagnetic (FM) metallic, antiferromagnetic (AF) or paramagnetic (PM) insulating as well as charge/orbital ordered states coexist in the same compound has been found in a variety of hole doped manganites [1, 4, 5, 6, 21, 22]. This phenomenon is known as phase separation (PS). An interesting aspect of this PS phenomenon is the scale of the inhomogeneities. The length scale associated with these inhomogeneities can vary from sub-nanometers up to even a micron depending on the composition, giving distinct electrical and magnetic properties in manganites. Within this PS scenario the insulator-to-metal transition (IMT) can be described by percolation assuming a growth of the FM domains (conducting phase) with decreasing temperature. If regions of this phase overlap a continuous current may flow resulting in a sudden drop of the

resistivity (see Fig. 2.6). Further external perturbation such as magnetic field, electric field, x-ray or light irradiation can also induce IMT and, thus, alter the phase distribution in a PS state [1, 4, 5, 6]. Electron conduction between neighboring FM domains should be reduced if their magnetizations are not aligned (see Fig. 2.6 (a)). The low magnetic fields (which is low enough not to affect the CO phases) easily align the magnetizations of FM domains and increase the conductivity in manganites (see Fig. 2.6 (b)). The high magnetic fields also melt the CO phases and change the relative volumes of coexisting CO insulating and FM metallic phases. The existence of inhomogeneous state or competing phases of CO-AF and FM and melting of CO-AF phases by the magnetic fields lead to CMR in manganites.

The PS is generally the result of a competition between charge localization and delocalization. The size of clusters depends on the competition between double exchange and Coulomb force. Depending on the strength of interaction the shapes of clusters could be droplets or stripes [2, 4, 6]. Such a PS scenario bridges the gap between the DE model and the lattice models.

# Bibliography


[1] Y. Tokura, Rep. Prog. Phys. **69** 797 (2006).

[2] P. K. Siwach, H. K. Singh, and O. N. Srivastava1, J. Phys.: Condens. Matter **20**, 273201 (2008).

[3] A.-M. H.-Gosnet, and J.-P. Renard, J. Phys. D: Appl. Phys. **36**, R127 (2003).

[4] C. N. R. Rao and P. V. Vanitha, Curr. Opin. Solid State Mater. Sci. **6**, 97 (2002).

[5] K. Dörr, J. Phys. D: Appl. Phys., **39**, R125 (2006).

[6] E. Dagotto, T. Hotta, and A. Moreo, Phys. Rep. **344**, 1 (2001).

[7] C. Zener, Phys. Rev. B **82**, 403 (1951).

[8] A. J. Millis, P. B. Littlewood, and B. I. Shraiman, Phys. Rev. Lett. **74**, 5144 (1995).

[9] A. J. Millis, Phil. Trans. R. Soc. Lond. A **356**, 1473 (1998).

[10] A. J. Millis, Nature **392**, 147 (1998).

[11] J.-S. Zhou, J. B. Goodenough, A. Asamitsu, and Y. Tokura, Phys. Rev. Lett. **79**, 3234 (1997).

[12] C. P. Adams, J. W. Lynn, Y. M. Mukovskii, A. A. Arsenov, and D. A. Shulyatev, Phys. Rev. Lett. **85**, 3954 (2000).

[13] Y.-D. Chuang, A. D. Gromko, D. S. Dessau, T. Kimura, and Y. Tokura, Science **292**, 5521 (2001).

[14] A. S. Alexandrov, and A. M. Bratkovsky, Phys. Rev. Lett. **82**, 141 (1999).

[15] A. S. Alexandrov, A. M. Bratkovsky, and V.V. Kabanov, Phys. Rev. Lett. **96**, 117003 (2006).

[16] Y. Tokura, and N. Nagaosa, Science **288**, 462 (2000).

[17] C. N. R. Rao, J. Phys. Chem. B, **104**, 5877 (2000).

[18] K. F. Wang, Y. Wang, L. F. Wang, S. Dong, D. Li, Z. D. Zhang , H. Yu, Q. C. Li, and J.-M. Liu, Phys. Rev. B **73**, 134411 (2006).

[19] S. Mori, C. H. Chen, and S.-W. Cheong, Nature **392**, 473 (1998).

[20] M. Coey, Nature **430**, 155 (2004).

[21] J. C. Loudon, N. D. Mathur, and P. A. Midgley, Nature **420**, 797 (2002).

[22] M. Uehara, S. Mori, C. H. Chen, and S.-W. Cheong, Nature **399**, 560 (1999).

# Chapter 3

# Sample Preparation and Measurement Techniques

In this chapter, we will describe the various experimental techniques used to prepare the bulk (polycrystalline) manganite samples, ferroelectric $BaTiO_3$ (BTO) samples, composite samples of manganite and BTO, sputtering targets and heterostructures. We will also briefly report on the working principles of the various instruments commonly used to investigate the structural, electrical transport, magnetic, ferroelectric and multiferroic properties of materials in this thesis.

## 3.1 Sample preparation methods

### 3.1.1 Polycrystalline bulk samples

#### Manganite samples

Polycrystalline manganite samples in this study were prepared using the standard solid state reaction method. For example, to prepare stoichiometric $Sm_{0.60}Sr_{0.40}MnO_3$: a prescribed ratio of $Sm_2O_3$, $SrCO_3$ and $MnO_2$ powders were mixed thoroughly and calcined at 1373 K for 24 hours in air. This pro-

cedure allows the mixed powders to undergo the following chemical reaction: $(0.60/2)\ Sm_2O_3 + 0.40\ SrCO_3 = Sm_{0.60}Sr_{0.40}MnO_3 + 0.40\ CO_2$. The resulting samples were pulverized, pressed into pellets and sintered twice at 1473 K for 24 hours with an intermediate pulverizing. The samples were again pulverized, and then sintered for a third time at 1473 K for 48 hours. This process (pulverizing and sintering) was repeated three times in order to obtain a high degree of chemical homogeneity and single phase perovskite crystal structure sample. The pellet shaped sintered samples were cut into rectangular shaped bars for resistance and magnetization measurements. The resistance of the samples were measured using the four probe method with silver contacts that are sputtered using a radio frequency magnetron source onto the samples as will be discussed later. A piece of the rectangular bars was pulverized and used in powder x-ray diffraction analysis. Moreover, pellets with 1 inch diameter were made as a target material for thin film deposition.

**Ferroelectric samples**

Polycrystalline ferroelectric $BaTiO_3$ samples in this study were also prepared using the standard solid state reaction methods. A prescribed ratio of $BaCO_3$ and $TiO_2$ powders were mixed thoroughly and calcined at 1273 K for 12 hours in air. It allow the mixed powders to undergo the following chemical reaction: $BaCO_3 + TiO_2 = BaTiO_3 + CO_2$. The resulting samples were pulverized, pressed into pellets and sintered twice at 1473 K for 12 hours with an intermediate pulverizing. The samples were again pulverized, and then sintered for a third time at 1473 K for 24 hours. This process (pulverizing and sintering) was repeated three times in order to obtain a high degree of chemical homogeneity and single phase perovskite crystal structure sample. The pellet shaped sintered samples were cut into rectangular shaped bars for ferroelectric characterization as will be discussed later. A piece of the rectangular bars was pulverized and used in powder x-ray diffraction analysis.

#### Composite samples

The final sintered pellets of single phase $Sm_{0.60}Sr_{0.40}MnO_3$ and $BaTiO_3$ were pulverized for making composite (1-$y$) $Sm_{0.60}Sr_{0.40}MnO_3$ +$y$$BaTiO_3$ samples. A prescribed ratio of $Sm_{0.60}Sr_{0.40}MnO_3$ and $BaTiO_3$ powders were mixed thoroughly, pressed into pellets and calcined at 1473 K for 48 hours in air. The pellet shaped sintered composite samples were cut in rectangular shaped bars for resistance, magnetization and ferroelectric characterization as will be discussed later. A piece of the rectangular bars was pulverized and used in powder x-ray diffraction analysis.

### 3.1.2 Thin film deposition

Due to high deposition rate and less substrate damage from stray particles (electrons and Argon ions) [1, 2], magnetron sputtering is one of the most successful methods of depositing epitaxial thin films on single crystal substrates. Depending on the target material either direct current (DC) or radio frequency (RF) magnetron sputtering source was used for depositing the epitaxial thin films in this thesis.

#### Manganite thin films

Manganite epitaxial films, such as $La_{0.66}Ca_{0.34}MnO_3$ (LCMO) or $Sm_{0.60}Sr_{0.40}$ $MnO_3$ (SSMO), were deposited onto oriented $SrTiO_3$ (STO) single crystal substrates using DC magnetron sputtering. The basic principle of sputtering is as follows. Energetic ions in a vacuum chamber are accelerated towards a solid sputtering target to eject target atoms. These atoms fly off and hit a nearby substrate, and can then bond to it at an atomic level, developing a very thin film (see the Fig. 3.1). An inert sputtering gas, argon, is introduced in the vacuum chamber for creating $Ar^+$ ions which work as energetic ions. In DC sputtering, a constant applied voltage between the target (also called

a cathode) and the substrate ionizes Ar atoms and creates a plasma, a hot gas-like phase consisting of ions and electrons. As a result of this biasing, the $Ar^+$ ions are accelerated towards the target material ejecting target atoms as well as producing secondary electrons. The electrons released during argon ionization and the secondary electrons are accelerated towards the anode, subsequently colliding with additional Ar atoms, creating more ions and free electrons, continuing the sputter deposition. In DC magnetron sputtering, additional placement of magnets below the target increase the ionization rate. The magnetic field is located parallel to the target surface. Strong magnetic field near the target causes the secondary electrons to spiral along magnetic flux lines, and hence the probability of collision between the electrons and Ar atoms near the target is greatly enhanced. As a result the plasma is confined to an area of the target and a dense plasma is created even at low pressure of sputtering gas [1]. In addition to the Ar gas, $O_2$ is added as a reactive gas during the epitaxial film deposition. $O_2$ helps in maintaining the stoichiometry of the epitaxial films.

**Ferroelectric thin films**

$BaTiO_3$ ferroelectric epitaxial thin films were deposited using RF magnetron sputtering source. Generally, RF magnetron sputtering is good for sputtering insulating materials [2]. As the Ar ions strike the surface of a conducting target, the resulting charges can move freely in the conducting material. This prevents any charge buildup. However, free charge movement does not occur in insulating samples. Hence, during insulator deposition using DC sputtering , positive charge build up on the cathode (target) makes it impossible for other ions to bombard the target surface. In this case $10^{12}$ volts may be required to sputter insulators using this method. On the other hand, RF sputtering provide an alternating potential difference between the target (cathode) and anode, and prevents charge build up on an insulating surface.

**Heterostructure of manganite and ferroelectric multilayers**

In the first step, manganite (such as LCMO) films were deposited on oriented STO or LAO substrates using DC magnetron sputtering. Then, ferroelectric BTO films were deposited on the manganite layers using RF magnetron sputtering. During BTO deposition on the manganite layer, silicon was used to mask a part of the manganite layer in order to utilize the manganite layer as an electrode (see Fig. 3.8).

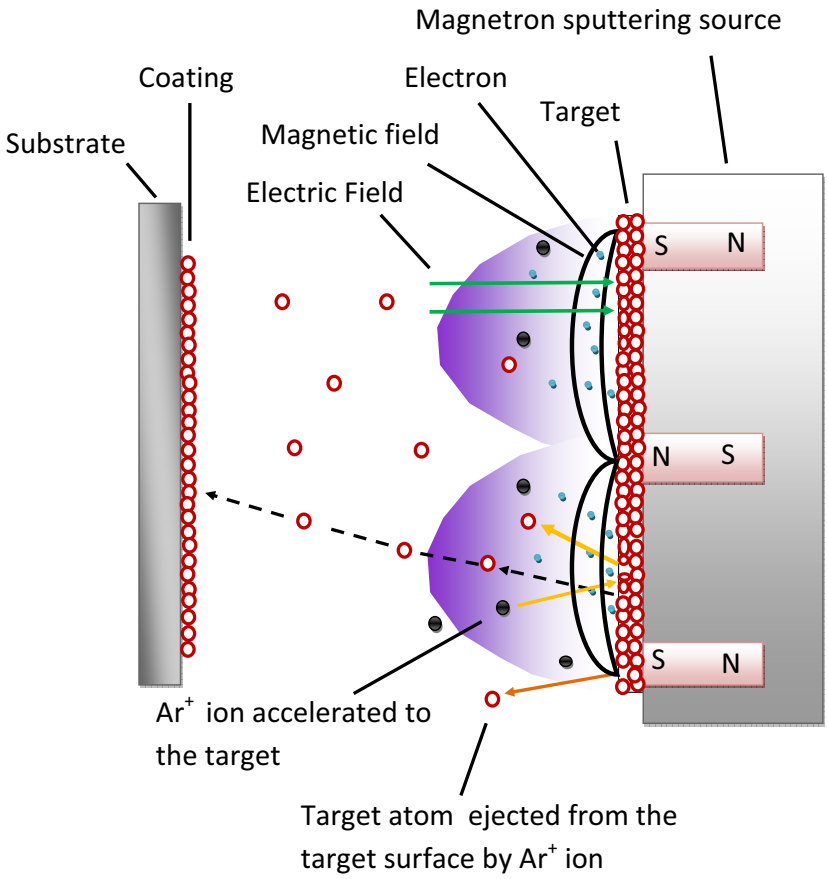


Figure 3.1: Schematic illustration of Magnetron sputtering.

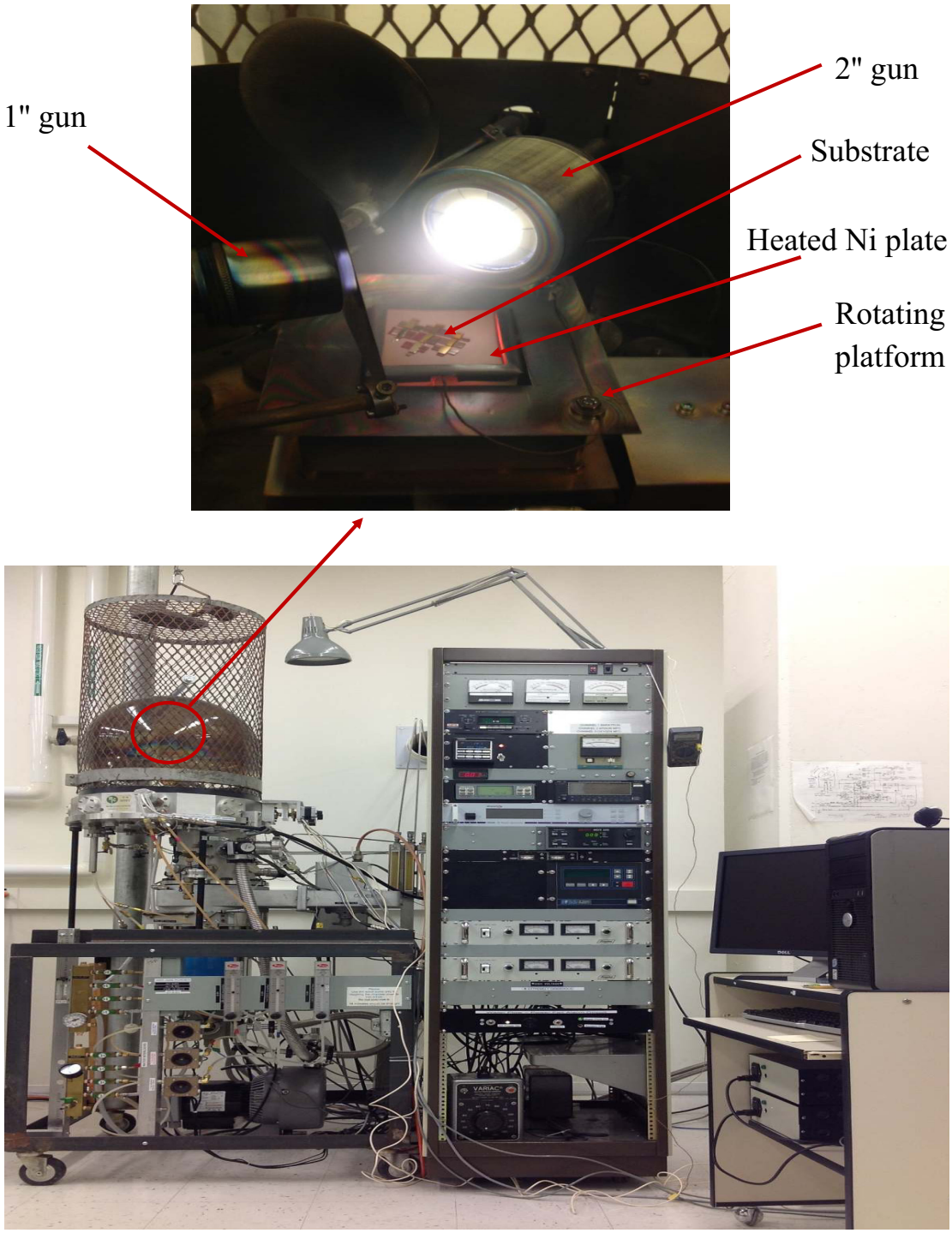


Figure 3.2: Magnetron sputtering system that was used to deposit epitaxial thin films. Top picture: multilayer epitaxial films deposition.

**Deposition process**

The magnetron sputtering system that was used for thin film deposition in this thesis is placed inside a custom designed bell jar vacuum chamber with a base pressure of less than $5 \times 10^{-7}$ Torr which is produced by a cryopump. The system consists of three magnetron sputtering sources ( one 1 inch and two 2 inch guns manufactured by Angstrom Sciences, Inc.) powered by either RF or DC power supplies and a heater for heating the substrates up to 750 $^{o}$C. The heater is equipped with a Ni plate for mounting the substrates (see Fig. 3.2). The heater is mounted on rotating platform for making a uniform thickness of the film on a substrate.

The first step in the magnetron sputtering deposition of a film is to clean substrates (such as STO). Clean substrates are then mounted on the Ni plate using Ag paste. This makes a good thermal contact between the Ni-plate and the substrate. Air in the bell jar is pumped out till the base pressure is around $4.5 \times 10^{-7}$ Torr. Typically, before doing any deposition, the chamber pressure is increased to working pressure $\sim$ 120 mTorr by introducing ultra-high pure $O_2$ and Ar gas mixture of ratio 5:1 into the chamber. Then the heater temperature is raised to 750 $^{o}$C with a rate of 12.5$^{o}$C per minute and kept constant at this temperature for about 20 minutes for thermal annealing of the substrate. The deposition is performed using either a DC power of 50 W or a RF power of 100W at 750 $^{o}$C for 10 to 720 minutes depending on the desired thickness of the film. After deposition, the chamber is filled with oxygen at a pressure around 1 atm and the films are subsequently quenched to 650 $^{o}$C and kept at this temperature for 3 hours to ensure the stoichiometric content of oxygen in the film. Films are then cooled to room temperature with a rate of 20$^{o}$C per minute.

In order to make electrodes or contact pads for ferroelectric and resistance measurement of the epitaxial films, silver was sputter deposited at room temperature using a RF power of 40 W at an Ar pressure of 20 mTorr for about

$5 - 12$ minutes.

## 3.2 Sample Characterization

### 3.2.1 Structural characterization

Following the preparation of polycrystalline sample and epitaxial thin film deposition, x-ray diffraction measurements were carried out on these samples using a RIGAKU 12 kW rotating anode x-ray diffractometer (see Fig. 3.3) (Cu -$K_\alpha$ radiation) at room temperature. The voltage and current were kept at 55 kV and 150 mA, respectively during x-ray diffraction. The measurement was performed using a $2\theta$ scan mode with a resolution of $0.01^o$. The x-rays are scattered by the sample according to Bragg's law : $n\lambda = 2d_{hkl}\sin\theta$, where $n$ is the order of reflection, $\lambda$ is the wavelength of x-rays, $d_{hkl}$ is the distance between crystal planes (hkl) and $\theta$ is the diffraction angle. The x-ray diffraction patterns were compared with published results and analyzed using the *FullProf Suite* software for bulk polycrystalline samples (see the Fig. 3.3). The lattice spacing of the epitaxial films deposited on oriented substrates were determined from the diffraction patterns of thin films. X-ray diffraction gives information about the phase purity, crystallinity and epitaxial strain in the sample.

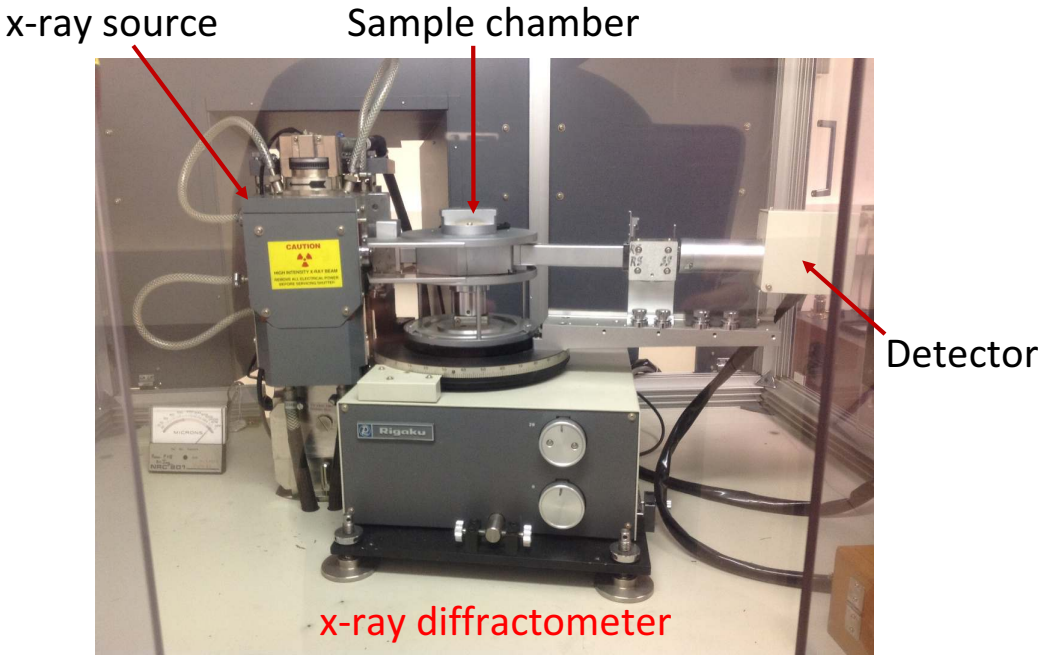


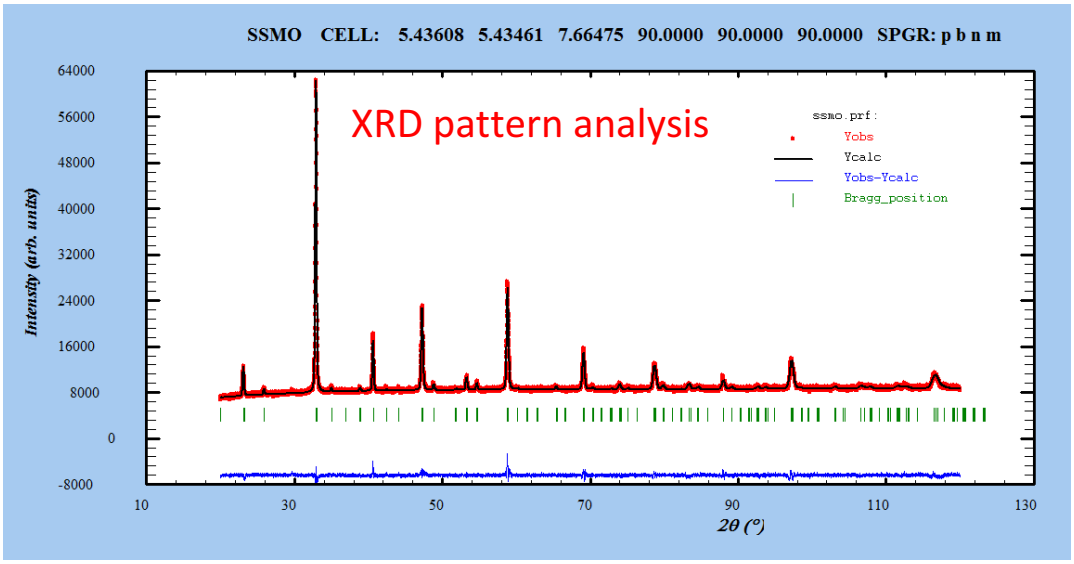


Figure 3.3: Top picture is an x-ray diffractometer used for x-ray diffraction (XRD). Bottom picture is an example of XRD pattern analysis using *FullProf Suite* software for $Sm_{0.60}Sr_{0.40}MnO_3$ (SSMO) sample.

## 3.3 Transport Measurements

### 3.3.1 Resistance

#### Magneto-resistance setup

The resistance of the samples was measured using a home build anisotropic magnetoresistance (AMR) system (see Fig. 3.4 ). The samples were mounted on a copper block (cold-finger) located in a cryostat that is attached to a closed-cycle cryocooler (a Sumitomo RDK-408D2 close cycle refrigerator). Apiezone-N grease was used to hold the sample in place and provide good thermal contact with the copper sample holder. LakeShore 332 temperature controller equipped with a heater (CADDOCK MP850 - thick film resistors) and temperature sensors (LakeShore Cernox CX-1050-AA) were used to control the sample holder's temperature (T) between 10 to 325K. In some instances, temperature on the surface ($T_S$) of the sample was also measured simultaneously with another (Cernox) thermometer. An electro-magnet (GMW 3473-70, Dipole Electromagnet) with a rotatable platform was used to generate magnetic fields up to 1.1 Tesla using a unipolar power supply (Elgar, model SGA60/83C-1CAA). A step motor driver (Parker 6104 indexer drive) was used to rotate the magnet. The magnet can rotate between 0 and $180^o$ with a resolution of $0.1^o$ and is used to apply magnetic field to the sample at various angles. A 16 channel relay box was used to apply the current and measure the voltage of four (4) samples. This allowed us to measure the resistance of the four samples at the same time. Both current and voltage wires were connected separately to each sample. All the instruments are connected and controlled by the graphical programming language Labview through GPIB and serial interfaces. The resistance of the samples was measured as a function of current strength, temperature, magnetic field, angle and time. All data were recorded and graphically presented using the Labview program during the measurement.

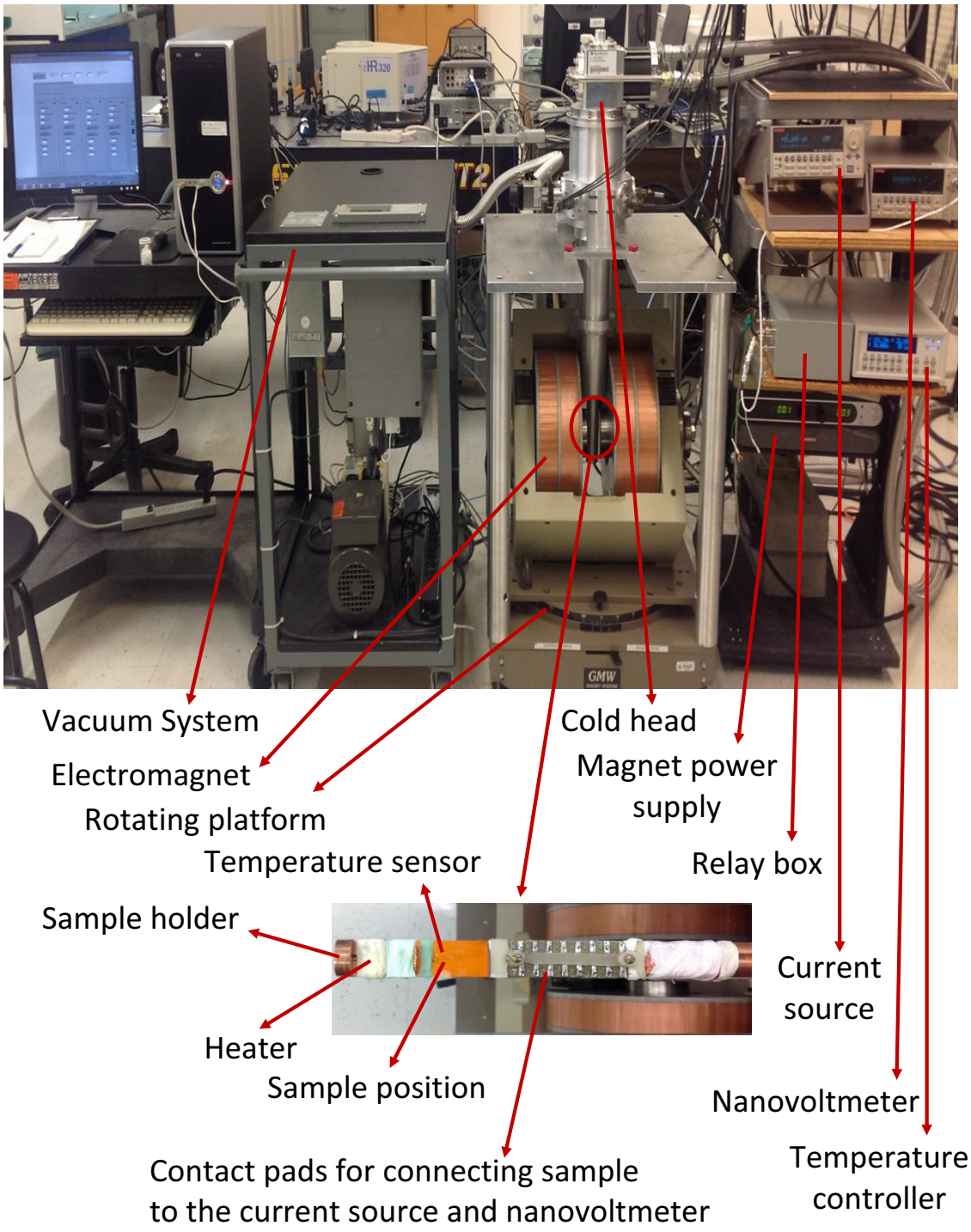


Figure 3.4: Anisotropic magnetoresistance (AMR) system that was used to measure the resistance of the sample.

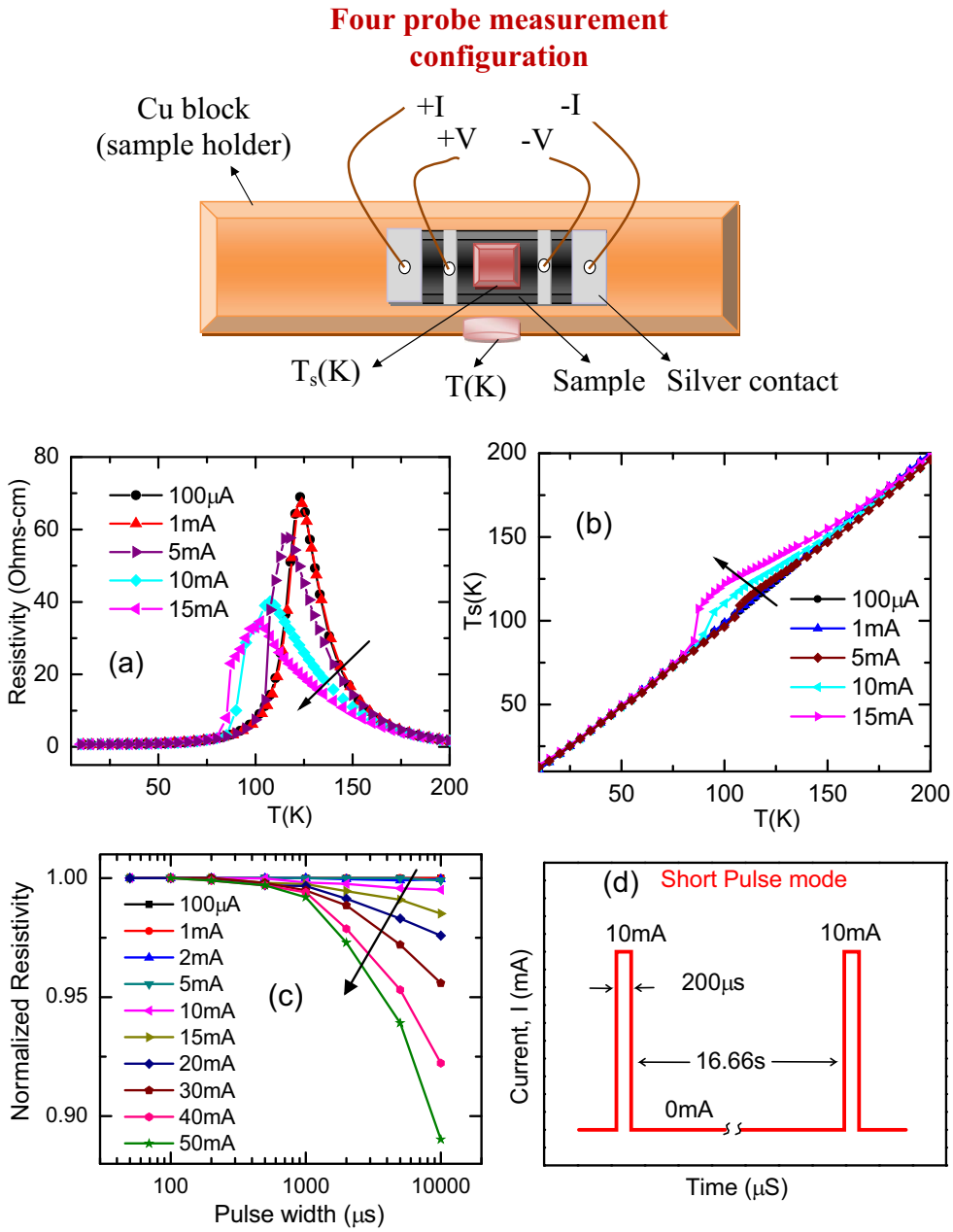


Figure 3.5: (a) Temperature dependence of resistivity for $Sm_{0.60}Sr_{0.40}MnO_3$ (SSMO) at various DC excitation. (b) The corresponding surface temperature of the sample ($T_S$) vs the temperature of the sample holder ($T$). Top figure shows the measurement configuration. (c) Normalized resistivity vs pulse width of the excitation current for SSMO at the MIT temperature of the sample. The arrows in Fig. (a), (b) and (c) indicate increasing current strength. (d) The timing diagram for the current excitation of short pulse mode that was used for intrinsic electroresistance measurement.

**Resistance measurement**

The resistance of the samples was measured using the four probe method (see Fig. 3.5 (top figure)) with silver contacts that were sputtered onto the samples using the RF magnetron source. Copper leads were mechanically attached to silver contacts using indium. A typical distance between the voltage probes was between 0.8 and 1.5 mm. A Keithley 6221 AC/DC current source was used to supply the current to the samples, and the voltage drop across the sample was measured using either a Keithley 2182A Nanovoltmeter or a Tiepie HS3 high resolution USB oscilloscope. For high resistance samples, a Keithley 2410 source meter and two probe measurement were used to determine the resistance of the sample ( In this case contact resistances were negligibly small compared to the sample resistance).

The resistivity of the samples was determined using the formula $\rho = RA/L$, where $R(= V/I)$ is the resistance between the voltage probes of the sample, $A$ is the cross-sectional area through which the current (I) flows, $L$ is the distance between the voltage electrodes and V is the voltage drop across them.

As discussed in chapter 4, one of the goals of this research was to investigate the intrinsic electroresistance (a relative change of the electrical resistance of a material due to a change in the magnitude of the electric field/current) of some manganites. To determine the electroresistance, the resistance of the samples was measured using various current excitation. Note that the Joule heating effect is a problem in resistance measurement when using high current excitation. Fig. 3.5 (a) shows an example how the Joule heating can change the resistivity of SSMO sample at large dc current excitation. An increase of the sample's surface temperature near the metal to insulator transition (MIT) (see Fig. 3.5 (b)) and shifts of the MIT to lower temperature (see Fig. 3.5 (a)) at higher current strength are evidence of the Joule self-heating effect.(The Joule heating generated in the sample can be expressed as $H = I^2Rt$, where $t$ is the current passing time through the sample). Since the amount of Joule

heating depends on the time the current passed through the sample, it is advantageous to pass the current through the sample for a short time and simultaneously measure the resistance of the sample.

The combination of a Keithley 6221 AC/DC current source and a Keithley 2182A nanovoltmeter was used to provide the pulse current excitation and to measure the voltage, respectively. Fig. 3.5 (c) shows the variation of normalized resistivity (measured at the MIT ) as a function of the pulse width (between 50$\mu$s and 10ms) of the excitation current (between 100$\mu$A and 50mA). The normalized resistivity is independent of pulse width at low current excitation, and at higher current excitations the normalized resistivity is almost constant for pulse widths $<$ 1ms. For pulse widths $\geq$ 1ms, the normalized resistivity is found to decrease gradually with higher current strengths (see Fig. 3.5 (c)) which is caused by Joule heating. These measurements imply that Joule self-heating effects can be dramatically reduced by using short current pulses.

Since our goal was to measure the intrinsic ER in the samples, the Joule heating must be minimized. Therefore, short current pulses (of widths 200 $\mu$s) were supplied to the SSMO sample for determination of the intrinsic voltage. (There was a rise time of the current from the source. The current pulses of width $>$100 $\mu$s were reliable for measuring the voltages across the SSMO samples using high current excitation). Each current pulse is separated by a long period of zero current (see Fig. 3.5 (d) for an example of the timing diagram). The estimation of the intrinsic ER is not a trivial issue because significant Joule heating can be present at high currents in our samples. An oscilloscope can be advantageous to inspect and analyze the time dependence of the voltage across the sample. The nanovoltmeter was primarily used to measure the small voltage drops at low current excitation (where Joule heating is also minimal), because it can measure small voltage drops more precisely than the oscilloscope. The oscilloscope was used to record the time depen-

dence of voltage at higher current excitations. The existence of Joule heating is indicated by a change of voltage with time; therefore, the extrapolation analysis was used to estimate the intrinsic resistivity . These are discussed in detail in chapter 4.

### 3.3.2 AC magnetic susceptibility measurement

Measurements of the temperature dependence of ac magnetic susceptibility $\chi(T)$ for all polycrystalline bulk samples were carried out in a zero dc magnetic field using a home-built susceptometer. A schematic diagram of our ac susceptometer system is shown in Fig. 3.6.

The basic principle of the susceptometer is as follows. Ac susceptibility is measured using Faraday's mutual inductance principle (induced voltage in the secondary coil, $V(t) = -d\phi/dt = -A(dB/dt)$ where flux $\phi = BA$, $B$ is the magnetic induction and $A$ is the area of a loop). A small alternating magnetic field, $H_{ac}$ produced by the primary coil induces a voltage in the secondary coil. Secondary coil consists of two coils which are identical and oppositely wound. A change in magnetic field induces equal and opposite electromotive force in these two coils . As a result, any experimentally detected signal in an ac susceptometer is only due to changing magnetic moment of the sample in response to an applied ac field.

The induced moment in a small ac field is given by $M_{ac} = (dM/dH)H_{ac}sin(\omega t)$ where $\omega$ is the driving frequency, $H_{ac}$ is the amplitude of the driving field and $dM/dH = \chi$ is the slope of the $M(H)$ curve, called the susceptibility. At higher frequency, the sample's magnetization may lag behind the driving field. Thus, ac susceptibility is a complex quantity. The magnitude of the susceptibility is $\chi$ and the phase shift relative to the drive signal is $\varphi$. The in-phase or real component of $\chi$ is $\chi' = \chi\cos\varphi$ and the out-of-phase or imaginary component of $\chi$ is $\chi'' = \chi\sin\varphi$. At low frequency, the $\chi'$ is just the slope of the $M(H)$. The $\chi''$ is related to the energy losses or the energy absorbed by the sample

from the ac field. Both $\chi'$ and $\chi''$ are very responsive to thermodynamic phase changes, and are used to measure transition temperatures.

Polycrystalline bulk samples were mounted on a sapphire rod (sample holder) located in a vacuum cryostat that is attached to a closed-cycle cryocooler. Apiezone-N grease was used to hold the sample and provide good thermal contact with the sample holder. A LakeShore 332 temperature controller equipped with a resistor heating element and cernox thermometers was used to control the sample holder temperature between 23K and 300K. A Keithley 6221 AC/DC current source was used to supply the ac current (of amplitude 2mA) to the primary solenoid coil. A EG&G 7265 DSP lock-in amplifier was used to detect the induced voltage in a secondary coil. The secondary coil consists of two identical coils which are wound in opposite directions and connected in series. The sample is placed in one of the coils (known as the sample coil) while the other coil (known as the balance coil) is left empty. These are illustrated in Fig. 3.6. The ac current in the primary coil generates a magnetic field and magnetizes the sample, and the flux change in the sample is detected by the secondary coil. The induced voltage in the secondary coil is proportional to the susceptibility of the sample [3]. All the instruments are connected and controlled by the Labview program through GPIB and serial interfaces. All data are recorded and graphically presented using the Labview program. The $\chi$ of all the bulk samples was measured as a function of temperature, and the Cure temperature of the samples, $T_cs$, was determined using the gradient method (see the Fig. 3.7 for an illustration of the gradient method).

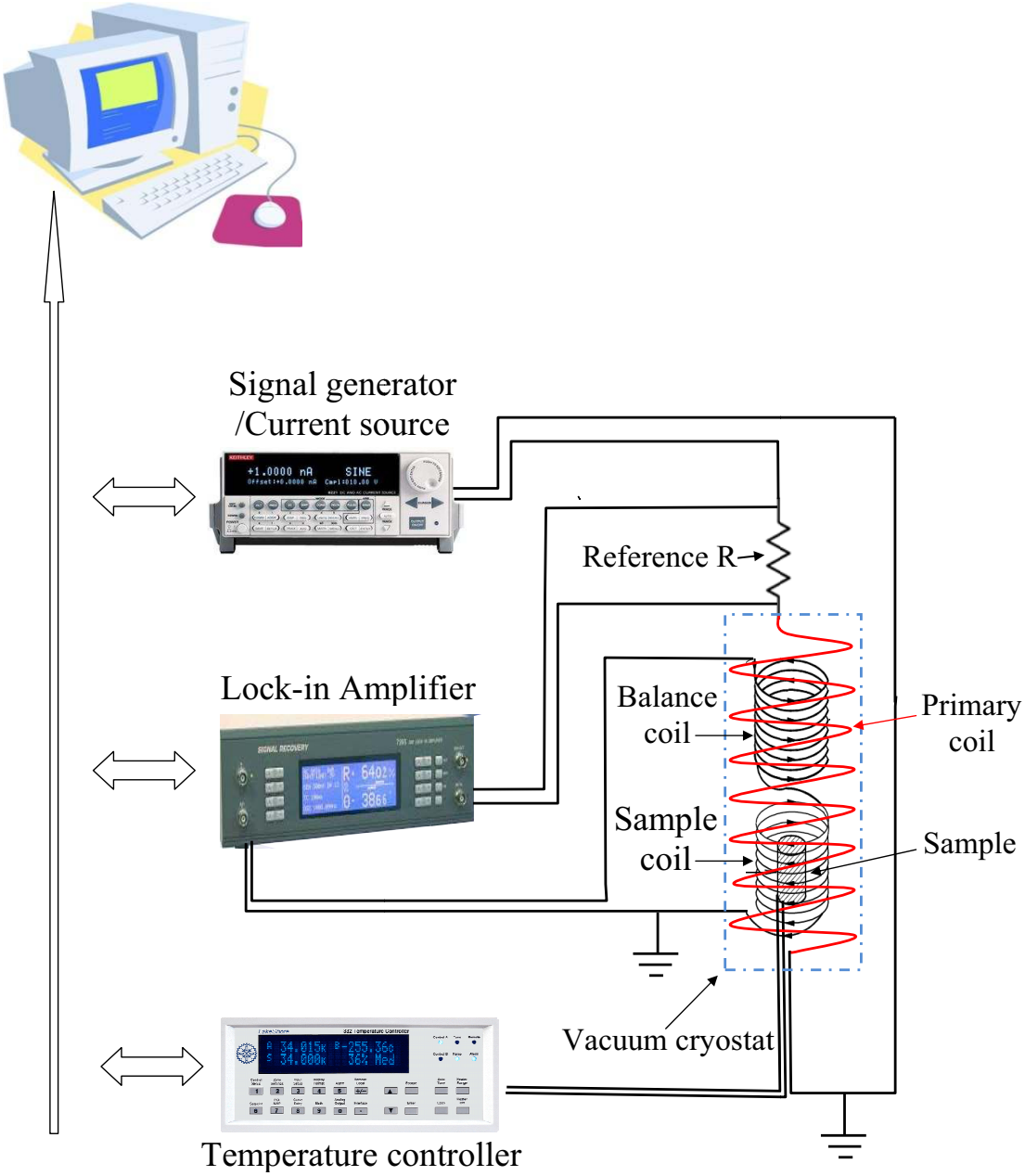


Figure 3.6: Schematic illustration of Ac susceptometer system.

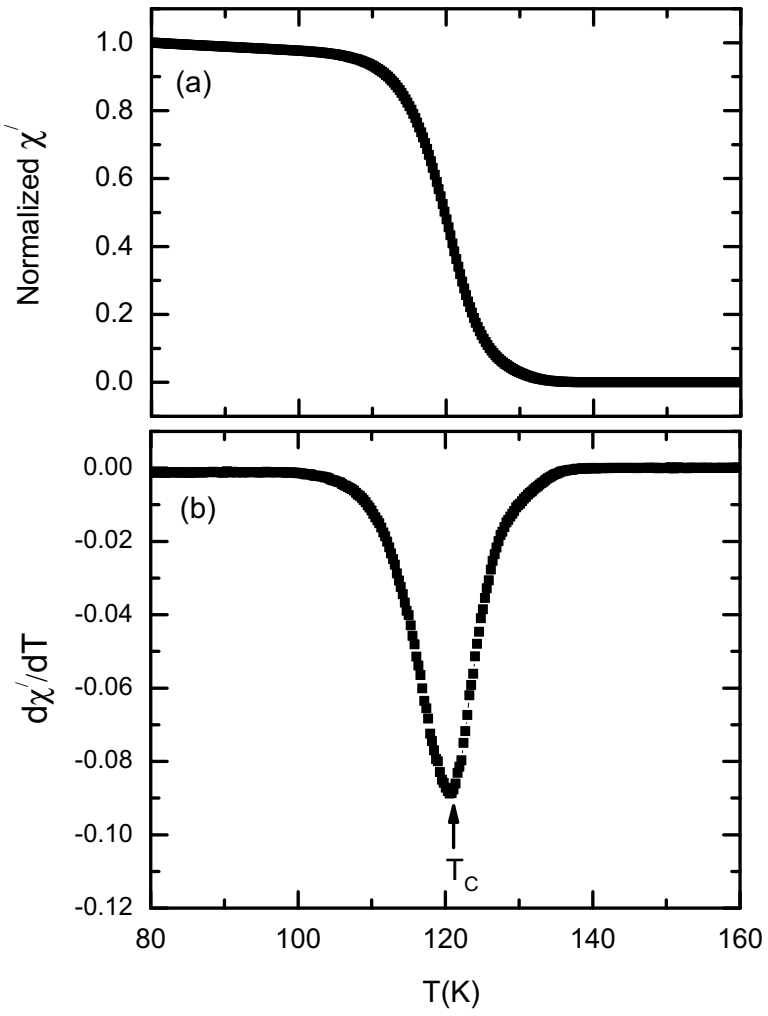


Figure 3.7: (a) Normalized $\chi'$ versus temperature (T) for $Sm_{0.60}Sr_{0.40}MnO_3$ sample. (b) An example of the gradient method for determination of $T_c$ from the $\chi'(T)$ measurement of $Sm_{0.60}Sr_{0.40}MnO_3$ sample.

### 3.3.3 Capacitance, magnetocapacitance and dielectric measurement

Parallel-plate capacitor configuration is the most convenient geometry for the measurement of capacitance, dielectric permittivity and polarization of polycrystalline bulk and thin film samples. Sketches of capacitance measure-

ment configuration for our bulk and thin film samples are shown in Fig. 3.8. The silver electrodes on the samples were sputtered using a RF magnetron source. The capacitance and dielectric loss of the samples were measured using an Agilent 4284A ($20Hz - 1MHz$) precision LCR meter. A schematic view of the capacitance measurement setup is shown in the Fig. 3.9. A liquid-nitrogen glass Dewar was used to cool the sample, and an OMEGA HH506RA digital thermometer with a K-type thermocouple was used to monitor sample temperature. A thin layer of apiezon grease was used to attach the sample to the sample holder and to maintain better thermal contact between them. The sample holder was placed inside the electromagnet (see Fig. 3.9) in order to measure capacitance of the sample in the presence of an external dc magnetic field. The magnet was powered by a Sorensen DCS20-150SE power supply which provides magnetic fields up to 0.57 Tesla. In some cases, the bulk samples were kept inside the vacuum bell jar where the samples were heated to 200 $^{o}$C (473K) to confirm the high temperature phase transition in the samples (see Fig. 3.10 for an example of C(T) measurement for a $BaTiO_3$ bulk sample).

When the materials are under the influence of a time dependent electric field, the dielectric constant or dielectric permitivity response is a complex quantity and it contains two terms: in-phase or real component $\varepsilon'$ and out-of-phase or imaginary component $\varepsilon''$. The $\varepsilon'$ of the samples is calculated using the relation $\varepsilon' = (C_S t_S)/(\varepsilon_0 A)$, where $C_S$ is the capacitance of the sample, $t_S$ is the thickness of the sample, $\varepsilon_0$ is the vacuum permitivity ( $8.85 \times 10^{-12}$ F/m) and A is the electrode area of the sample (see Fig. 3.8). The $\varepsilon''$ is related to the dielectric losses . The value of the loss factor, $\tan\delta = \varepsilon''/\varepsilon'$ is taken as the figure of merit of the material.

The measurement of capacitance (or dielectric constant) under various applied magnetic fields is known as a magnetocapacitance (MC) (or magnetodielectric (MD)) measurement. This measurement is an important tool used to

confirm the existence of the magneto-electric (ME) coupling of the sample. Magnetocapacitance is defined as a change in capacitance due to an applied magnetic field. Mathematically, $MC = (C_S(H) - C_S(H = 0T))/C_S(H = 0T) = \Delta C_S/C_S$, and MD $= (\varepsilon'(H) - \varepsilon'(H = 0T))/\varepsilon'(H = 0T) = \Delta\varepsilon'/\varepsilon'$. Both expressions are equivalent. The temperature dependence of capacitance of our samples was measured in a 0.57 Tesla magnetic field, and MC of the samples was calculated using the above formula.

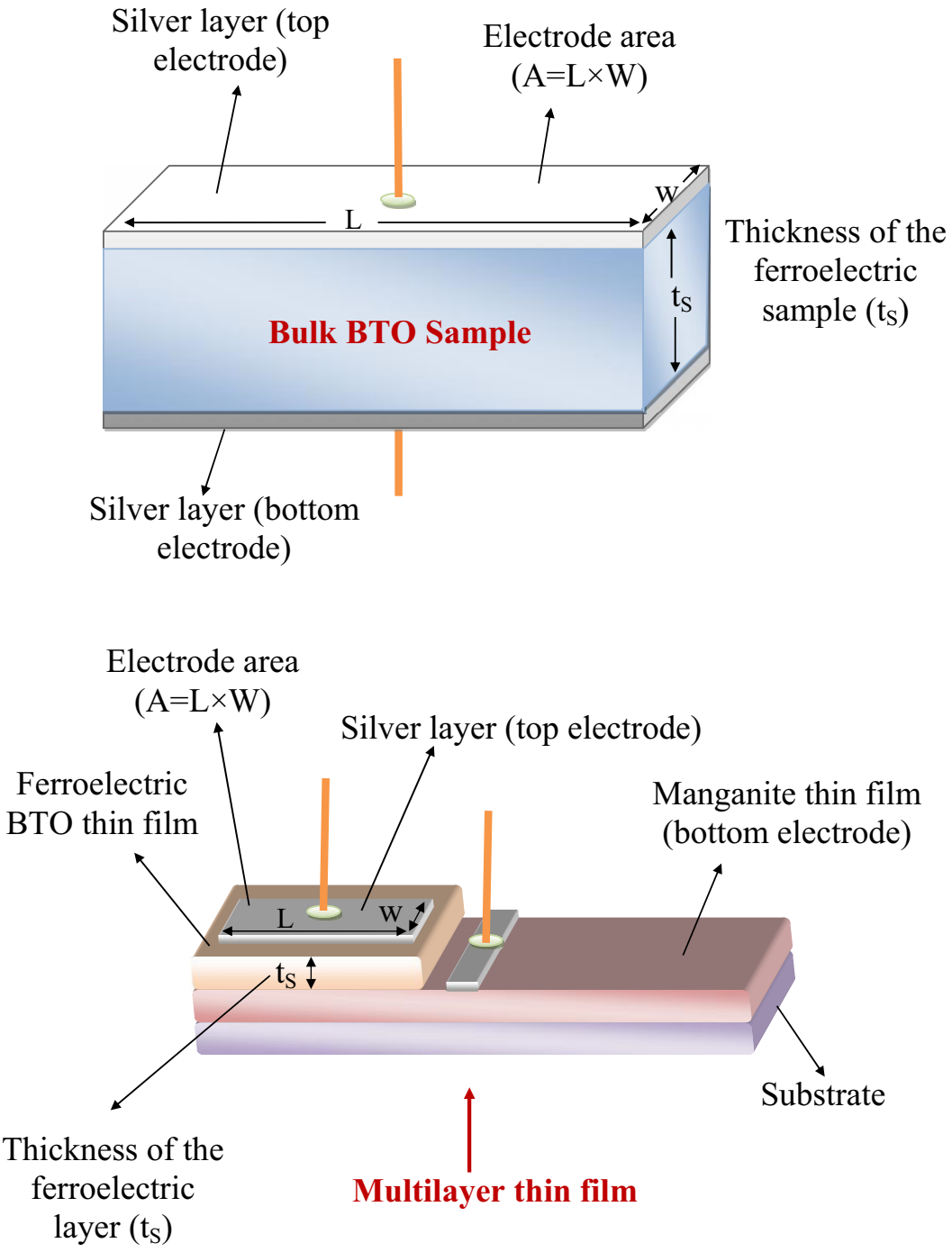


Figure 3.8: Sketches of the capacitance measurement configurations. Top sketch is for bulk $BaTiO_3$ (BTO) sample and bottom sketch is for multilayer thin film.

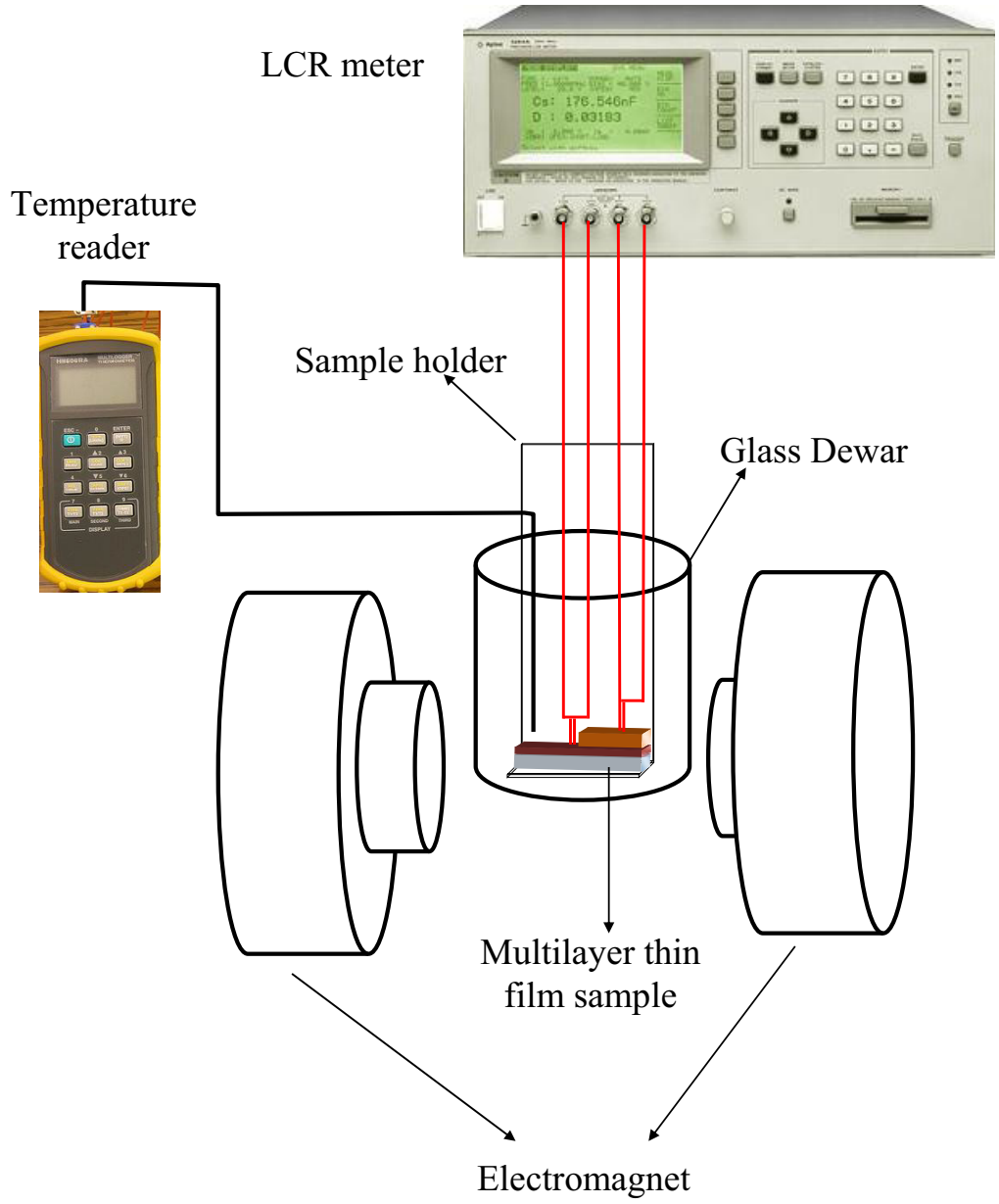


Figure 3.9: Schematic view of capacitance or magnetocapacitance measurement setup.

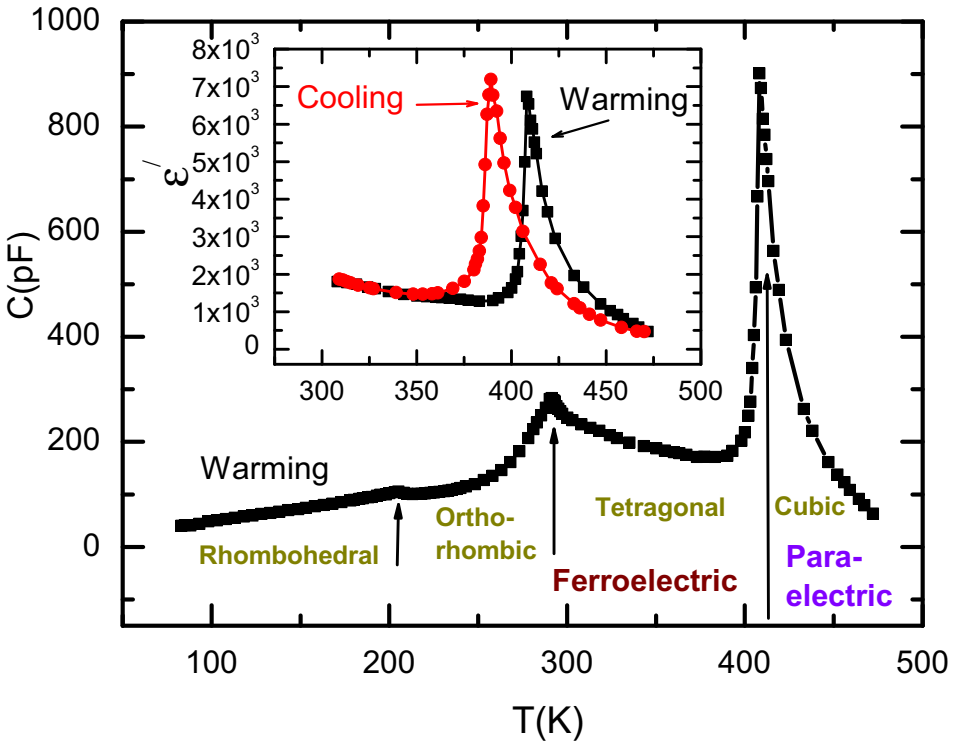


Figure 3.10: The temperature dependent capacitance C(T) of $BaTiO_3$ (BTO) bulk sample measured at $1kHz$. The vertical arrows indicate the successive structural transition temperatures of BTO : rhombohedral to orthorhombic at 205K, orthorhombic to tetragonal at 292K, and tetragonal to cubic at 408K. BTO shows ferroelectricity below 408K and paraelectricity above 408K. The inset shows the calculated dielectric constant ($\varepsilon'$) and thermal hysteresis behavior near the ferroelectric to paraelectric phase transition temperature during warming and cooling cycle. These results are in good agreement with previous studies of BTO sample [4, 5, 6].

### 3.3.4 Ferroelectric Polarization measurement

The electric field dependent polarization loop, P(E) for BTO bulk and multilayer thin films was measured using a home built system. A Sawyer-Tower circuit [7] (see Fig. 3.11) was constructed in our laboratory to trace the ferroelectric P(E) loop at room temperature and liquid nitrogen temperature. The following equipment was used in this set-up: A signal generator (1311 AU audiometric oscillator), a Tiepie HS3 high resolution USB oscilloscope,

two resistors $10M\Omega$ and $100k\Omega$ (which work as a simple voltage divider to scale down (100 times lower) the voltage across the resistor $100k\Omega$, in order to create a reference voltage that can be measured using the oscilloscope), a $1\mu$F standard capacitor (also known as reference capacitor ($C_{ref}$)) and a breadboard. In some instances, a step-up transformer ($13X$) was used to supply the high voltage signal to the circuit. A liquid-nitrogen glass Dewar was used to cool the sample, and an OMEGA HH506RA digital thermometer with a K-type thermocouple were used to monitor sample temperature. All data taken during P(E) loop measurement were collected using Tiepie multi channel measurement software.

The basic principle of a P(E) loop measurement using a Sawyer-Tower circuit is as follows. Application of varying electric field across a ferroelectric sample produces a polarization in it. The polarization of the sample ($P_S$) is defined as $P_S = Q_S/A = (V_S C_S)/A$, where $Q_S$ ($= V_S C_S$) is the charge of the sample, $C_S$ is the capacitance of the sample, $V_S$ is the voltage across $C_S$ and A is the electrode area of the sample. Since $C_S$ and $C_{ref}$ are in series (see Fig. 3.11), the charge on both is the same ( $Q_S = Q_{ref}$). Then, $P_S = (V_{ref} C_{ref})/A$, or, $P_S \propto V_{ref}$ (where $C_{ref}/A$ =constant).

The electric field across the sample ($E_S$) is defined as $E_S = V_S/t_S$, where $t_S$ is the thickness of the sample. If $C_S \ll C_{ref}$ then $V_S \gg V_{ref}$ and $V_S \approx V_A$, where $V_A$ is total applied voltage to the circuit. Now, $E_S \cong V_A/t_S$. The voltage across $R_2$ in the circuit is given by $V_{R2} = (R_2/(R_1 + R_2))V_A = (R_2/(R_1 + R_2))E_S t_S$. Therefore, $E_S = ((R_1 + R_2)/(R_2 t_S))V_{R2}$, or, $E_S \propto V_{R2}$ (where $(R_1 + R_2)/(R_2 t_S)$ =constant).

The data of $V_{ref}$ and $V_{R2}$ for our samples were collected using the USB oscilloscope (see Fig. 3.11), and then the electric field dependence of polarization P(E) was determined using the known values of $C_{ref}$, A, $R_1$, $R_2$ and $t_s$.

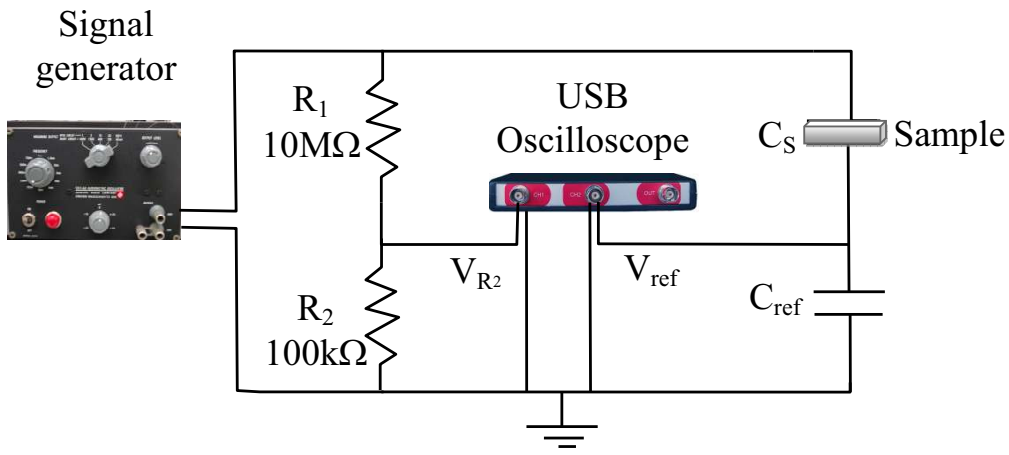


Sawyer- Tower circuit

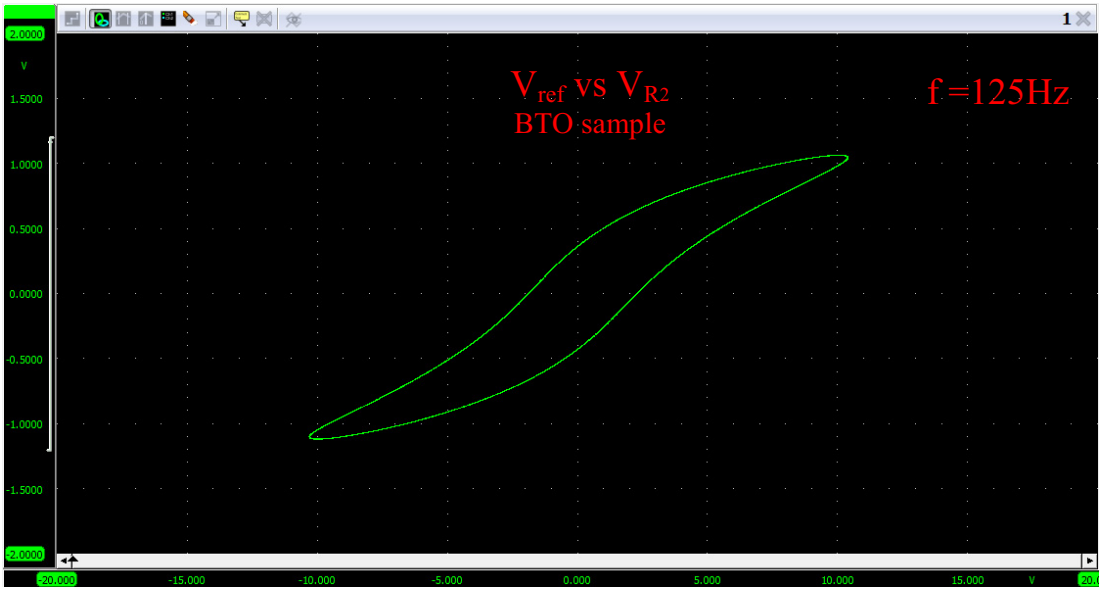


Figure 3.11: Top figure is a Sawyer-Tower circuit that used for P(E) loop measurements of our samples. Bottom figure is an example of loop measurement using the Sawyer-Tower circuit and USB oscilloscope for $BaTiO_3$ (BTO) sample at room temperature.

# Bibliography


[1] M. Ohring, Material Science of Thin Films, Academic Press (2002).

[2] K. Seshan, Handbook of Thin-film Deposition Process and Techniques, Noyes Publications, (2002).

[3] M. Nikolo, Am. J. Phys. **63**, 57 (1995).

[4] N. G. Kim, Y. S. Koo, C. J. Won, N. Hur, J. H. Jung, J. Yoon, Y. Jo, and M. H. Jung, J. Appl. Phys. **102**, 014107 (2007).

[5] G. H. Kwei, A. C. Lawson, S. J. L. Billinge and S.-W. Cheong, J. Phys. Chem. **97**, 2368 (1993).

[6] K. Kinoshita, and A. Yamaji, J. Appl. Phys. **47**, 371 (1976).

[7] C. B. Sawyer and C. H. Tower, Phys. Rev. Phys. **35**, 269 (1935).

# Chapter 4

# Intrinsic electroresistance of $Sm_{0.60}Sr_{0.40}MnO_3$ and $Sm_{0.55}Sr_{0.45}MnO_3$

## 4.1 Introduction

As discussed in Chapter 2, the mixed valent manganites $Re_{1-x}Di_xMnO_3$ (where Re and Di are the trivalent rare earth and diavalent alkaline earth elements, respectively) continue to attract interest because they possess fascinating properties such as colossal magnetoresistance (CMR), charge and orbital ordering (CO/OO), phase separation (PS), etc. [1, 2, 3, 4, 5, 6]. As a consequence of the strong interplay among spin, charge, lattice and orbital degrees of freedom, the ground state of manganites depends on which interactions dominate and can be tuned by impurity doping and by the application of external stimuli including magnetic field, pressure, laser and x-ray irradiation, electric field or electric current [1, 2, 3, 4, 7, 8]. The dependence of the electrical resistance of a manganite on the magnitude of the electric field/current, i.e., electroresistance (ER) [9, 10, 11, 12, 13, 14, 15, 16], is of sci-

entific interest and also has ramifications for applications such as non-volatile memory elements [10, 17]. Various mechanisms have been proposed to explain the origin of ER such as electric field induced melting of the CO state [9], structural rearrangement of ferromagnetic metallic (FMM) clusters in filamentary shapes along the direction of applied current [11], hot electron effects [12], pulsed voltage induced modification of carrier concentration [13], Joule heating [14, 15, 18, 19, 20], etc.

$Sm_{1-x}Sr_xMnO_3$ (SSMO) based manganite systems exhibit exotic electrical properties, which are mainly governed by multiphase competition [21, 22, 23]. One such property, as mentioned in Chapter 1, is the observation of ER in $Sm_{0.60}Sr_{0.40}MnO_3$ [14] (see chapter 1, Fig. 1.2) and $Sm_{0.55}Sr_{0.45}MnO_3$ [16] (see chapter 1, Fig. 1.3). Rebello *et al.* [14] investigated the ER of polycrystalline $Sm_{0.60}Sr_{0.40}MnO_3$ using the dc current and concluded that the results could be explained primarily by Joule heating (see chapter 1, section 1.1.1 for details). Mohan *et al.* [16] investigated the ER of polycrystalline $Sm_{0.55}Sr_{0.45}MnO_3$ using pulsed current (dc current for a few milliseconds) excitation. This method should drastically reduce any Joule heating [24] and facilitate measurement of the intrinsic ER. Intriguingly, they observed a giant ER ($\sim 2500\%$ at high currents) (see chapter 1, Fig. 1.3), much higher than ER measurements reported for other manganites, including $Sm_{0.60}Sr_{0.40}MnO_3$ [14].

In order to evaluate the reproducibility of the results reported by Mohan et al.[16] we have measured the *intrinsic* ER of SSMO $x = 0.45$ sample (see section 4.3.1). We have also measured the *intrinsic* ER of SSMO $x = 0.40$ sample (see section 4.3.1). From the existing literature [25, 26, 27] it is evident that the SSMO's with $x = 0.40$ and $x = 0.45$ exhibit different phase separated magnetic (hence transport) ground states (see chapter 1, section 1.1.1 for details), which may have noticeably different effects on the ERs of the compounds. In particular, the $x = 0.45$ manganite has a homogenous ferromagnetic (FM) ground state while a phase separated state comprised of

FM and anti-ferromagnetic (AF) regions exists for $x = 0.40$. Hence, from a scientific point of view it is interesting to explore the *intrinsic* ER properties of the two SSMO samples.

In analyzing the intrinsic ER in SSMO, as well as in manganites in general, it is highly relevant to establish the "controlling" parameter: is it *current* itself or is it *current density*? Although the latter is often assumed in the existing literature, to our knowledge this has not been experimentally established for SSMO or other manganites. To achieve this goal, we also investigated the current and current density dependent intrinsic ER for $x = 0.40$ and $x = 0.45$ compositions of $Sm_{1-x}Sr_xMnO_3$ (see section 4.3.2), where samples of each composition differ in geometrical dimension and resistance, but have the same resistivity.

## 4.2 Experimental Procedure

The polycrystalline $Sm_{1-x}Sr_xMnO_3$, $x = 0.40$ and $x = 0.45$, samples were prepared using the same solid state reaction method. A prescribed ratio of $Sm_2O_3$, $SrCO_3$ and $MnO_2$ powders were mixed thoroughly and calcined at 1373 K for 24 hours in air. The resulting samples were pulverized, pressed into pellets and sintered twice at 1473 K for 24 hours with an intermediate pulverizing. The samples were again pulverized, and then sintered for a third time at 1473 K for 48 hours. The samples are single phase with orthorhombic crystal structure, as confirmed by X-ray diffraction analysis (see Fig. 4.1). The resistance of the samples were measured using the four probe method with silver contacts that are sputtered using RF magnetron source onto the samples. The results reported in this chapter were primarily on samples that were rectangular in shape with dimensions $10.0 \times 1.42 \times 0.74$ mm$^3$ (for $x = 0.40$) and $10.0 \times 1.68 \times 0.99$ mm$^3$ (for $x = 0.45$). (Other samples of these two compositions were also measured with similar results.) They were mounted

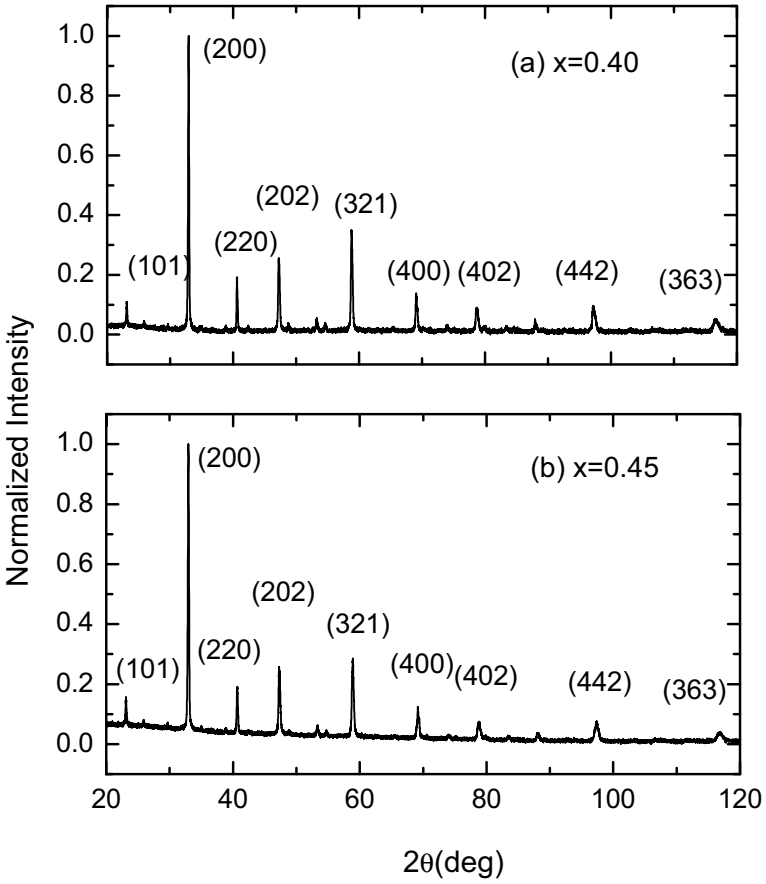


Figure 4.1: X-ray diffraction pattern at room temperature for $Sm_{1-x}Sr_xMnO_3$: (a) $x = 0.40$ and (b) $x = 0.45$. The intensity of each peak was normalized to the (200) peak intensity.

on a copper block (cold-finger) located in a vacuum cryostat that is attached to a closed-cycle cryocooler. The temperature of the block, $T$, is monitored either with a GaAlAs or Pt thermometer. A Keithley 6221 AC/DC current source was used to supply current pulses to the samples. The voltage across the samples, which is needed to calculate the ER, was measured with either a Keithley 2182A nanovoltmeter or a Tiepie HS3 high resolution USB oscilloscope. The nanovoltmeter was particularly useful for measuring the small voltage drops at low current excitation (where Joule heating is also very minimal), because it can measure the small voltage drops more precisely than the

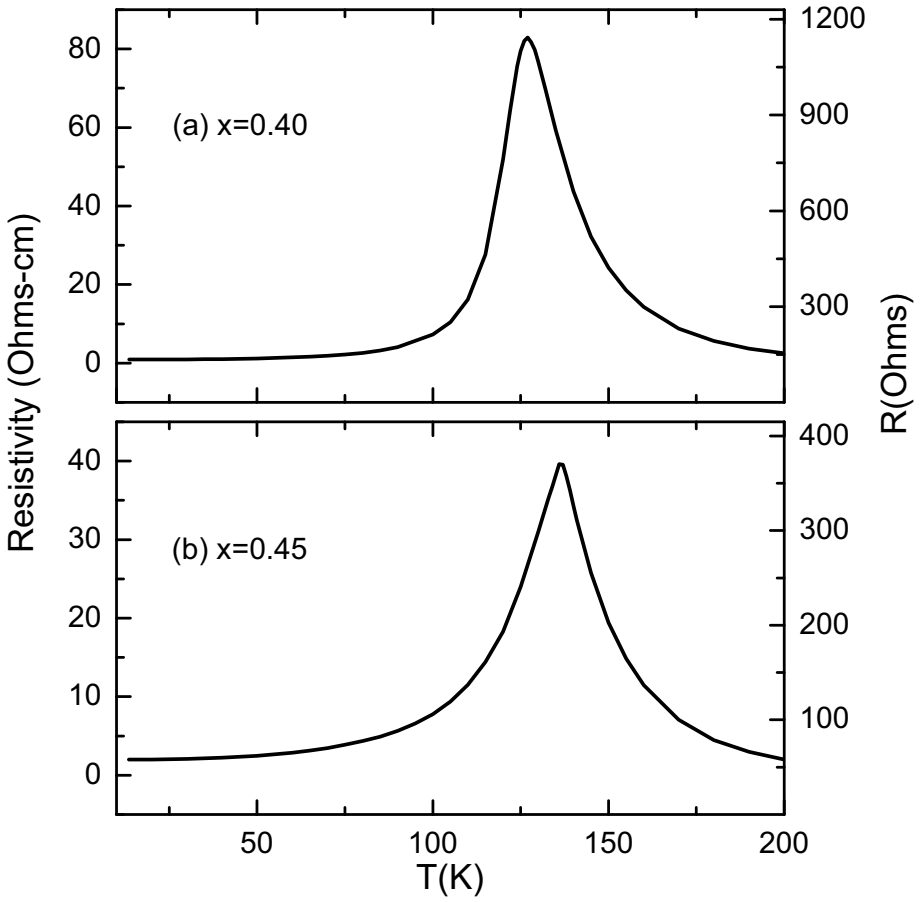


Figure 4.2: The temperature dependence of resistivity (and resistance) acquired during warming for $Sm_{1-x}Sr_xMnO_3$: (a) $x = 0.40$ and (b) $x = 0.45$. The data are obtained using low current (1mA).

oscilloscope. In order to confirm that we are indeed measuring the intrinsic voltage drops (i.e., without contribution of Joule heating) at low currents, we established that there is no change in the voltage (and hence resistance or resistivity) with the width of the current excitation pulse in our samples (see Fig. 3.5(c) in Chapter 3 for details). The oscilloscope was used to measure the voltage at higher current excitations, because it was advantageous over the nanovoltmeter to inspect and analyze the time dependence of the voltage across the sample for high currents. The time dependence of the voltage was recorded and subsequently analyzed to estimate the intrinsic ER (see below).

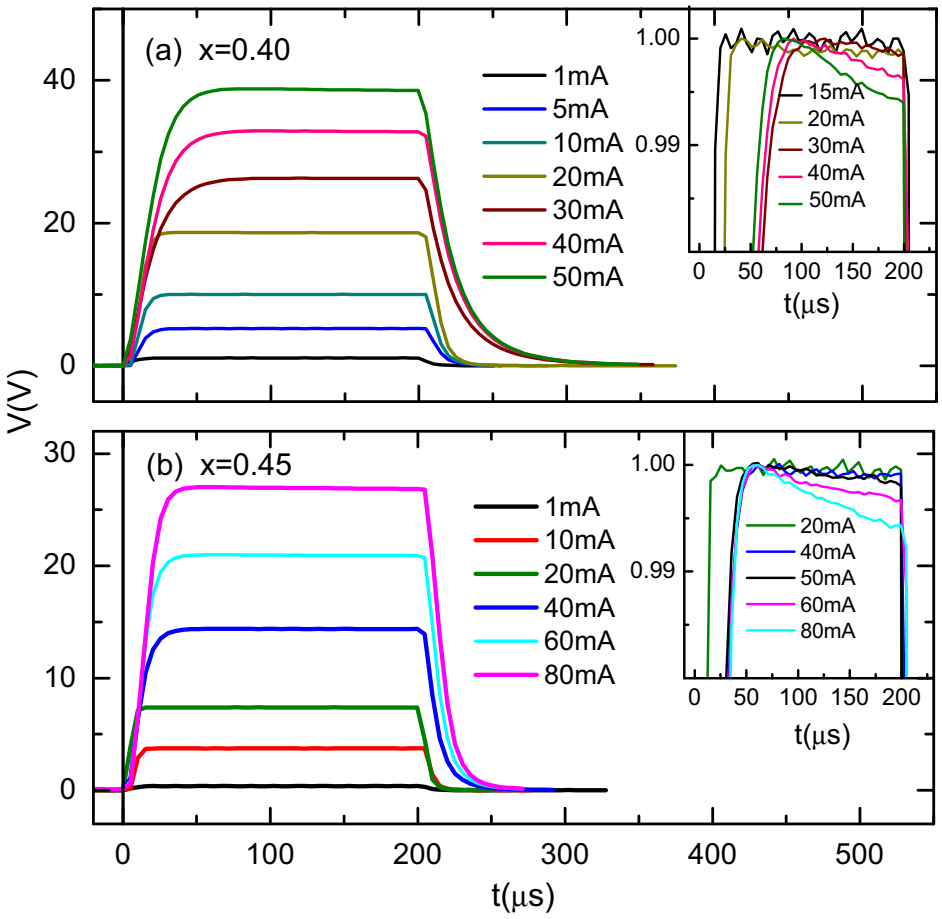


Figure 4.3: Voltage vs time acquired at various current excitations using 200 $\mu$s pulses at the $T_{MI}$s for $Sm_{1-x}Sr_xMnO_3$: (a) $x = 0.40$ and (b) $x = 0.45$. The insets show the normalized voltage vs time for the two samples.

Fig. 4.2 (a) and 4.2(b) show the temperature dependent resistance (and resistivity) for our $x = 0.40$ and $x = 0.45$ samples, measured using low current excitation. The $T_{MI}$s are $\approx$ 127 K and 137 K for the $x = 0.40$ and $x = 0.45$ samples, respectively. We now discuss in more detail our methodology for estimating the intrinsic ER; this is not a trivial issue because significant Joule heating can be present at high currents in our samples, and in the manganites in general, e.g., Ref. [20]. Our approach is based primarily on inspection and analysis of the oscilloscope traces of the time dependence of the voltage across the sample, such as those shown in Fig. 4.3 near the $T_{MI}$s of the two

compositions (for a 200 $\mu$s pulse). (The voltage or resistance measurements as a function of width of the current pulses were discussed in previously in chapter 3, section 3.3.1). In the examples shown in Fig. 4.3, there is a time-interval where the voltage rises (related to the rise time of the current from the source), followed by a plateau-like region, then a subsequent decay of the voltage (after 200 $\mu$s) towards zero. At the lower currents, e.g. below $\sim 20$ mA for $x = 0.40$ and $\sim 50$ mA for $x = 0.45$, there is no obvious time dependence in the plateau-like region (see inset of Fig. 4.3); its flatness indicates that Joule heating is not important here. In these situations, the (average) voltage of the plateau-like region is equivalent to the "intrinsic" voltage drop across the sample. However, at higher currents, there is a clear decrease of the voltage in the plateau-like regime, implying that Joule heating is playing a progressively more prominent role, i.e., the internal temperature of the sample is rising.

In order to obtain a reasonable estimate of the intrinsic ER for each current pulse, we use the average of two values: The first of these values is the average of the voltages within the pulse away from the rise and decay edges. If there is significant Joule heating which causes a decrease in the voltage in the plateau-like region, then this value underestimates the intrinsic voltage. The second of these values is the extrapolation of the voltage data back to the start of the pulse at $t = 0$ (using a phenomenological function, e.g., consisting of an exponential decay plus a constant, etc.), as exemplified in Fig. 4.4. This approach would likely overestimate the intrinsic voltage since Joule heating should only become significant during part of the rising edge of the current pulse; hence, this second value should be viewed as an upper limit on the intrinsic voltage. The difference between the two values provides an estimate of the "error" in our estimate of the intrinsic voltage or resistance.

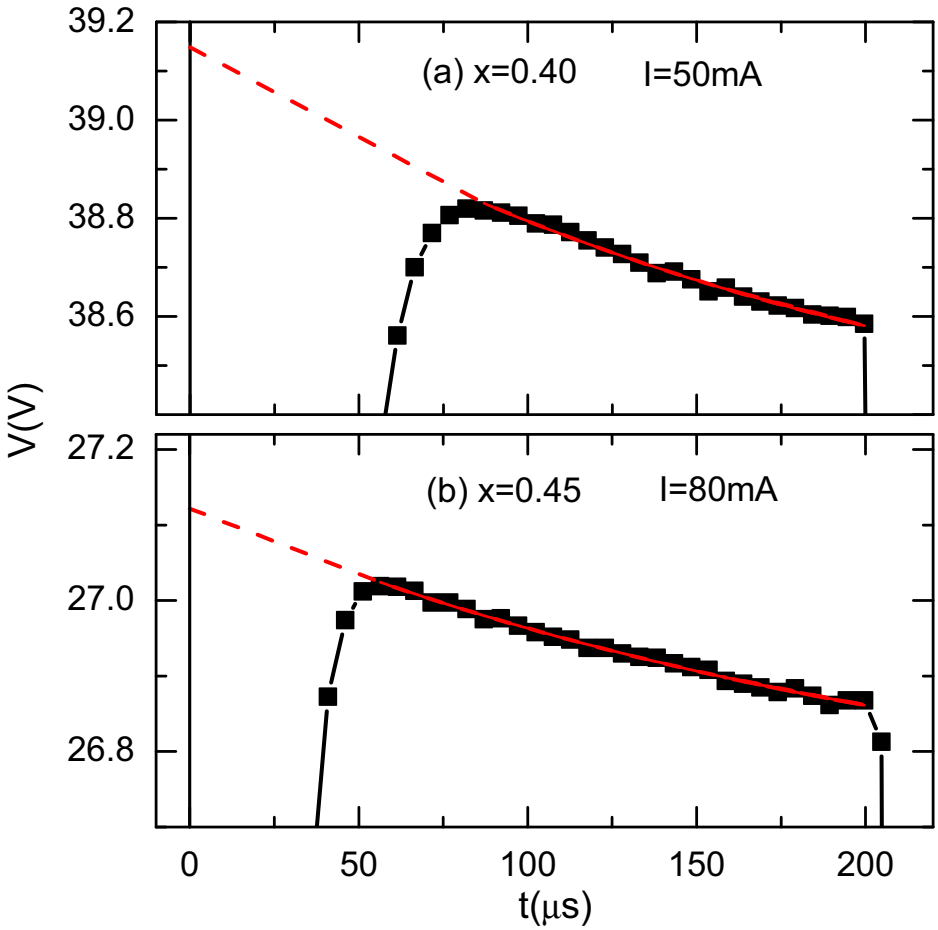


Figure 4.4: Examples of the extrapolation used at higher currents, as part of the procedure used to extract the intrinsic voltage (see text), in the $Sm_{1-x}Sr_xMnO_3$ samples: (a) $x = 0.40$ and (b) $x = 0.45$.

## 4.3 Results and discussion

### 4.3.1 Intrinsic Electroresistance

Fig. 4.5(a) and 4.5(b) show the temperature dependence of the intrinsic resistance $R(T)$ (and resistivity $\rho(T)$), estimated as described above using 200 $\mu$s pulses, of our $x = 0.40$ and $x = 0.45$ samples, respectively, while warming from base temperature. Each temperature/current data point in Fig. 4.5 was obtained from the off-line analysis of the relevant recorded oscilloscope trace.

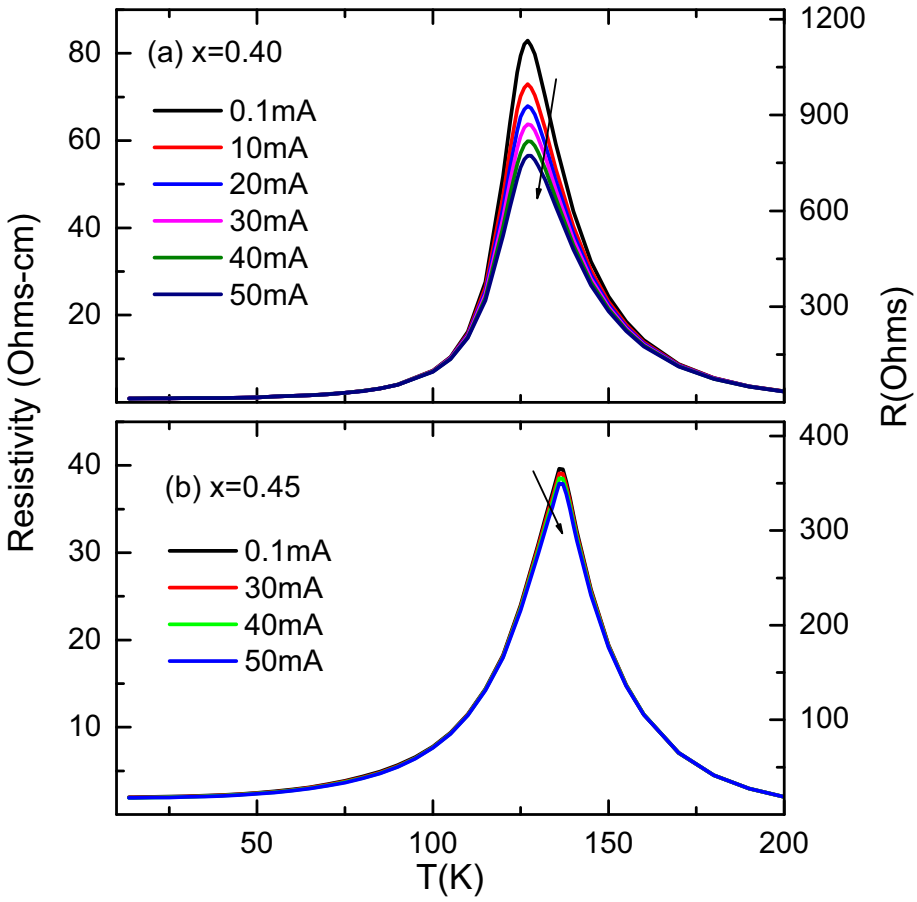


Figure 4.5: Resistance/resistivity vs temperature acquired during warming for $Sm_{1-x}Sr_xMnO_3$: (a) $x = 0.40$ and (b) $x = 0.45$. The data are obtained using 200 $\mu$s current pulses.

Fig. 4.5(a) should be contrasted with the results on SSMO $x = 0.40$ reported by Rebello *et al.* [14] who measured the ER for this composition using dc current. They observed large changes in the resistivity and significant shifting of $T_{MI}$ to lower temperature with higher current strength (see Fig. 1.2 in Chapter 1). (We also see similar behavior if we use dc current excitation (see Fig. 3.5(a) in Chapter 3).) By contrast, as seen in Fig. 4.5(a), if the Joule heating contribution is minimized, there are much smaller reductions of the resistivity, and virtually no shift in $T_{MI}$ ($\approx$ 127 K). Analogous results are obtained for the other (i.e., $x = 0.45$) sample: there is a decrease in the

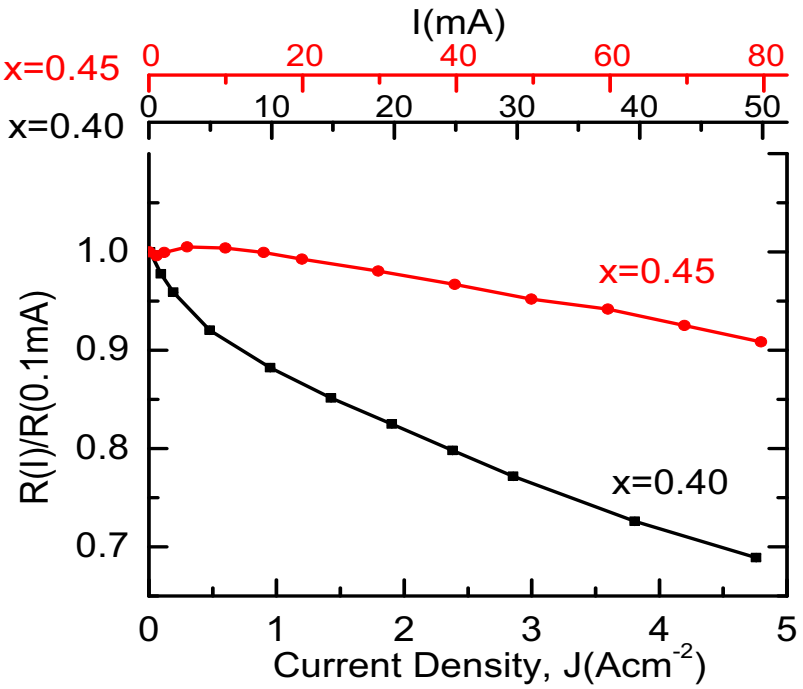


Figure 4.6: $R(I)/R(0.1mA)$ vs current density for $Sm_{1-x}Sr_xMnO_3$ at the $T_{MI}$s of the samples.

peak resistivity and virtually no shift in $T_{MI}$ ($\approx$ 137 K) for the short-pulse excitation (see Fig. 4.5(b)). Interestingly, our estimates of the intrinsic ER in $Sm_{0.55}Sr_{0.45}MnO_3$ is many orders of magnitude smaller than those reported by Mohan *et al.* [16](see Fig. 1.3 in Chapter 1) - we will return to a discussion of this result below.

Although both samples have an intrinsic electro-resistance, Figs. 4.5(a) and 4.5(b) suggest that the changes of the resistance with the magnitude of the current is significantly smaller for the $x = 0.45$ sample. Indeed, Fig. 4.6 clearly shows that at the $T_{MI}$ of the samples, the intrinsic changes of the resistance with current density (and also current) are significantly larger in $Sm_{0.60}Sr_{0.40}MnO_3$ than in $Sm_{0.55}Sr_{0.45}MnO_3$. For example, the changes in the ER, defined as $[(R(0.1mA) - R(I))/R(I)] \times 100\%$ is found to be $\sim$45% and $\sim$9.5% for $x = 0.40$ and $x = 0.45$ respectively at 4.8 A/cm$^2$.

A possible mechanism for this dramatic difference is now discussed: Gen-

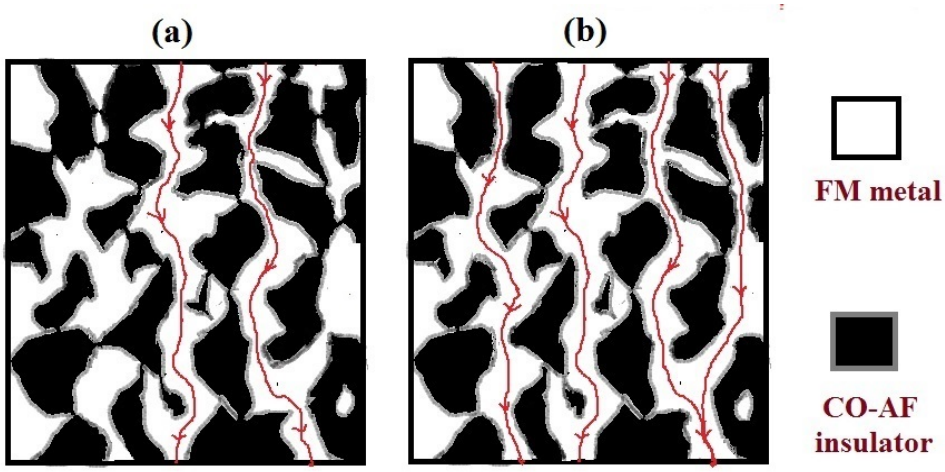


Figure 4.7: Schematic illustration of the coexistence of the ferromagnetic (FM) metallic phase (white area) and charge ordered antiferromagnetic (CO-AF) insulating phase (black area) and percolative conduction paths in an inhomogenious manganite system at fixed temperature for (a) low current/electric field, and (b) high current/ electric field. The red lines present the flowing current through the filamentous percolated paths (or in an inter connected FM metallic regions). In particular, Fig. 4.7(b) shows the formation of new percolative conduction paths in a phase separated sample at high current excitation.

erally, current percolation through internal inhomogeneities is considered to be important for ER. For example, the change in electrical resistance may be associated with the current-induced "melting" of charge ordered AF clusters which can enhance the volume of the ferromagnetic metallic (FMM) state as well as the percolative conduction paths [28] (see Fig. 4.7). Hence, it is reasonable to expect that the ratio of FMM and AF phases within the sample will be an important parameter for determining the amount of ER. Recent measurements on SSMO have noted that at low temperatures, the $x = 0.40$ sample has a phase-separated FMM ground state with A-type AF and small amounts of CE-type (charge ordered) AF clusters [25, 26, 27] whereas the low temperature ground state for $x = 0.45$ is a homogeneous FMM [26, 27] (see Fig. 1.1 in Chapter 1 for the phase diagram of $Sm_{1-x}Sr_xMnO_3$). (This is consistent with our observation that our $x = 0.45$ sample has a lower peak

resistivity and higher $T_{MI}$ than the $x = 0.40$ sample.) Hence, it is reasonable to expect that the current will have a larger effect for the more inhomogenous composition, i.e., $x = 0.40$.

Finally, we return to the results of Mohan *et al.* [16] regarding the intrinsic ER of SSMO $x = 0.45$. While an ER of $\approx 10$ % is observed in our present study, they reported changes on the order of thousands of percent at comparable current densities. The huge discrepancy between our measurements and those of Ref. [16], which are also significantly larger than the ER of many other manganites, is puzzling and not fully understood at this time. The morphology of the polycrystalline bulk samples, which are sensitive to the preparation conditions, as well as the quality of the contacts used for the electrical transport measurements are just some of the factors that govern their resistivities and their evolution with the magnitude of the current (the sample in Ref. [16] has higher resistivity and lower $T_{MI}$ than ours).

### 4.3.2 Current Density and Intrinsic Electroresistance

To establish the controlling parameter for analyzing intrinsic ER, we experimentally investigated the role of geometry on the current and current density dependencies of the intrinsic electroresistance of SSMO. The results reported in this section were done primarily on samples that were rectangular in shape (see Fig. 4.8(a)) with two different geometrical dimensions for each composition: $10.0 \times 2.13 \times 1.24$ mm$^3$ and $10.0 \times 1.73 \times 0.91$ mm$^3$ for $x = 0.40$, and $10.0 \times 1.68 \times 0.99$ mm$^3$ and $10.0 \times 0.90 \times 0.41$ mm$^3$ for $x = 0.45$. Note, therefore, that the two samples for each composition have the same length L, but have different width W and height H, and hence different cross-sectional areas. The resistance of the samples was measured using the four probe method with silver contacts that were sputtered using a RF magnetron source onto the samples. In order to ensure that the current flows uniformly through the cross-sectional area of the sample, the ends of the bar-shaped sample were

covered with silver (see Fig. 4.8(a)).

Fig. 4.8 and Fig. 4.9 show the temperature dependence of the intrinsic resistance $R(T)$ and resistivity $\rho(T)$ for the $x = 0.40$ and $x = 0.45$ samples, respectively. Note that, as expected, the two geometrically distinct samples within each composition ($x = 0.40$ and $x = 0.45$) have different resistances since they have different cross-sectional areas. However, they have (i) very similar resistivities (see Fig. 4.8(b) and Fig. 4.9(b)) and (ii) the same metal insulator transition temperatures ($T_{MI}$) of $\approx$ 125 K and $\approx$ 137 K for the

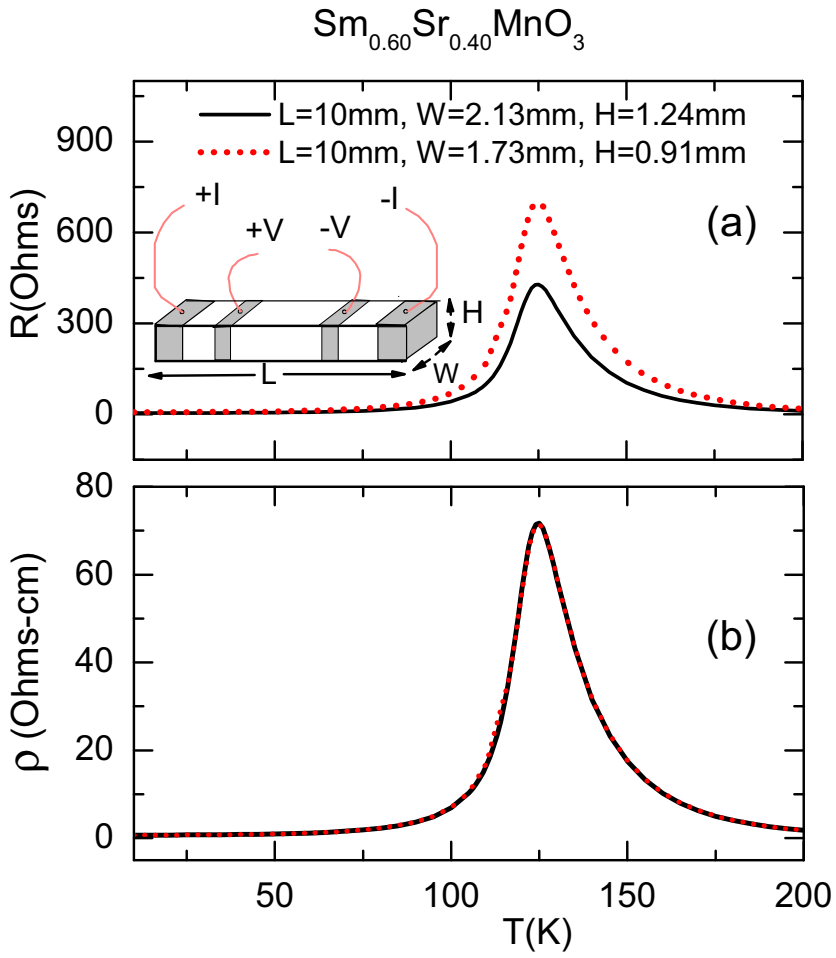


Figure 4.8: (a) Resistance (R) vs temperature (T), and (b) resistivity ($\rho$) vs temperature for $Sm_{0.60}Sr_{0.40}MnO_3$. The inset shows the geometrical dimensions of the samples.

$x = 0.40$ and $x = 0.45$ samples, respectively. This indicates that preparation conditions of these four samples have not introduced any defects or imperfections that could significantly change their transport properties.

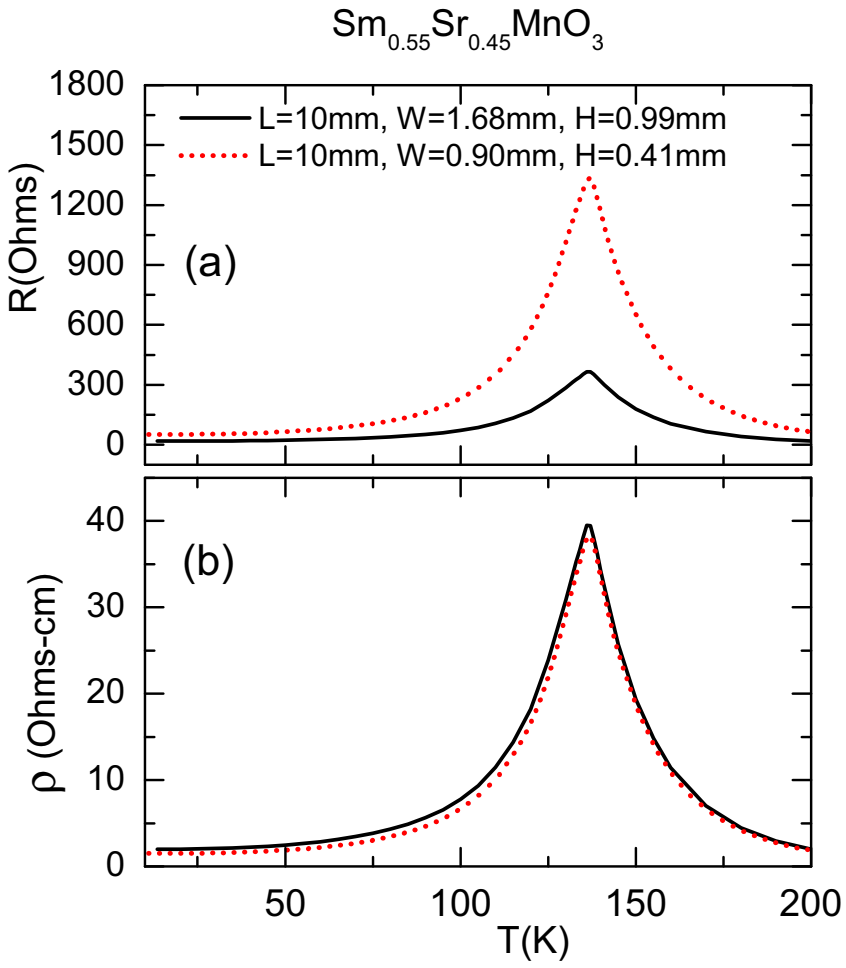


Figure 4.9: (a) Resistance (R) vs temperature (T), and (b) resistivity ($\rho$) vs temperature for $Sm_{0.55}Sr_{0.45}MnO_3$.

The data shown in Fig. 4.10 and 4.11 experimentally establish whether it is the current or the current density that governs the behavior of the intrinsic ER, as we will explain below. In the figure, the ER of the sample is represented by the normalized resistance/resistivity $R(I)/R(0.1mA)$.

Fig. 4.10(a) and 4.10(b) show the ER vs the current (I) for the same $x = 0.40$ and $x = 0.45$ samples shown in Fig. 4.8 and 4.9, measured at their $T_{MI}$. By

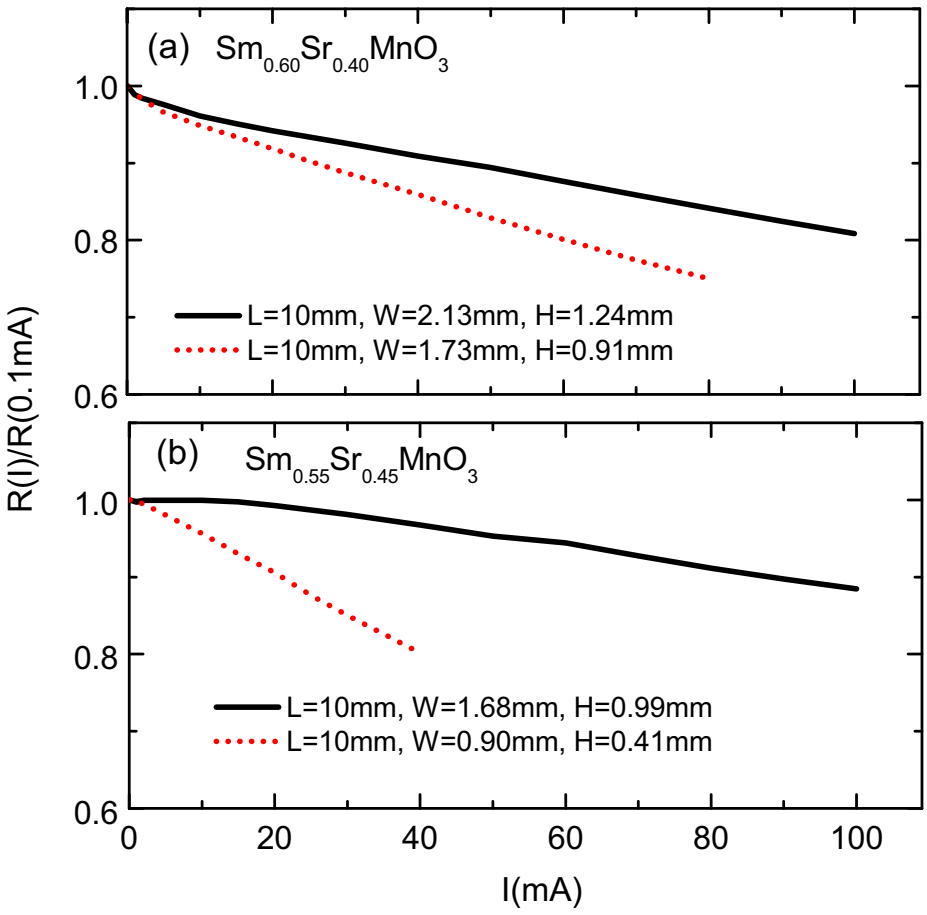


Figure 4.10: The current (I) dependence of $R(I)/R(0.1mA)$ for (a) $Sm_{0.60}Sr_{0.40}MnO_3$ and (b) $Sm_{0.55}Sr_{0.45}MnO_3$ at the $T_{MI}$s of the samples.

contrast, Fig. 4.11 shows the dependence of their ER on the current density (J). Clearly, the normalized resistances of the samples of each composition do not coincide when plotted against the magnitude of the current (see Fig. 4.10(a) and 4.10(b)). However, they agree very well when plotted against the current density (see Fig. 4.11). This confirms that it is indeed the current density, rather than the magnitude of the current, that globally determines the values of the intrinsic ER in a particular composition of $Sm_{1-x}Sr_xMnO_3$.

Note that Joule heating is more pronounced in samples with higher resistance, i.e., its contribution to the measured voltage is larger. However, the

fact that plots of the normalized resistance versus current density for samples with different resistances coincide (see Fig. 4.11) confirm that the influence of Joule heating is minimal and the estimated ER is indeed an "intrinsic" one. Furthermore, Fig. 4.11 shows that the changes of intrinsic ER are significantly larger in the $x = 0.40$ compared to the $x = 0.45$ compositions. The relative change in ER with compositions ($x = 0.40$ and $x = 0.45$) are consistent with findings reported in the previous section 4.3.1.

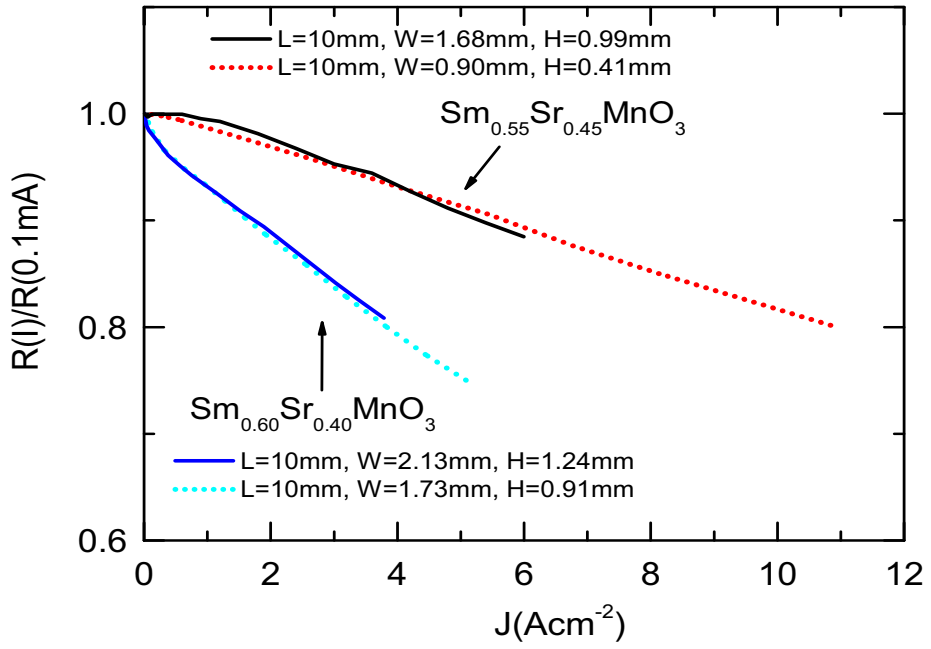


Figure 4.11: The current density (J) dependence of $R(I)/R(0.1mA)$ for $Sm_{0.60}Sr_{0.40}MnO_3$ and $Sm_{0.55}Sr_{0.45}MnO_3$ at the $T_{MI}$s of the samples.

## 4.4 Summary

In summary, we have investigated the intrinsic electroresistance of $Sm_{0.60}Sr_{0.40}MnO_3$ and $Sm_{0.55}Sr_{0.45}MnO_3$ synthesized in the same way. This electroresistance depends on the magnitude of the current, and undergoes larger changes in the $x = 0.40$ sample compared to the $x = 0.45$ sample. We attribute this

difference to the contrasting homogeneity of these two compositions. Our estimates of the electroresistance are dramatically smaller than those previously measured for the same compositions by others [14, 16].

# Bibliography


[1] Y. Tomioka, X. Z. Yu, T. Ito, Y. Matsui, and Y.Tokura, Phys. Rev. B **80**, 094406 (2009).

[2] Y. Tokura, Rep. Prog. Phys. **69**, 797 (2006).

[3] E. Dagotto, T. Hotta, and A. Moreo, Phys. Rep. **344**, 1 (2001).

[4] C. N. R. Rao and P. V. Vanitha, Curr. Opin. Solid State Mater. Sci. **6**, 97 (2002).

[5] M. Egilmez, K.H. Chow, and J.A. Jung, Mod. Phys. Lett. B, **25**, 697 (2011); M. Egilmez, K.H. Chow, J. Jung, and Z. Salman, Appl. Phys. Lett., **90**, 162508 (2007).

[6] M. Egilmez, K.H. Chow, J. Jung, and Z. Salman, Appl. Phys. Lett., **90**, 162508 (2007).

[7] Y. Tokura and N. Nagaosa, Science **288**, 462 (2000).

[8] L. Hu, Y. P. Sun, B. Wang, Z. G. Sheng, X. Luo, X. B. Zhu, Z. R. Yang, W. H. Song, J. M. Dai, Z. Z. Yin, and W. B. Wu, J. Appl. Phys. **106**, 083903 (2009).

[9] A. Asamitsu, Y. Tomioka, H. Kuwahara, and Y. Tokura, Nature **388**, 50 (1997).

[10] A. Odagawa, T. Kanno, H. Adachi, H. Sato, I. H. Inoue, H. Akoh, M. Kawasaki, and Y. Tokura, Thin Solid Films **486**, 75 (2005).

[11] Y. Yamato, M. Matsukawa, Y. Murano, R. Suryanarayanan, S. Nimori, M. Apostu, A. Revcolevschi, K. Koyama, and N. Kobayashi, Appl. Phys. Lett. **94**, 092507 (2009).

[12] H. Jain and A. K. Raychaudhuri, Appl. Phys. Lett. **93**, 182110 (2008).

[13] A. Rebello and R. Mahendiran, Appl. Phys. Lett. **94**, 112107 (2009).

[14] A. Rebello and R. Mahendiran, Appl. Phys. Lett. **96**, 152504 (2010).

[15] A. A. Wagh, P. S. A. Kumar, H. L. Bhat, and S. Elizabeth, J. Appl. Phys. **108**, 063703 (2010).

[16] R. Mohan, N. Kumar, B. Singh, N. K. Gaur, S. Bhattacharya, S. Rayaprol, A. Dogra, S. K. Gupta, S. J. Kim, and R. K. Singh, J. Alloys and Compd. **508**, L32 (2010).

[17] Y. Nishi, Current Applied Physics **11**, e101 (2011).

[18] Y. F. Chen, M. Ziese, and P. Esquinazi, Appl. Phys. Lett. **88**, 222513 (2006).

[19] A. S. Carneiro, R. F. Jardim, and F.C. Fonseca, Phys. Rev. B **73**, 012410 (2006).

[20] S. Mercone, R. Frésard, V. Caignaert, C. Martin, D. Saurel, C. Simon, G. André, P. Monod, and F. Fauth, J. Appl. Phys. **98**, 023911 (2005).

[21] C. Martin, A. Maignan, M. Hervieu, and B. Raveau, Phys. Rev. B **60**, 12191 (1999).

[22] Y. Tomioka, H. Hiraka, Y. Endoh, and Y. Tokura, Phys. Rev. B **74**,104420 (2006).

[23] M. Egilmez, M. M. Saber, A. I. Mansour, R. Ma, K. H. Chow, and J. Jung, Appl. Phys. Lett. **93**, 182505 (2008).

[24] B. Fisher, J. Genossar, K. B. Chashka, L. Patlagan, and G. M. Reisner, Appl. Phys. Lett. **88**, 152103 (2006).

[25] I. D. Luzyanin, V. A. Ryzhov, D. Yu. Chernyshov, A. I. Kurbakov, V. A. Trounov, A. V. Lazuta, V. P. Khavronin, I. I. Larionov, and S. M. Dunaevsky, Phys. Rev. B **64**, 094432 (2001).

[26] A. I. Kurbakov, A. V. Lazuta, V. A. Ryzhov, V. A. Trounov, I. I. Larionov, C. Martin, A. Maignan, and M. Hervieu, Phys. Rev. B **72**, 184432 (2005).

[27] A. I. Kurbakov, J. Magn. Magn. Mater. **322**, 967 (2010); A. I. Kurbakov, A.V. Lazuta, and V. A. Ryzhov, J. Phys.: Conf. Ser. **200**, 012099 (2010).

[28] H. Sakai and Y.Tokura, Appl. Phys. Lett. **92**, 102514 (2008).

# Chapter 5

# Disorder enhanced intrinsic electroresistance in $\mathbf{Sm_{0.60}Sr_{0.40}Mn_{1-}}_x\mathbf{Fe}_x\mathbf{O_3}$

## 5.1 Introduction

Consider $Sm_{1-x}Sr_xMnO_3$ (SSMO), a system where multiphase competition plays a prominent role in driving their magnet-transport properties [1, 2, 3, 4, 5]. From the investigations of SSMO (see chapter 4), we found that the changes of the intrinsic electroresistance with current density are much more significant in $Sm_{0.60}Sr_{0.40}MnO_3$ compared to $Sm_{0.55}Sr_{0.45}MnO_3$, hinting that spatial inhomogeneities related to the multiphase coexistence are important to determine the intrinsic ER in SSMO. It is therefore interesting to further address the extent to which the intrinsic ER in these manganites can be tuned by the amount of inhomogeneity/disorder in these systems, and to probe the possible mechanisms involved.

To achieve this goal, we have systematically investigated the intrinsic ER in a series of Fe doped $Sm_{0.60}Sr_{0.40}Mn_{1-x}Fe_xO_3$ samples. (Since $Sm_{0.60}Sr_{0.40}MnO_3$ shows relatively larger intrinsic ER than $Sm_{0.55}Sr_{0.45}MnO_3$, we have chosen

$Sm_{0.60}Sr_{0.40}MnO_3$ as a parent compound to investigate the ER). The substitution of Fe for Mn (also referred to as Mn-site or B-site doping) has attracted considerable interest since the ionic size of $Fe^{3+}(3d^5{:}t_{2g}^3e_g^2$ high spin) is almost identical to that of $Mn^{3+}(3d^4{:}t_{2g}^3e_g^1)$ [6, 7, 8, 9, 10]. This minimizes the effects of lattice distortion upon substitution, and more readily reveals phenomena associated with changes in the electronic configuration. For example, the existence of a small amount of Fe, randomly distributed in the manganites, has been responsible for the formation of different size-distributed magnetic clusters, super-paramagnetic clusters, random canting of spins or spin-glass like behavior, etc [6, 11, 12, 13, 14, 15].

Furthermore, it is known from other experimental measurements (such as Mössbauer spectra measurements) that Fe ions in manganites prefer to be in the high-spin trivalent state, they have half filled very stable 3d-state ($3d^5$), and there is antiferromagnetic coupling between Fe and Mn ions [16, 17]. Replacing $Mn^{3+}$ with $Fe^{3+}$ and the antiferromagnetic (AF) coupling between $Fe^{3+}$ and $Mn^{4+}$ ions lead to a competition between the AF superexchange and ferromagnetic metallic (FMM) interactions between $Mn^{3+}$ and $Mn^{4+}$ ions. Consequently, the hopping/double exchange mechanism is less effective, which in turn increases the resistivity and decreases the metal-to-insulator temperature $T_{MIT}$ of the system [17].

## 5.2 Experimental Procedure

Polycrystalline $Sm_{0.60}Sr_{0.40}Mn_{1-x}Fe_xO_3$ samples with $x = 0, 0.005, 0.01$, 0.015, and 0.02 were prepared using the same solid state reaction method: a prescribed ratio of $Sm_2O_3$, $SrCO_3$, $MnO_2$ and $Fe_2O_3$ powders were mixed thoroughly and calcined at 1100 $^o$C (1373 K) for 24 hours in air. The resulting samples were pulverized, pressed into pellets and sintered twice at 1200 $^o$C (1473 K) for 24 hours with an intermediate pulverizing. The samples were

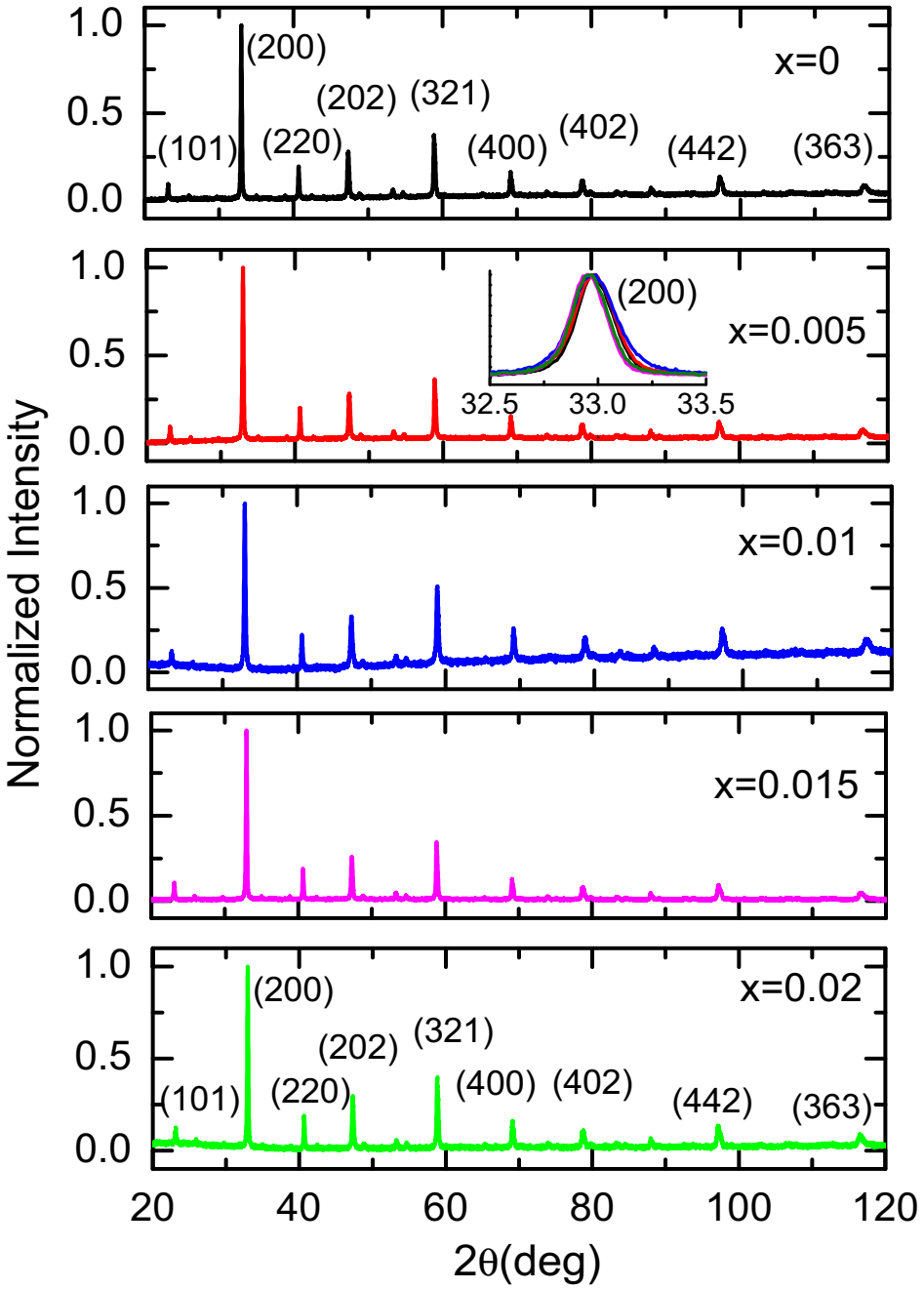


Figure 5.1: X-ray diffraction patterns at room temperature for $Sm_{0.60}Sr_{0.40}Mn_{1-x}Fe_xO_3$ (SSMFO) ($x = 0, 0.005, 0.01$, 0.015, and 0.02 ). The intensity of each peak was normalized to the (200) peak intensity. The inset shows the (200) peak for all SSMFO compositions.

again pulverized, and then sintered for a third time at 1200 $^o$C for 48 hours. X-ray diffraction analysis confirmed that all the samples are single phase with the orthorhombic Pbnm structure (see Fig. 5.1). The inset of Fig. 5.1 shows the (200) peak for all the $Sm_{0.60}Sr_{0.40}Mn_{1-x}Fe_xO_3$ (SSMFO) ($x = 0, 0.005, 0.01,$ 0.015, and 0.02 ) compositions; It is found that there is no discernable change in peak positions compared to the parent compound ($x = 0$).

The resistance of the rectangular shaped samples was measured using the four probe method with silver contacts that are RF-magnetron-sputtered onto the samples. They are mounted on a copper block (cold-finger) located in a vacuum cryostat that is attached to a closed-cycle cryocooler. The temperature of the block, $T$, is monitored with a Cernox thermometer. Since our goal is to measure the *intrinsic* ER in the samples, Joule heating must be minimized. This was achieved using a technique described in detail in Chapter 4. The temperature dependence of ac magnetic susceptibility $\chi(T)$, was measured for the warming cycle at a frequency of 1997 Hz and in a zero magnetic field . $T_c$ was determined using the gradient method ( see Fig. 3.7 in Chapter 3).

## 5.3 Results and discussion

The temperature dependence of the intrinsic resistivity $\rho(T)$ of the polycrystalline $Sm_{0.60}Sr_{0.40}Mn_{1-x}Fe_xO_3$ ($0 \leqslant x \leqslant 0.02$) samples measured in a magnetic field of H = 0 T and H = 1.1 T (during warming from the base temperature of 10 K) is shown in Fig. 5.2 and 5.3, respectively. (Samples with $x > 0.02$ have either very high resistivity at the $T_{MIT}$ or are insulating; therefore, they have not been investigated in detail.) A metal-to-insulator (MIT) transition occurs at $T_{MIT}$ in all the samples, and $T_{MIT}$ decreases significantly with increasing Fe concentration. Such behavior is qualitatively consistent with previous studies of $Sm_{0.60}Sr_{0.40}MnO_3$, which have shown that 5% of Fe is sufficient to completely "destroy" the FMM phase [17]. Fig. 5.2 also illustrates

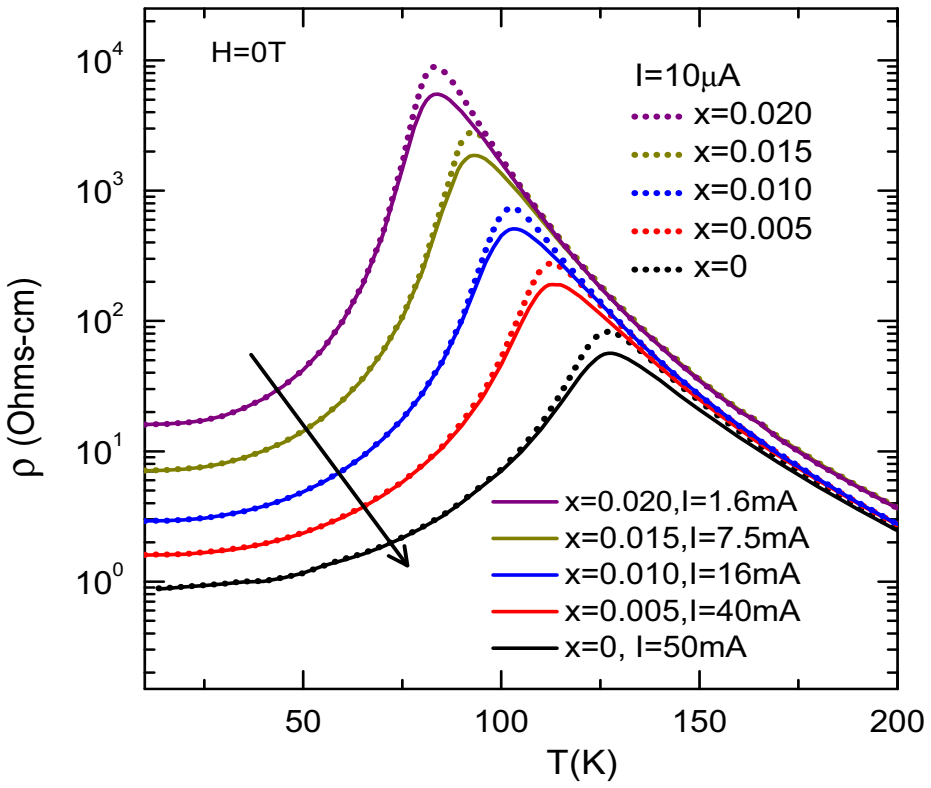


Figure 5.2: Resistivity vs temperature $\rho(T)$, in the absence of an applied magnetic field, acquired during warming, for $Sm_{0.60}Sr_{0.40}Mn_{1-x}$ $Fe_xO_3$. The dotted lines are for low currents $\rho(T)$, and the solid lines are for high currents $\rho(T)$. The arrows indicate the trend as $x$ decreases from 0.020 to 0.

that there is significant electroresistance, i.e., the $\rho(T)$ changes with the magnitude of the applied current; in all the samples, there is virtually no change in the position of the $T_{MIT}$ with current. Furthermore, $\rho(T)$ measured for low currents shows that there is significant magnetoresistance in the samples: increasing the magnetic field leads to a decrease in the peak resistivity and a shift of the $T_{MIT}$ to higher temperatures ( see Fig. 5.3).

The normalized resistivity, $\rho(I)/\rho(10\mu A)$ vs current density (J) for $Sm_{0.60}$ $Sr_{0.40}Mn_{1-x}Fe_xO_3$, measured in H = 0 T and H = 1.1 T at their $T_{MIT}$'s, are shown in Fig. 5.4(a) and Fig. 5.4(b), respectively. At both magnetic fields, a significant ER is observed. It increases with an increasing Fe content $x$. If the

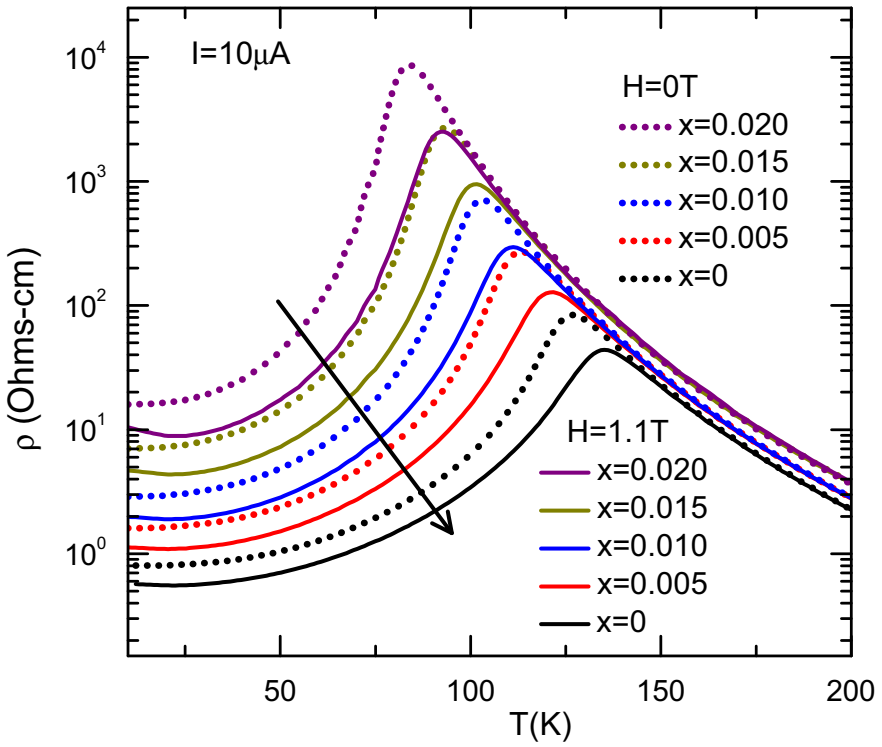


Figure 5.3: Resistivity vs temperature $\rho(T)$, at low currents, acquired during warming, for $Sm_{0.60}Sr_{0.40}Mn_{1-x}Fe_xO_3$. The dotted lines are for $\rho(T)$ in zero magnetic field, and the solid lines are for $\rho(T)$ in a magnetic field of 1.1T. The arrows indicate the trend as $x$ decreases from 0.020 to 0.

sample with a particular value of $x$ is subjected to a magnetic field, its ER at the $T_{MIT}$ is reduced. These observations are summarized in Fig. 5.4(c), which shows the numerical values of the ER (defined as $[(\rho(10\mu A) - \rho(I))/\rho(I)] \times 100\%$) as a function of Fe content at a current density of J=0.060 A/cm$^2$ for H = 0 T and H = 1.1 T. Note that at a constant magnetic field, the ER increases with $x$ while at a particular value of the Fe content, the ER in an applied field of H = 1.1 T is smaller than in a zero field.

There appears to be a clear correlation between the ER and the extent of the inhomogeneities in the samples. In particular, as shown in Fig. 5.5, there is a hysteresis in the $\rho(T)$ of our samples during warming from a base temperature to temperatures well above the metal-insulator transition, followed by cooling. The thermal hysteresis width $\Delta$T, defined in the figure, and the ra-

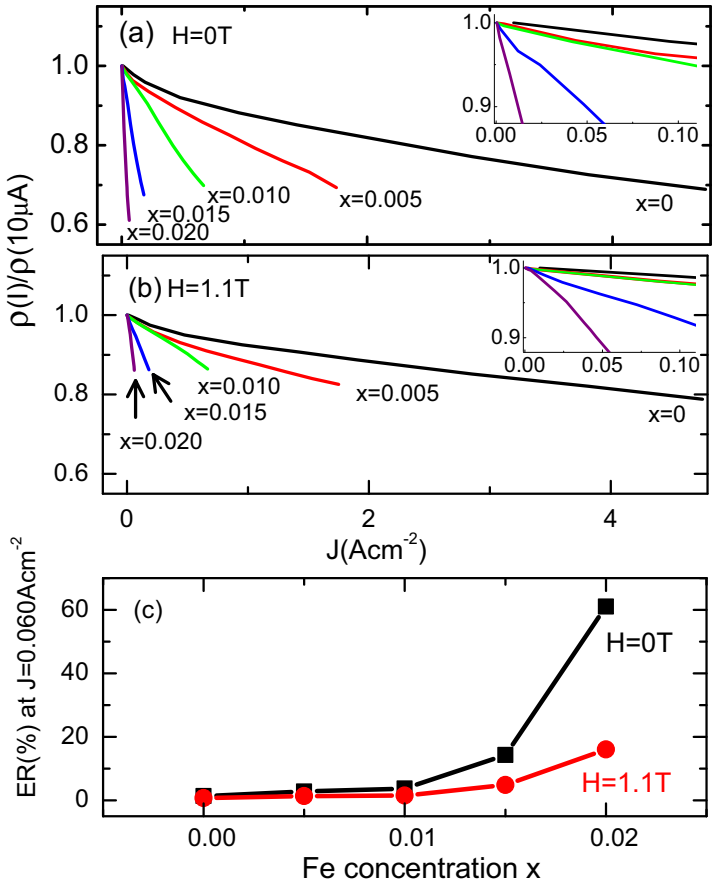


Figure 5.4: $\rho(I)/\rho(10\mu A)$ vs current density for $Sm_{0.60}Sr_{0.40}Mn_{1-x}Fe_xO_3$ measured in (a) H = 0 T and (b) H = 1.1 T at their $T_{MIT}$. The insets in Fig. 5.3(a) and Fig. 5.3(b) show the expanded low current density regions . The data are obtained after warming to the MIT. (c) Intrinsic ER, at J=0.060A/cm$^2$, vs Fe content in H=0 T and H=1.1 T.

tio of the peak resistivity values during cooling and warming, i.e., $Res_{c/w}$, are measures of the amount of inhomogeneities/disorder in a manganite [18]. In general, the thermal hysteresis in the $\rho(T)$ curve indicates the inhomogeneous magnetic/electronic state (i.e., coexistence of FM metallic (FMM) and AF insulating (AFI) clusters) in the sample [19]. The electrical conductivity in the sample can be understood by considering the percolation process via the FMM clusters (see chapter 2, section 2.6 for the percolation in a phase separation scenerio). Consequently, the sample's resistivity ($\rho$) and the metal-insulator transition temperature ($T_{MIT}$) depend on the total concentration of magnetic

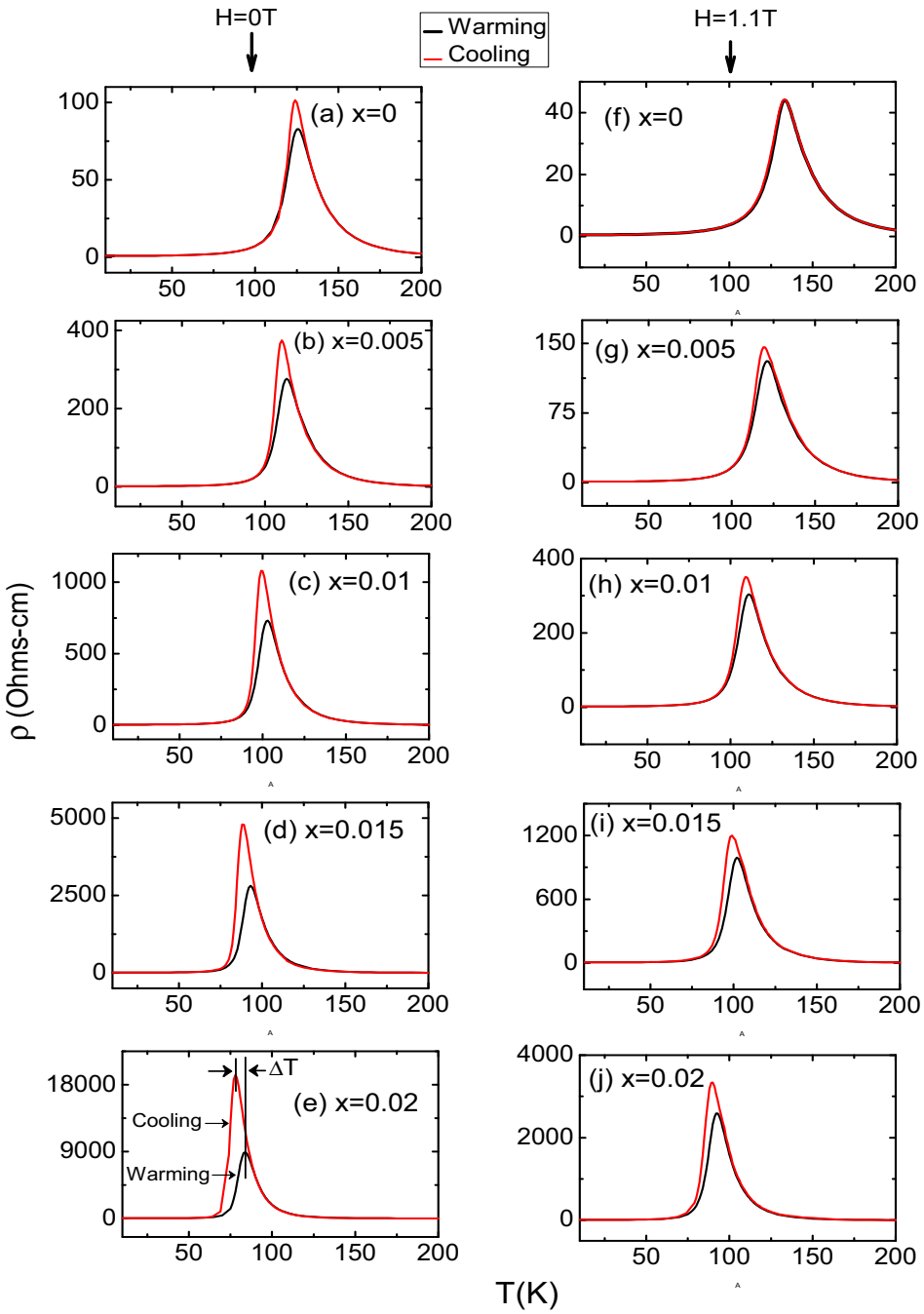


Figure 5.5: Thermal hysteresis in $\rho(T)$, observed during warming and cooling as described in the text, of the $Sm_{0.60}Sr_{0.40}Mn_{1-x}Fe_xO_3$ samples at low current ($10\mu$A). Fig. 5.5 (a-e) show the thermal hysteresis in H=0 T and Fig. 5.5 (f-j) show the thermal hysteresis in H= 1.1T. The $\Delta$T is the difference in $T_{MIT}$s measured during warming and cooling sequences.

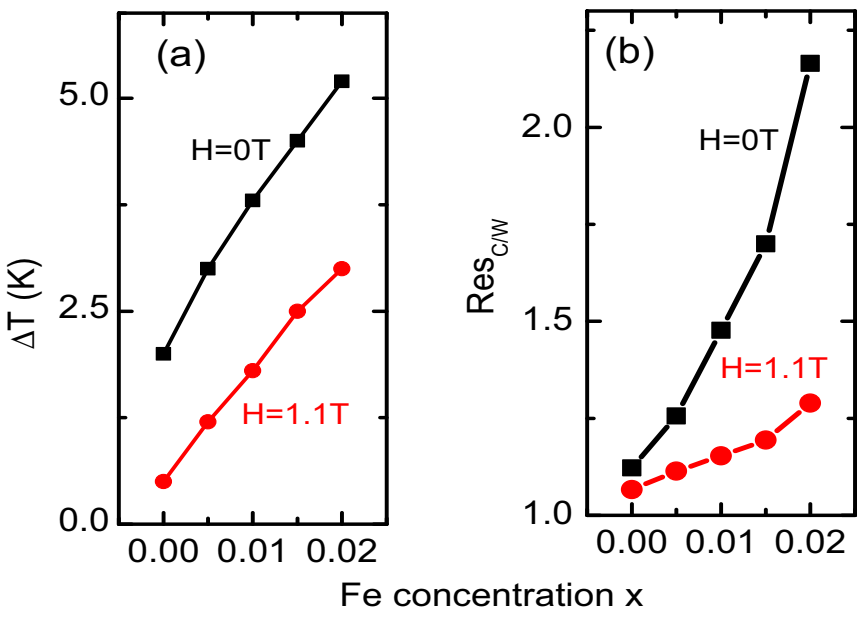


Figure 5.6: (a) The $\Delta$T vs Fe concentration and (b) the ratio of peak resistivities during cooling and warming ($Res_{c/w}$) vs Fe concentration in $Sm_{0.60}Sr_{0.40}Mn_{1-x}Fe_xO_3$ for H = 0 T and H = 1.1 T.

clusters (FMM and AFI) and the distribution of magnetic clusters of different shapes and sizes [18, 19]. Both $\Delta$T and $Res_{c/w}$ increase with an increasing Fe content (see Fig. 5.6(a) and Fig. 5.6(b)), indicating that the inhomogeneity is also being enhanced with an increasing $x$. Intuitively, this is not surprising given the known effect of Fe on the magnetic and transport properties in the manganites, as described earlier. Specifically, in $Sm_{0.60}Sr_{0.40}MnO_3$, recent measurements have found that at low temperatures, the sample has a phase-separated FMM ground state with A-type AF and small amounts of CE-type (charge ordered) AF clusters [20, 21, 22] (see chapter 1, Fig. 1.1 for a phase diagram of $Sm_{1-x}Sr_xMnO_3$). We suggest that Fe doping in SSMO suppresses the FMM phase and enhances the AFI phase. Because of identical ionic size of Mn and Fe ions, a few percent of Fe doping in SSMO will be randomly distributed in the system, and some new magnetic clusters will be formed. Fe-doping induced formation of different size-distributed magnetic clusters in

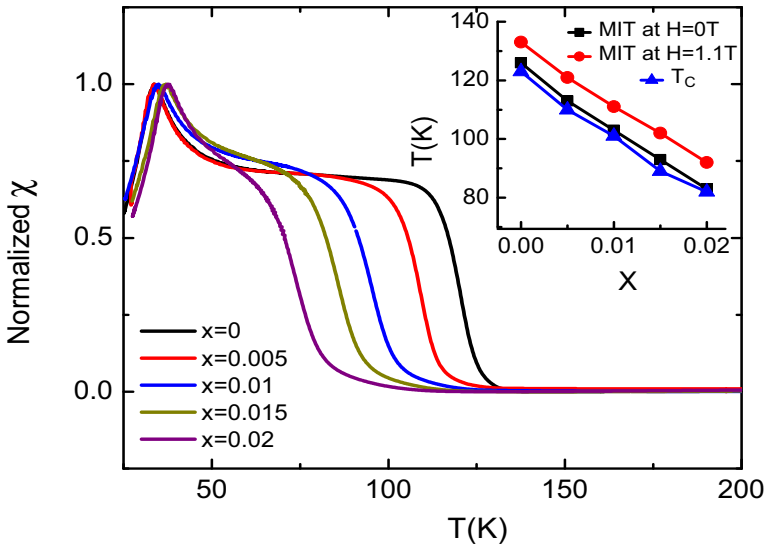


Figure 5.7: The temperature dependence of the normalized susceptibility $\chi$ for $Sm_{0.60}Sr_{0.40}Mn_{1-x}Fe_xO_3$. The inset shows the variation of $T_{MIT}$ for H=0T, $T_{MIT}$ for H=1.1T, as well as $T_c$ with Fe concentration $x$ (the data are obtained during warming).

SSMO enhances the disorder (spin disorder) in the magnetic structure of the system resulting in a more inhomogeneous system. Strong suppression of the FMM phase by Fe doping has been confirmed by the ac susceptibility measurements (see Fig. 5.7). $T_c$ decreases rapidly with an increasing Fe doping (see the inset of Fig. 5.7). The peaks observed at low temperatures in the susceptibility $\chi(T)$ for all the samples are believed to be related to the onset of AF ordering and/or spin reorientation of saturation magnetization [23]. Fig. 5.8 illustrates that the intrinsic ER, plotted for a current density of J = 0.060 A/cm$^2$, increases with an increasing $\Delta$T for both 0 T and 1.1 T.

We now discuss possible mechanisms for the observed dramatic increase of the ER with an increasing Fe doping in SSMO as illustrated in Fig. 5.4 and Fig. 5.8. It is known that percolation between randomly distributed FMM clusters plays an important role in determining the conduction properties of phase separated manganites [24]. It has been suggested that the application

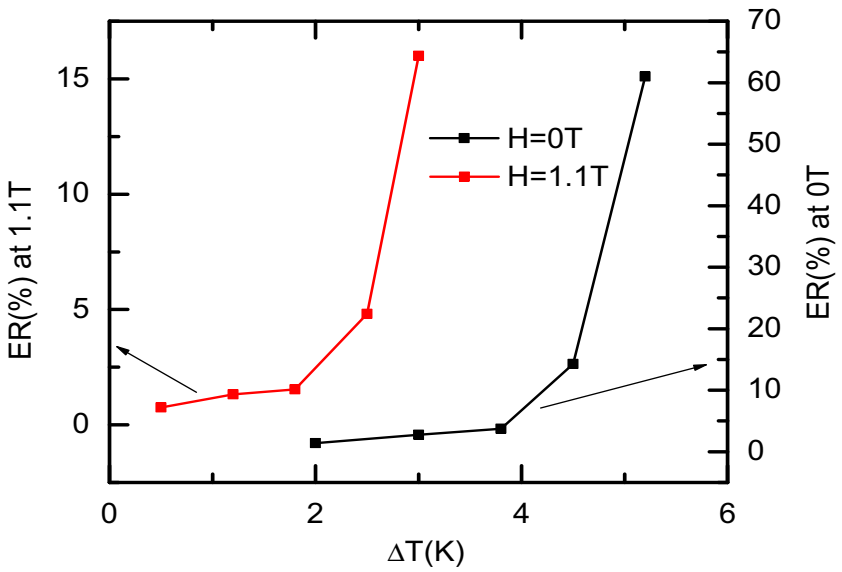


Figure 5.8: The intrinsic ER at a common current density of J=0.060 A/cm$^2$ vs $\Delta$T for $Sm_{0.60}Sr_{0.40}Mn_{1-x}Fe_xO_3$ for H = 0 T and H = 1.1 T.

of an electric field increases the relative volume fraction of metallic and insulting regions by accumulation of charge in metallic and insulating phases, thereby causing the interface between metallic and insulating regions to move [25]. We believe that similar behavior is occurring in our experiments: the electric field induced across the sample in our applied pulsed current experiments results in rearrangement of the interfaces. If the boundaries of the FMM clusters are closer together, links between them may be created and/or new filamentary conduction paths may be formed, which in turn decreases the resistivity [25]. In a more inhomogeneous sample, with higher Fe concentration, the electric field associated with pulsed current excitation creates a larger relative perturbation of the coexisting inhomogeneous magnetic states. The larger "tendency" to develop filamentary conduction paths results in an increase of the intrinsic ER with Fe doping. Note that one of the consequences of applying a magnetic field to the manganite is that it enhances the magnetic homogeneity of the samples through melting of the insulating state and

subsequent "increase" of the FMM state [26, 27]. Hence, the intrinsic ER is expected to be suppressed by a magnetic field. This behavior is observed in Fig. 5.4(c), 5.6 and 5.8 where for a particular Fe composition, the ER, $\Delta$T and $\mathrm{Res}_{c/w}$ all decrease when the applied magnetic field is increased.

## 5.4 Summary

In summary, we have investigated the intrinsic ER of $\mathrm{Sm}_{0.60}\mathrm{Sr}_{0.40}\mathrm{Mn}_{1-x}\mathrm{Fe}_x\mathrm{O}_3$ ($0 \leq x \leq 0.020$). This ER increases with increasing Fe content, while it decreases with an increasing magnetic field. Fe content induces AFI clusters in a FMM ground state, which in turn creates a more inhomogeneous magnetic system. On the other hand, magnetic field creates a more homogeneous magnetic system through melting of the AFI clusters in a FMM ground state. The results imply that the intrinsic electroresistance increases with the inhomogeneities of the samples.

# Bibliography


[1] S. T. Mahmud, M. M. Saber, H. S. Alagoz, K. Biggart, R. Bouveyron, Mahmud Khan, J. Jung, and K. H. Chow, Appl. Phys. Lett. **100**, 232406 (2012);

[2] S. T. Mahmud. M. M. Saber, H. S. Alagoz, R. Bouveyron, J. Jung, and K.H. Chow, Appl. Phys. Lett. **100**, 072404 (2012).

[3] C. Martin, A. Maignan, M. Hervieu, and B. Raveau, Phys. Rev. B **60**, 12191 (1999).

[4] Y. Tomioka, H. Hiraka, Y. Endoh, and Y. Tokura, Phys. Rev. B **74**, 104420 (2006).

[5] M. Egilmez, M. M. Saber, A. I. Mansour, R. Ma, K. H. Chow, and J. Jung, Appl. Phys. Lett. **93**, 182505 (2008).

[6] S. Hébert, A. Maignan, C. Martin, and B. Raveau, Solid State Commun. **121**, 229 (2002).

[7] V. S. Kumar, and R. Mahendiran, J. Appl. Phys. **109**, 023903 (2011).

[8] C. Hao, B. Zhao, G. Kuang, and Y. Sun , Phys. Status Solidi B **248**, 2921 (2011).

[9] J.-W. Cai, C. Wang, B.-G. Shen, J.-G. Zhao, and W.-S Zhan, Appl. Phys. Lett. **71**, 1727 (1997).

[10] Y. L. Chang, Q. Huang, and C. K. Ong, J. Appl. Phys. **91**, 789 (2002).

[11] J. M. Barandiarán, F. J. Bermejo, J. Gutiérrez, and L. F. Baquín, Journal of Non-crystalline Solids **353**, 757 (2007).

[12] O. Z. Yanchevskii, O. I. V'yunov, A. G. Belous, and A. I. Tovstolytkin, Low Temp. Phys. **32**, 134 (2006).

[13] S. M. Yusuf, M. Sahana, M. S. Hegde, K. Dörr, and K.-H. Müller , Phys. Rev. B **62**, 1118 (2000).

[14] S. D. Bhame, V. L. J. Joly, and P. A. Joy , Phys. Rev. B **72**, 054426 (2005).

[15] W. H. Shah, and S. K. Hasanain, J. Appl. Phys. **108**, 113907 (2010).

[16] L. K. Leung, A. H. Morrish, and B. J. Evans, Phys. Rev. B **13**, 4069 (1976).

[17] H. Sakai, K. Ito, T. Nishiyama, X. Yu, Y. Matsui, S. Miyasaka, and Y.Tokura, J. Phy. Soc. Jpn. **77**, 124712 (2008).

[18] D. Khomskii, and L. Khomskii, Phys. Rev. B **67**, 052406 (2003).

[19] L. Zhang, C. Israel, A. Biswas, R. L. Greene, and A. de Lozanne, Science **298**, 805 (2002).

[20] I. D. Luzyanin, V. A. Ryzhov, D. Yu. Chernyshov, A. I. Kurbakov, V. A. Trounov, A. V. Lazuta, V. P. Khavronin, I. I. Larionov, and S. M. Dunaevsky, Phys. Rev. B **64**, 094432 (2001).

[21] A. I. Kurbakov, A. V. Lazuta, V. A. Ryzhov, V. A. Trounov, I. I. Larionov, C. Martin, A. Maignan, and M. Hervieu, Phys. Rev. B **72**, 184432 (2005).

[22] A. I. Kurbakov, J. Magn. Magn. Mater. **322**, 967 (2010); A. I. Kurbakov, A.V. Lazuta, and V. A. Ryzhov, J. Phys.: Conf. Ser. **200**, 012099 (2010).

[23] V. Y. Ivanov, A. A. Mukhin, A. S. Prokhorov, and A. M. Balbashov, Phys. Status Solidi B **236**, 445 (2003).

[24] E. Dagotto, T. Hotta, and A. Moreo, Phys. Rep. **344**, 1 (2001).

[25] T. Wu, S. B. Ogale, J. E. Garrison, B. Nagaraj, A. Biswas, Z. Chen, R. L. Greene, R. Ramesh, T. Venkatesan, and A. J. Millis, Phys. Rev. Lett. **86**, 5998 (2001).

[26] M. Uehara, S. Mori, C. H. Chen, and S.-W. Cheong, Nature **399**, 560 (1999).

[27] A. I. Abramovich, L. I. Koroleva, A. V. Michurin, O. Y. Gorbenko, and A. R. Kaul, Physica B **293**, 38 (2000).

# Chapter 6

# Disorder controlled time dependent electrical transport in doped $Sm_{0.60}Sr_{0.40}MnO_3$ and $(Sm_{0.5}Gd_{0.5})_{0.55}Sr_{0.45}MnO_3$ manganites

## 6.1 Introduction

In electroresistive or colossal magnetoresistive manganites, relaxation (a relative change in electrical resistance with time) influences the physical properties of the materials and may limit their technological applications (e.g., in data storage devices, magnetic field sensors, spintronic devices) [1, 2, 3, 4, 5, 6, 7, 8, 9, 10, 11, 12, 13]. Up to now, the mechanism that controls the relaxation effect in manganites is unclear; therefore it is necessary to obtain a more detailed understanding of the relaxation effect to achieve reliable device operations.

As discussed in chapter 1, several authors [7, 8, 9, 10] have studied the

temperature dependent relaxation rate of resistivity in various manganites that show the metal to insulator transitions (MIT). Most of these studies have been focused on temperatures near the MIT of the samples, and reported large resistive relaxation (increase/decrease of resistivity with time) in this temperature range (see chapter 1, Fig. 1.4). Carneiro et al. [8] explained that close to MIT, the system's state can be changed easily between ferromagnetic (FM) and charge ordered (CO) antiferromagnetic (AF) due to the small energy barrier between these phases. ( Generally, the change in resistivity with time at a fixed temperature is caused by a spontaneous phase transformation between the coexisting various phases. Due to the competition of double exchange, superexchange and electron-lattice coupling, many kinds of phase transitions occur in the mixed-valence manganites [14]. In manganites, the coexisting FM and CO-AF phases have very similar free energies [15]. The free energy barriers between various phases of the system reach a minimum value near the phase transition temperatures [8, 16, 17]. In the mixed state, the total system contains a large number of subsystems with different free energies (i.e., the system has multiple free energy minima separated by finite energy barriers). The relaxation process followed by the clusters to reach their equilibrium size, can be thought of as a stepwise movement of the phase boundaries (interphase walls that separate the coexisting phases) through energy barriers [18, 19]. Phase boundaries usually tend to redistribute themselves towards a lower energy state to reach equilibrium).

Huang et al. [10] reported negative resistive relaxation ( decrease of resistivity with time) at low temperatures in the metallic state of the sample and a positive resistive relaxation (increase of resistivity with time) close to the MIT (see chapter 1, Fig. 1.5). They concluded that the mobilities of the phase boundaries at temperatures near the MIT change the phase fraction and are responsible for the relaxation in resistivity. At low temperatures (below 40 K, see chapter 1, Fig. 1.5), the phase boundaries become frozen due to low

thermal energies and the sample shows nearly zero relaxation of resistivity. However, the authors did not explain the origin of large negative resistive relaxations in the metallic state at low temperatures (near 40 K $\ll$ $T_{MIT}$, see chapter 1, Fig. 1.5 ), and experiments did not provide an explicit mechanism for controlling these relaxation effects in manganites.

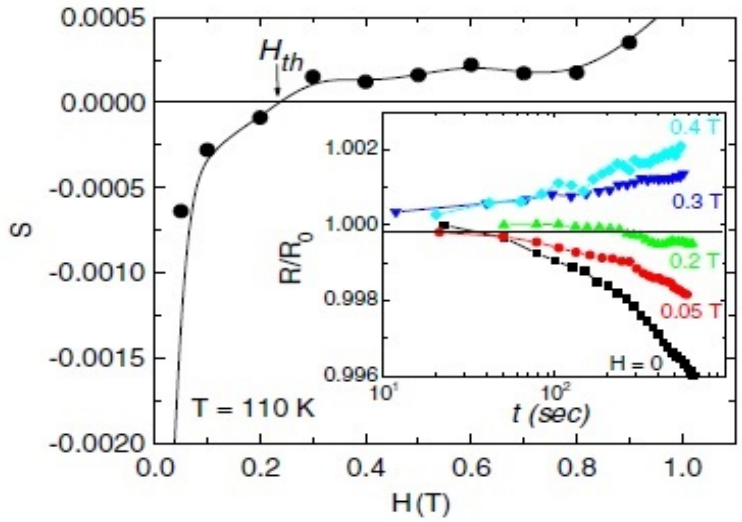


Figure 6.1: Resistive relaxation rate, S (defined as $S = (1/R_0)(dR/dlog(t))$, where $R_0$ is the initial resistance), measured at temperature 110 K, after the application and removal of different magnetic fields (H) to $La_{0.325}Pr_{0.3}Ca_{0.375}MnO_3$ polycrystalline sample. The inset shows the time evolution of the normalized resistance ($R/R_0$), after the application and removal of H. These data were used to calculate the values of S plotted in the main panel, and to extract the threshold field, $H_{th}$, the field at which the FM reaches equilibrium. Figure was reproduced from Ref. [9].

Recently, Quintero et al.[9] reported that an equilibrium state (no relaxation of resistivity) in a sample can be reached at a zero magnetic field after the application and subsequent removal of a threshold external magnetic field ($H_{th}$) (see Fig. 6.1). (The measurement procedure was as follows. $La_{0.325}Pr_{0.3}Ca_{0.375}MnO_3$ manganite was cooled from room temperature to a target temperature in zero magnetic field and time dependent resistance was measured. After that, they applied a magnetic field and subsequently removed it. This was followed by the measurement of relaxation at zero field. They

found that the initial negative relaxation rate of resistance observed in zero field gradually decreases and becomes positive with an increasing applied field H. They defined a threshold field $H_{th}$ upon removal of which the relaxation rate of the sample becomes zero (and an equilibrium state is reached)). The authors concluded that the negative relaxation rate of resistivity for H< $H_{th}$ indicates that a ferromagnetic (FM) fraction is lower than the equilibrium value and that the excess antiferromagnetic/charge order ( AF/CO) phase is transformed into the FM phase as time passes. An external magnetic field enhances the FM phase fraction at the cost of the non-FM phase and modifies the ratio of FM and non-FM regions into a phase separated (PS) system, leading an equilibrium state at H=$H_{th}$.

It is also known from earlier experimental measurements [20, 21, 22, 23, 25, 26, 27] that 'doping' can *permanently* modify the proportion of coexisting FM metallic and non-FM insulating phases in a manganite system. Moreover, 'doping' can be used to increase either FM metallic phases or non-FM insulating phases in a manganite system (whereas magnetic field can increase only the FM metallic phases). For example, a small amount of Fe doping (in Mn site) increases the amount of AF insulating phase fraction in a manganite system; a small amount of Ru doping (in Mn site) increases the amount of FM metallic phases and $BaTiO_3$ doping increases the amount of non-magnetic insulating phase fraction in a manganite system.

These results raise questions about the extent to which the relative amount of FM and non-FM phases and the relaxation of resistivity can be tuned, and about the origin of the relaxation effect and how to control it.

In order to further understand the effect of the relative amount of FM and non-FM phases on the relaxation of resistivity described above, we have attempted to modify the relative fraction of these phases in several manganites by 'doping' using for instance, $Sm_{0.60}Sr_{0.40}Mn_{1-x}Fe_xO_3$, (1-$y$)$Sm_{0.60}Sr_{0.40}MnO_3$ +$y$$BaTiO_3$ and $(Sm_{0.5}Gd_{0.5})_{0.55}Sr_{0.45}Mn_{1-z}Ru_zO_3$ compounds doped with Fe,

$BaTiO_3$ and Ru. The properties of these compositions are described in more detail below.

As discussed in previous chapters, $Sm_{0.60}Sr_{0.40}MnO_3$ (SSMO) shows some distinct electric and magnetic properties compared to other manganites. To the best of our knowledge, a time dependent electric property has not been studied before for this important manganite. Doping $Sm_{0.60}Sr_{0.40}MnO_3$ with Fe (on Mn site) increases the amount of an AF insulating phase in a manganite system. Note that SSMO has a phase separated ferromagnetic metallic (FMM) ground state with A-type AF and a small amount of CE-type (CO) AF insulating clusters [28]. Replacing some Mn ions with Fe in SSMO leads to an AF coupling between Fe and Mn ions and introduces magnetic disorder into the FMM ground state of this system [20, 21]. This results in an increase of the resistivity and a decrease of the sample's Curie temperature ($T_C$) and metal-to-insulator transition temperature ($T_{MIT}$) [20, 21].

Doping SSMO with $BaTiO_3$ (BTO), a non magnetic insulating material, increases the amount of an insulating phase and induces an extra disorder or strain into the system. This causes a shift of $T_{MIT}$ to low temperature but $T_C$ remains almost unchanged [22]. BTO mainly resides within grain boundaries, which increases scattering of charge carriers and consequently the resistivity [22].

Recent investigation of the effects of Ru doping (on Mn site) on the magneto-transport of $(Sm_{0.5}Gd_{0.5})_{0.55}Sr_{0.45}MnO_3$ (which is in the vicinity of the spin-glass-like insulator (SGI) and FMM border) revealed that small amounts of Ru doping improves the metallicity of the system, and moves the system away from the SGI state [23]. In fact, the substitution of Sm with Gd in $(Sm_{1-p}Gd_p)_{0.55}Sr_{0.45}MnO_3$ manganites dramatically reduces the ferromagnetic long range ordering (FMO). The quenched disorder caused by local lattice distortion modifies the FMO and induces spin frustration [29]. At Gd doping level $p \geq 0.6$, the FMO is converted to a SGI, where short-ranged charge

ordered/orbital ordered (CO/OO) correlations exist [29]. At slightly lower doping $p = 0.5$ the system's resistivity is expected to manifest a dependence on time due to the competition in its phase separated state near the boundary with the SGI phase. Therefore, it will be interesting to study the time dependent electrical transport of this Ru doped $(Sm_{0.5}Gd_{0.5})_{0.55}Sr_{0.45}MnO_3$ (SGSMO) system. (In particular, for investigating the effects of increasing FM interactions on the relaxation of resistivity SGSMO was chosen as the parent compound instead of SSMO because as we note in the section 6.3, SSMO possesses little relaxation of the resistivity and increasing the FM interactions within the sample further suppresses this metastability, making the measurements of this phenomenon challenging. On the other hand, SGSMO is considerably more "disordered" than SSMO, and SGSMO's resistivity is expected to manifest large relaxation rate.) It is well known from other experimental measurements (such as x-ray photoelectron spectroscopy (XPS)) that Ru ions in the Ru-doped manganites are mainly $Ru^{4+}$ with a small amount of $Ru^{5+}$ [24]. The presence of valence states $Ru^{4+}(4d^4{:}t_{2g}^4e_g^0)$ and $Ru^{5+}$ $(4d^3{:}t_{2g}^3e_g^0)$ in the Ru doped SGSMO manganite system leads to an increase in $Mn^{3+}(3d^4{:}t_{2g}^3e_g^1)$/ $Mn^{4+}(3d^3{:}t_{2g}^3e_g^0)$ ratio (increase $e_g$ electron density) and provides another ferromagnetic coupling pair $Mn^{3+}$- $Ru^{5+}$, in addition to $Mn^{3+}$- Mn $^{4+}$. This results in an increase of the FM metallic phase, $T_C$ and $T_{MIT}$ [23, 25, 26, 27].

## 6.2 Experimental Procedure

Polycrystalline samples of $Sm_{0.60}Sr_{0.40}Mn_{1-x}Fe_xO_3$ (with $x = 0$, 0.01, 0.015, 0.02, 0.025, 0.03), composite (1-$y$) $Sm_{0.60}Sr_{0.40}$ $MnO_3$ +$y$$BaTiO_3$ (with $y$= 0, 0.01, 0.015, 0.02) and $(Sm_{0.5}Gd_{0.5})_{0.55}Sr_{0.45}$ $Mn_{1-z}Ru_zO_3$ (with $z = 0$, 0.01, 0.05, 0.10) were prepared using the same solid state reaction method. This procedure was described in detail in Chapter 3. A Keithley 6221 ac/dc current source and Keithley 2182A nano-voltmeter were used to measure tem-

perature and time dependence of resistivity $\rho(T,t)$ at low applied currents ($\sim$1$\mu$A). The measurements of $\rho(T)$ were performed in a zero magnetic field over a temperature range between 10 K and 300 K. Time dependence of $\rho$ was measured at temperatures between 10 K and $\sim$160 K during warming cycles using the following procedure. The sample was first cooled from 300K to 10K and then warmed up to the temperature at which time dependence of $\rho$ was measured. The data were collected over a waiting period of 7,000 seconds. Before taking the $\rho(t)$ data at different temperatures, the sample's temperature was increased to 200K, above its $T_{MIT}$ value, followed by cooling to 10K and warmed up to the next temperature of the measurement in order to secure identical condition for all the measurements. Temperature dependence of the logarithmic relaxation rate of the resistivity $S(T,t)$ was calculated using the formula $S(T,t) = dlog(\rho(T,t)/\rho(T,1s))/dlog(t)$. The temperature dependence of ac magnetic susceptibility $\chi(T)$, was measured in a zero dc magnetic field for the warming cycle. $T_c$ was determined using the gradient method.

## 6.3 Results and discussion

$\rho(T)$ for all the Fe-doped SSMO, SSMO+BTO and Ru-doped SGSMO samples measured during the warming cycle are shown in Fig. 6.2 (a-c). All the samples show a metal to insulator transition (MIT) in zero magnetic field. The $T_{MIT}$ and $T_c$ of undoped SSMO ($\sim$ 120 K) and SGSMO ($\sim$ 65 K) are in excellent agreement with previous reports [29, 21, 30]. The $T_{MIT}$ and $T_c$ decrease significantly with an increasing Fe content in SSMO (down to $\sim$ 65 K for $x = 0.03$) . They increase significantly with an increasing Ru content in SGSMO (up to $\sim$ 98 K for $z = 0.10$) (see Fig. 6.2 (d) and (f)). Such behavior is consistent with previous studies of Fe doped and Ru doped manganites [20, 21, 23]. The $T_{MIT}$ for the composite SSMO+BTO samples decrease with an increasing BTO content ($y$), while the $T_c$ of the composite samples is almost

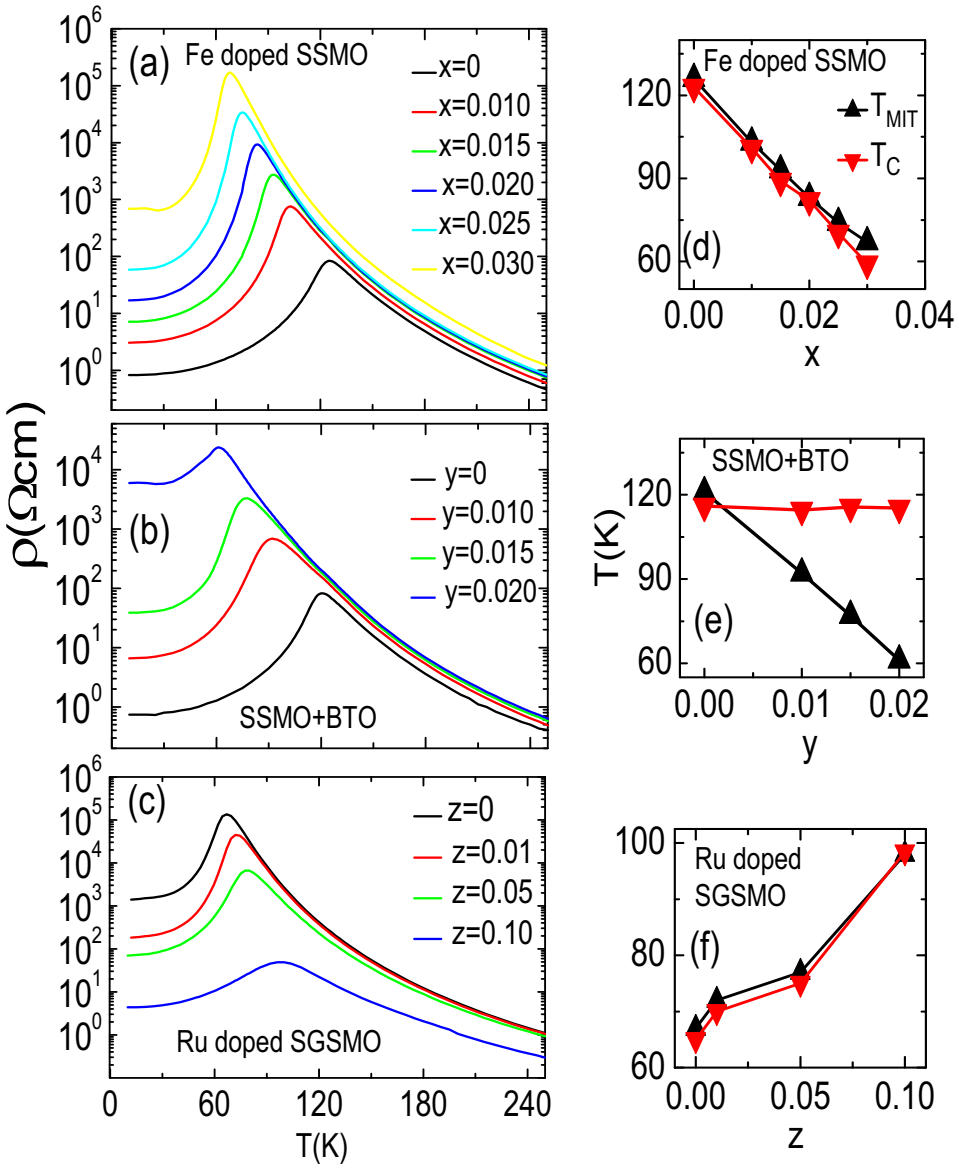


Figure 6.2: The temperature dependence of resistivity for : (a) Fe doped SSMO for different doping levels $x$, (b) composite SSMO+BTO for different SSMO/BTO ratios $y$, and (c) Ru doped SGSMO samples for different doping levels $z$. (d) Dependence of $T_{MIT}$ and $T_c$ on Fe doping level $x$; (e) $T_{MIT}$ and $T_c$ vs BTO doping $y$; (f) $T_{MIT}$ and $T_c$ vs Ru doping $z$. The lines are guides to the eye.

constant (see Fig. 6.2 (e)). Such behavior is also consistent with previous studies of BTO doped composites [22].

The time dependence of resistivity $\rho(t)$ was investigated for all samples.

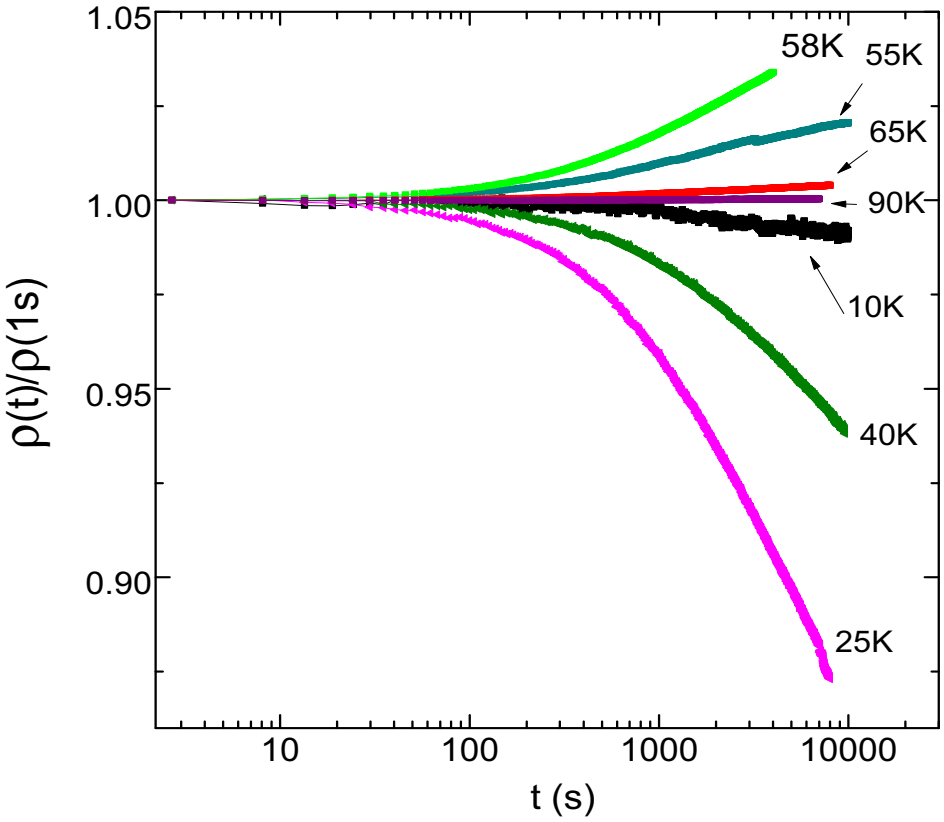


Figure 6.3: Examples of normalized resistivity $\rho(t)/\rho(1s)$ (where $\rho(1s)$ is the resistivity detected 1 second after the measurement has started) as a function of time (t) measured at several different temperatures and zero field in undoped SGSMO during warming cycle.

Fig. 6.3 shows an example of resistivity measured in an undoped SGSMO as a function of time at several different temperatures and zero magnetic field during the warming cycle. The resistivity decreases with time at temperatures between 10 K and 50 K, and increases with time at temperatures between 50 K and 90 K; however, the relaxation rates are small above 90K.

Temperature dependence of the relaxation rate of resistivity, $S$(T), for all the samples is presented in Fig. 6.4 (a-c). $S$ changes with temperature. The $S$(T) shows a maximum and a minimum for all the samples (see Fig. 6.4(a-c)): a minimum at temperature near the $T_A$ (an onset of AF ordering temperature,

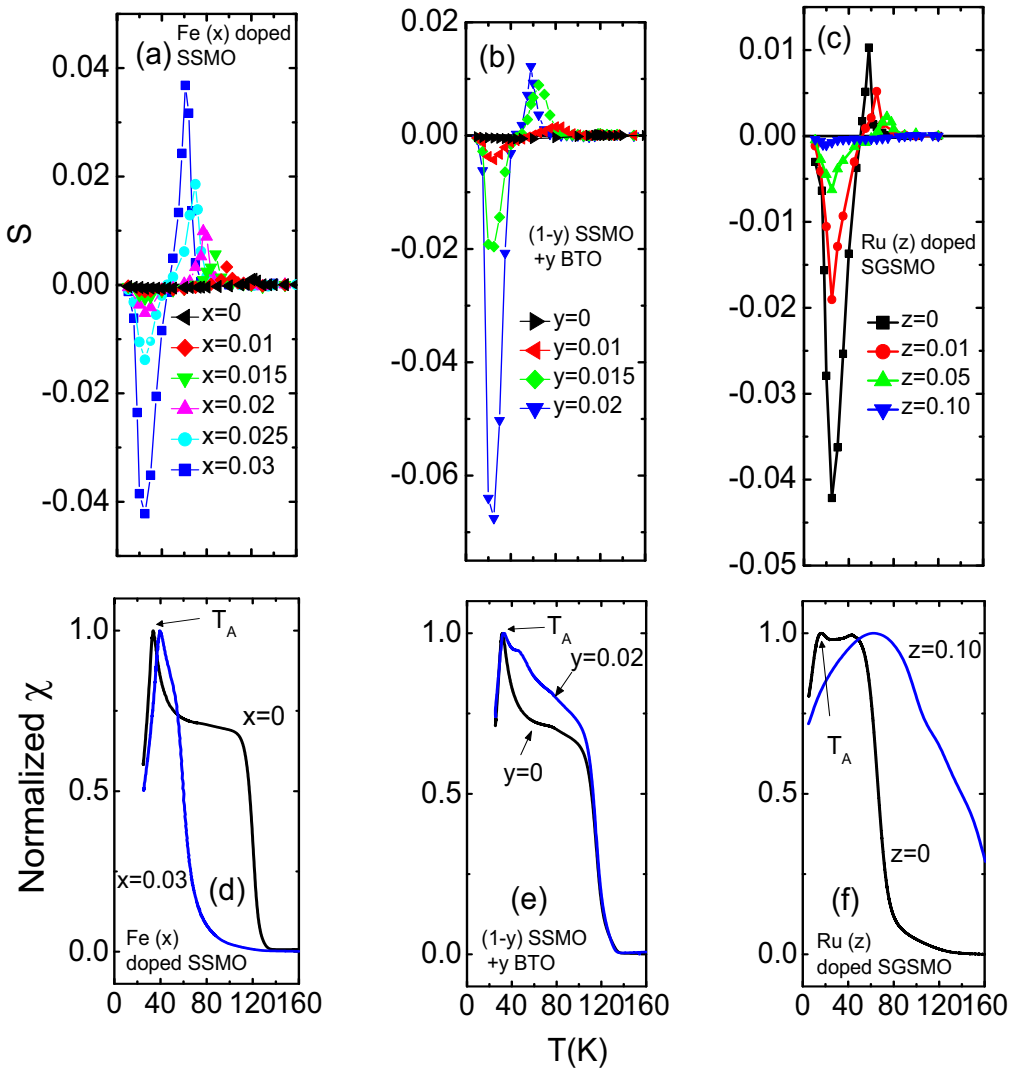


Figure 6.4: Temperature dependence of $S$ for all the samples: (a) Fe doped SSMO, (b) SSMO+BTO and (c) Ru doped SGSMO. The lines are guides to the eye. The temperature dependence of the normalized susceptibility $\chi$ for samples : (d) SSMO and Fe doped SSMO, (e) SSMO and composite SSMO+BTO, and (d) SGSMO and Ru doped SGSMO.

which is labeled in Fig. 6.4(d-f)) and a maximum at temperatures near $T_c$ or $T_{MIT}$. Similar behavior in $S(T)$ (positive and negative values) has been also reported by Huang et al. [10] in LCMO samples. Negative $S$ reflects the

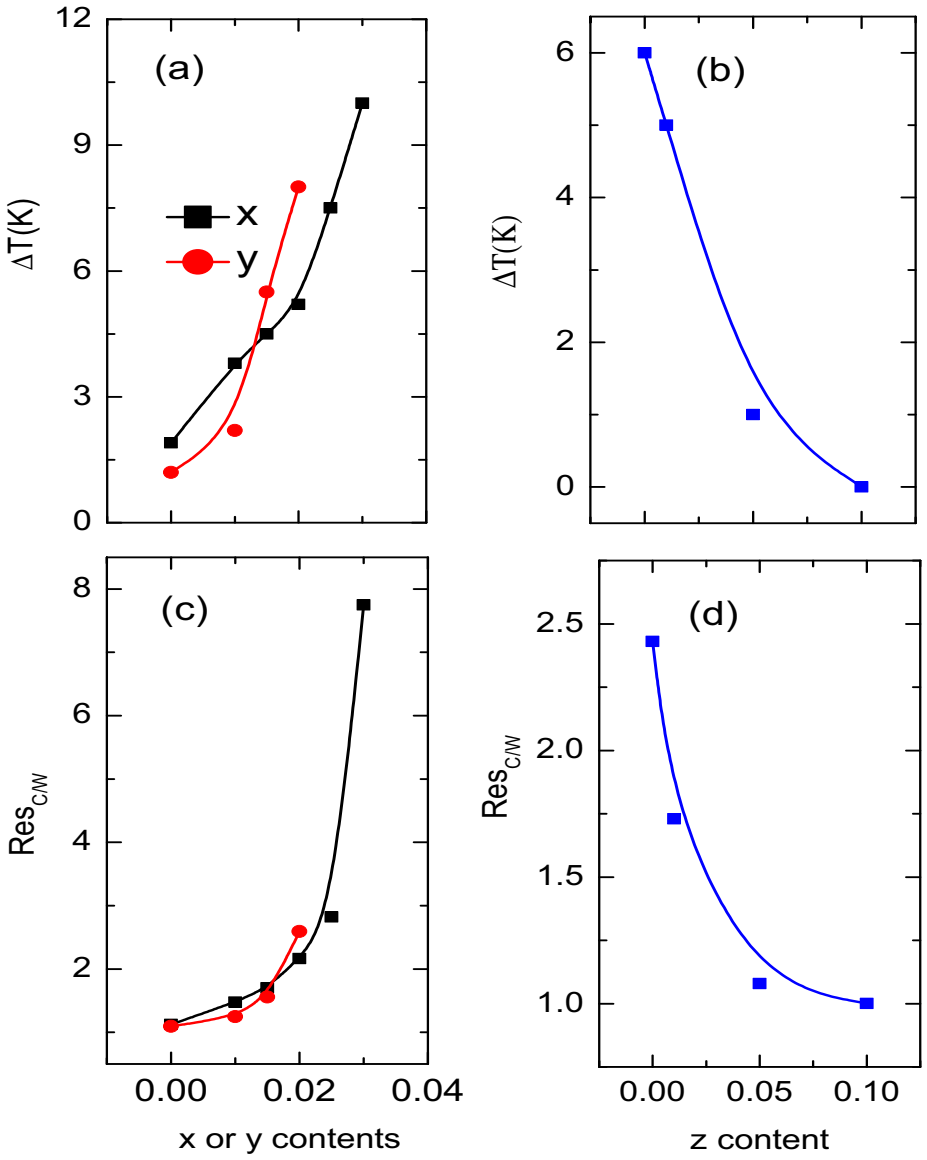


Figure 6.5: (a) $\Delta$T vs Fe concentration $x$ in $Sm_{0.60}Sr_{0.40}Mn_{1-x}Fe_xO_3$ and the $\Delta$T vs $y$ contents in the composite (1-$y$) $Sm_{0.60}Sr_{0.40}MnO_3$ +$y$$BaTiO_3$. (b) $\Delta$T vs Ru concentration $z$ in $(Sm_{0.5}Gd_{0.5})_{0.55}Sr_{0.45}$ $Mn_{1-z}Ru_zO_3$. The ratio of the peak resistivities during cooling and warming ($Res_{c/w}$) vs $x$ and $y$ is shown in Fig.(c). The ratio of the peak resistivities during cooling and warming ($Res_{c/w}$) vs $z$ is shown in Fig.(d). The lines are guides to the eye.

growth of the fraction of FMM phases as a function of time. On the other hand, positive $S$ indicates the increase of an insulating phase (for example, CO-AF) with time. The Fe doping ($x$) of SSMO and the BTO doping ($y$) in

SSMO+BTO revealed that $S$ increases gradually with an increasing doping levels ($x$ and $y$) in these systems (see Fig. 6.4(a-b)). On the other hand, $S$ decreases with increasing Ru concentration ($z$) in SGSMO; however at $z = 0.10$ the sample shows very little relaxation of resistivity (see Fig. 6.4(c)).

A sharp peak labeled $T_A$ in the normalized susceptibility $\chi(T)$ (see Fig. 6.4 (d-f)) is believed to be related to the onset of AF ordering and/or spin reorientation of saturation magnetization [31]. ( $T_A$ is not a spin glass transition because the frequency dependent $\chi$ measurements did not exhibit any shift of $T_A$ with frequency (not shown), which is consistent with the results reported by Naik et al.[32] in SSMO sample.) The decraese of $\chi(T)$ below $T_A$ could be due to ordering of $Sm^{3+}$ ($4f^5$) moments antiparallel to the Mn-sublattice, according to Ref.[32]. The $Sm^{3+}$ ($4f^5$) moments possibly order ferromagnetically within its sublattice but antiparallel to the Mn-sublattice below $T_A$ that is, there exist a weak AF coupling between Mn 3d and Sm 4f moments below $T_A$ [32]. This $T_A$ increases with an increasing Fe content in SSMO, it remains almost at the same temperature for BTO doping in SSMO+BTO, and it decreases with an increasing Ru substitution in SGSMO (see Fig. 6.4(d-f)).

There is a clear correlation between the relaxation of resistivity and the ratio of coexisting FM and non FM regions or the extent of phase separation in these samples. In particular, there is a hysteresis in the $\rho(T)$ for the SSMO sample after the warming and cooling cycles (see Fig. 5.5 in chapter 5). Thermal hysteresis width $\Delta T$ (see the text in Chapter 5 for details) and the ratio of the peak resistivity values measured after the cooling and warming cycles are measures of the extent of the inhomogeneous magnetic state or disorder in manganites [33, 34]. Both $\Delta T$ and the ratio of the peak resistivities increase with Fe doping in SSMO and BTO doping in SSMO+BTO (see Fig. 6.5(a) and (c)). On the other hand, they decrease with an increasing Ru content in SGSMO (see Fig. 6.5(b) and (d)), indicating the varying extent of the inhomogeneous magnetic state in these samples.

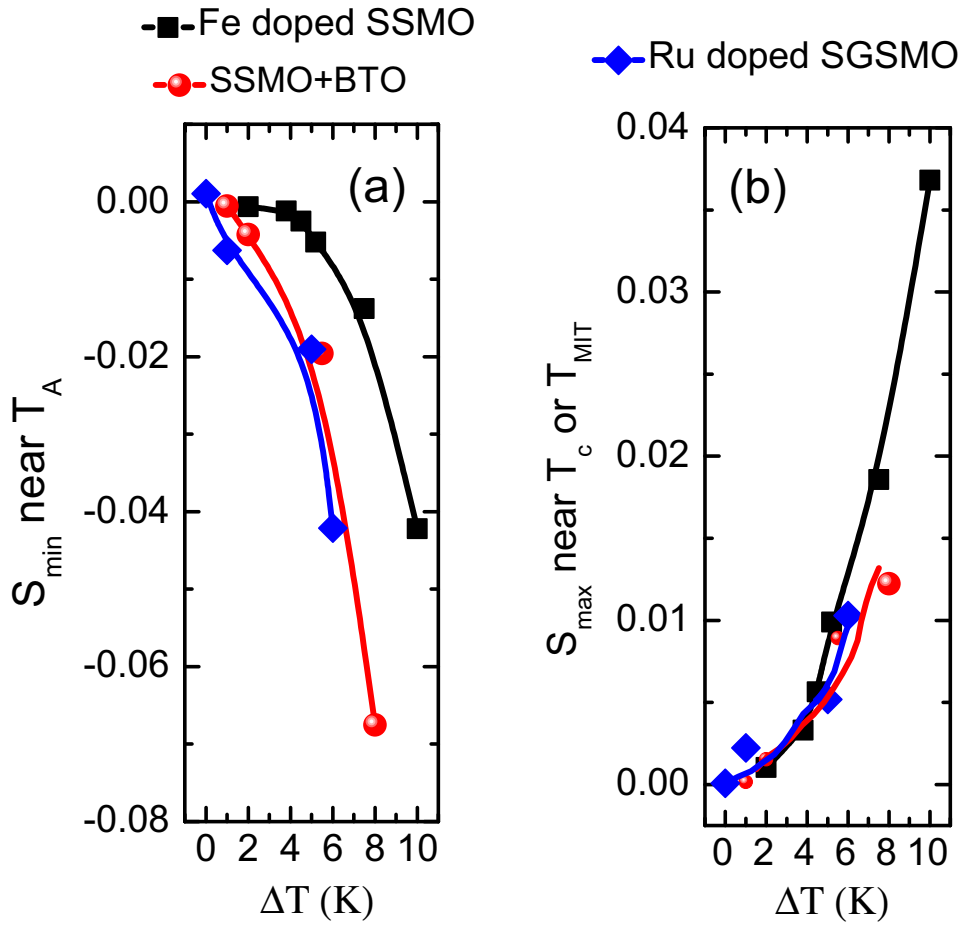


Figure 6.6: The minimum $S$ ($S_{min}$) near $T_A$ versus $\Delta$T, and (b) the maximum $S$ ($S_{max}$) near $T_C$ or $T_{MIT}$ versus $\Delta$T for all Fe doped SSMO, SSMO+BTO and Ru doped SGSMO samples. The lines are guides to the eye.

This result is consistent with the effects of Fe, BTO and Ru doping on the magnetic and transport properties of these manganites. SSMO has a FMM (a major phase fraction at low T) ground state with small amounts of AF insulating (AFI) phases/clusters [28]. A few percent of Fe in SSMO is randomly distributed, and the AF coupling between Fe and Mn ions [20, 21] introduce some new AF magnetic clusters or magnetic disorder. (Electrical conductivity in these PS samples can be understood by considering the percolation process via the FMM clusters (see section 2.6 in chapter 2). The sample's resistivity and the MIT temperature depend on the total concentration of magnetic

clusters (FMM and AFI) and the distribution of magnetic clusters of different shapes and sizes [33, 34].) Fe doping in SSMO suppresses the FMM phase and enhances the AF insulating phase, leading to a more inhomogeneous magnetic system. On the other hand, Ru doping in SGSMO (which is a more inhomogeneous PS manganite with coexisting FMM (a major phase fraction at low T) phase and CO/OO AFI clusters [29]) promotes the FMM states and destroys the short-ranged CO/OO AFI clusters, leading to a more homogeneous magnetic system. The presence of these features has been confirmed by the ac susceptibility measurements. $T_c$ decreases rapidly with an increasing content of Fe and increases due to Ru substitution (see Fig. 6.2 (d) and (f)). Moreover, the $T_A$ increases with an increasing Fe content and decreases with an increasing Ru substitution (see Fig. 6.4(d) and (f)). Although $T_c$ and $T_A$ (see Fig. 6.2(e)and 6.4(e)) are almost unchanged in SSMO+BTO, the non magnetic BTO resides within grain boundaries [22] and induces extra disorder in the system. Fig. 6.6(a) and (b) show clearly that the relaxation rates in all three series clearly correlated with the level of inhomogeneities within the system. Fig. 6.6(a) show the relaxation of resistivity at a temperature near $T_A$ (where the minimum relaxations take place) as a function of $\Delta$T, and Fig. 6.6(b) show the relaxation of resistivity at a temperature near $T_c$ or $T_{MIT}$ (where the maximum relaxations take place) as a function of $\Delta$T. The data (in Fig. 6.6(a,b)) show a exponential like increase of minimum S ($S_{min}$) and maximum S ($S_{max}$) with an increasing $\Delta$T for all the three manganite systems: Fe doped SSMO, BTO doped SSMO+BTO and Ru doped SGSMO.

We now discuss possible reasons for the observed change in the relaxation of resistivity caused by Fe doping in SSMO, BTO doping with SSMO and Ru doping in SGSMO (see Figs.6.4 (a-c), and 6.6(a,b)). Thermal energy favors the formation of various magnetic clusters of different length scales [33, 34, 35] in SSMO, SSMO+BTO and SGSMO system at various temperatures. The metastability of the coexisting magnetic clusters (for example, FMM and AFI

), phase competition and continuous variation of the coexisting phase fractions with time lead to the relaxation of resistivity in the phase-separated manganite system (see Figs. 6.4 (a-c)). At low temperatures (around $T_A$), the fraction of FMM domains is smaller than its corresponding equilibrium value, whereas FMM domains are larger than their corresponding equilibrium value near $T_{MIT}$. FMM phase dominates over the AFI phase in the low temperature region. Its volume increases with time, leading to a negative relaxation rate of resistivity. The volume of these regions can increase due to: the reorientation of magnetic moments/spins, motion of boundaries between coexisting phases, merging of two separated FMM domains, nucleation of new FMM domains or phase transformation from AFI to FMM (All these phenomena are correlated, and it is too hard to find a technique that can unequivocally support one or two of the above possibilities. Lorentz microscopy and electron holography [36] can be used to confirm the nucleation of new FMM domains, merging of two separated FM domains, motion of phase boundaries etc. at low temperatures). On the other hand, break-up of large FMM domains, the appearance of additional domain walls and the phase transformation from FMM to AFI phase lead to a positive relaxation rate of resistivity around the $T_{MIT}$. Note that the newly created domain walls act as scattering centers for the carriers and increase the resistivity. Moreover, FMM double exchange interaction (see chapter 2, section 2.3) weakens near the $T_{MIT}/T_c$ due to the high thermal energy. There is a possibility that the other coexisting insulting phases dominate over the FMM phase and start to grow at its expense. Our manganite samples also exhibit multiple magnetic ordering or transition (for example, samples show $T_A$ and $T_c$ ). Strong phase competition and easy phase transformation due to a small energy barrier between the coexisting phases in the vicinity of $T_A$ and $T_c/T_{MIT}$ [8] result in faster relaxation of resistivity, giving rise to the negative and positive peaks in $S(T)$ around the $T_A$ and $T_c/T_{MIT}$, respectively.

Figs. 6.2(a-f), 6.4(d-f) and 6.5(a-d) demonstrate that Fe and BTO doping increase the non FMM phases and intrinsic inhomogeneities in the SSMO manganite systems, whereas Ru doping increase the FMM regions and decrease the inhomogenieties/disorder in the SGSMO manganite system. Note that the coexistence and competition of multiple phases/clusters give rise to spin frustration into the system, producing a metastable state[4, 37]. In Fe and BTO doped samples not only does the insulating phase increase in volume but there is also an increase of the amount cluster [33, 34] and (magnetically disordered) interfaces between metallic and insulating clusters (Note that Fe and BTO doped samples show high resistivity and low MIT temperatures; percolation via the FMM clusters is considered to be a mechanism for MIT or electrical conduction in these phase-separated samples (see chapter 2, section 2.6)). In more inhomogeneous magnetic systems, i.e., for higher Fe and BTO concentration, the inter-cluster spin frustration, spin reorientation and phase transformation could be more pronounced than for lower Fe and BTO dopings, resulting in faster relaxation of resistivity. The opposite trend has been observed in Ru doped SGSMO samples, where the decrease of the intrinsic inhomogeneity or inter-cluster spin frustration results in a dramatic decrease in the spin reorientation and phase transformation. Consequently, the time decay of the resistivity decreases in the Ru doped SGSMO samples. For a Ru doping level $z$ of 0.1, disorder/inhomogeneity is negligible ($\Delta$T $\approx$ 0) and the resistivity is almost time independent (see Figs 6.4(c) and 6.6(a,b)). The data in Fig. 6.6 (a,b) show evidence for the correlation between the intrinsic inhomogeneity/disorder (defined by $\Delta$T) and the relaxation effects in manganite samples, and imply that the two peaks in $S$(T) (negative and positive) or the relaxation effect can be tuned by $\Delta$T through the control of the size and concentration of FMM and non FMM phase fractions. The relaxation of resistivity increases with increasing the amount of non FMM regions (for example, AF insulating, PM insulting etc.) into the PS manganite system,

but it decreases with an increasing amount of FMM phases.

Finally, we return to the results of Quintero et al.[9] who studied the relaxation of resistivity (in phase separated manganite) tuned by a magnetic field. They reported that the magnetic field can be used to quickly increase the amount of FMM phases, to control the 'negative' relaxation of resistivity and to drive the system to its equilibrium state. They determined a threshold magnetic field ($H_{th}$) (see Fig. 6.1) at which one can obtain the equilibrium FMM fraction. At high magnetic field ($H > H_{th}$), the amount of the FMM phase exceeds the equilibrium volume. Removal of applied H causes a decrease of the FMM fraction and consequently a 'positive' relaxation of the resistivity (see Fig. 6.1). This positive relaxation (an increase of resistivity with time) can be attributed to the break-up of ferromagnetic domains and the appearance of additional domain walls, according to Ref.[13]. Creation of highly resistive domain walls increases the scattering of electrons and the resistivity of the sample.

In contrast, we found that both the 'negative' (near the $T_A$, see Fig. 6.4 (a-c)) and 'positive' (near the $T_c/T_{MIT}$, see Fig. 6.4(a-c)) relaxation of resistivity can be controlled by doping, either increasing the amount of FMM phases or increasing the amount of non-FMM phases into the system. Both the 'negative' and 'positive' relaxation of resistivity decrease with an increasing amount of the FMM phases, whereas they increase with an increasing amount of the non-FMM phases.

The decrease/increase of the 'negative' relaxation of resistivity with an increasing amount of the FMM/non-FMM phases is consistent with the results reported by Quintero et al.[9] (where the growth of the FMM phase decreases the negative relaxation and drives the system to equilibrium). It is, therefore, expected that the growth of the non-FMM phase causes an unbalance of the relative phase fractions, leading to a large negative relaxation of resistivity. However, the mechanism of controlling the 'positive' relaxation of resistivity

has not been provided by these authors.

We found a correlation between the intrinsic inhomogeneity/disorder (defined by $\Delta$T as described earlier) and the negative and positive relaxation of resistivity for the manganite samples (see Fig. 6.6 (a,b)). Both the negative and positive relaxation rates are large in more inhomogeneous/disorder systems (see Fig. 6.6 (a,b)). The interplay between the intrinsic disorder and strong electronic and magnetic correlations in the mixed-valent manganites may frustrate the nucleation, giving rise to the observed doping dependence of the resistive relaxation. Our experimental data suggest that these ('negative' and 'positive') resistive relaxations can be controlled by the relative amount of FMM and non-FMM phases.

## 6.4 Summary

We have investigated the effect of the relative amount of FMM and non-FMM regions on the relaxation rates of resistivity ($S$) in Fe and BTO doped SSMO, and in Ru doped SGSMO. Fe and BTO doping increases the amount of non-FMM phases and modifies the relative amount of FMM and non-FMM phases in SSMO, whereas Ru doping increases the amount of FMM phases and modifies the ratio of FMM and non-FMM phases in SGSMO. A large negative relaxation rate of resistivity is found at low temperatures near the $T_A$ (an onset of AF ordering temperature). On the other hand, a large positive relaxation rate of resistivity is found near the $T_c$ or $T_{MIT}$ for all three manganite systems. Both the negative and positive relaxation of resistivity ($S_{min}$ near $T_A$ and $S_{max}$ near $T_c$/$T_{MIT}$) depend strongly on the thermal hysteresis width $\Delta$T (defined as an extent of the inhomogeneous magnetic state or disorder in a manganite system), which can be controlled either by an increasing amount of FMM phases or by an increasing amount of non-FMM phases. Doping SSMO with Fe and BTO causes a more inhomogeneous magnetic system as evidenced by

an increase of the $\Delta$T with an increasing Fe and BTO content in SSMO. On the other hand, doping SGSMO with Ru makes a more homogeneous magnetic system as evidenced by a decrease of the $\Delta$T with an increasing Ru content in SGSMO. Relaxation rates $S$ are large when the SSMO is doped with Fe and BTO; however, they are suppressed by Ru substitution in SGSMO. The data obtained on these three systems revealed a gradual exponential-like increase of the $S_{min}$ and $S_{max}$ with an increasing $\Delta$T. They imply that the relaxation of resistivity in manganites depends on $\Delta$T i.e., it can be tuned by modifying the relative amount of the FMM and non-FMM phases.

# Bibliography


[1] J. Tao, D. Niebieskikwiat, M. B. Salamon, and J. M. Zuo, Phys. Rev. Lett. **94**, 147206 (2005); D. Niebieskikwiat, J. Tao, J. M. Zuo, and M. B. Salamon, Phys. Rev. B **78**, 014434 (2008).

[2] J.-Z. Wang, J.-R. Sun, Q.-Y. Dong, G.-J. Liu, B.-G. Shen, Solid State Commun. **149**, 325 (2009).

[3] M. Egilmez, M. M. Saber, M. Abdelhadi, K. H. Chow, and J. Jung, Phys. Lett. A **375**, 4049 (2011)

[4] P. Levy, F. Parisi, L. Granja, E. Indelicato, and G. Polla, Phys. Rev. Lett. **89**, 137001 (2002).

[5] R. S. Freitas, L. Ghivelder,F. Damay, F. Dias, and L. F. Cohen, Phys. Rev. B **64**, 144404 (2001).

[6] I. G. Deac, S. V. Diaz, B. G. Kim, S.-W. Cheong, and P. Schiffer, Phys. Rev. B **65**, 174426 (2002); N. Kozlova, K. Dörr, D. Eckert, A. Handstein, Y. Skourski, T. Walter, K.-H. Müller, and L. Schultz , J. Appl. Phys. **93**, 8325 (2003).

[7] X. J. Chen, H.-U. Habermeier, and C. C. Almasan, Phys. Rev. B **68**, 132407 (2003).

[8] A. S. Carneiro, F. C. Fonseca, T. Kimura, and R. F. Jardim, J. Phys.: Condens. Matter **20**, 215203 (2008).

[9] M. Quintero, F. Parisi, G. Leyva, and L. Ghivelder, J. Phys.: Condens. Matter **20**, 345204 (2008).

[10] Z. Huang, G. Gao, F. Zhang, X. Feng, L. Hu, X. Zhao, Y. Sun, W. Wua, J. Magn. Magn. Mater. **322** 3544 (2010).

[11] K. A. Shaykhutdinov, D. A. Balaev, S. V. Semenov, S. I. Popkov, A. A. Dubrovskiy, N. V. Sapronova and N. V. Volkov, J. Phys. D: Appl. Phys. **44**, 255001 (2011).

[12] M. Sirena, L. B. Steren, and J. Guimpel, Phys. Rev. B **64**, 104409 (2001).

[13] S. R. Bakaul, B. F. Miao, W. Lin, W. Hu, A. David, H. F. Ding, and T. Wu, Appl. Phys. Lett. **101**, 012408 (2012).

[14] J. B. Goodenough, J. Appl. Phys. **81**, 5330 (1997).

[15] L. Ghivelder, R. S. Freitas, M. G. das Virgens, M. A. Continentino, H. Martinho, L. Granja, M. Quintero, G. Leyva, P. Levy, and F. Parisi, Phys. Rev. B **69**, 214414 (2004).

[16] M. Uehara, and S.-W. Cheong, Europhys. Lett. **52**, 674 (2000).

[17] G. Singh-Bhalla, A. Biswas, and A. F. Hebard, Phys. Rev. B **80**, 144410 (2009).

[18] G. Y. Wang, X. H. Chen, T. Wu, X. G. Luo, W. T. Zhang, and G. Wu, Phys. Rev. Lett. **100**, 146402 (2008).

[19] L. Ghivelder, and F. Parisi, Phys. Rev. B **71**, 184425 (2005).

[20] S. T. Mahmud, M. M. Saber, H. S. Alagoz, K. Biggart, R. Bouveyron, Mahmud Khan, J. Jung, and K. H. Chow, Appl. Phys. Lett. **100**, 232406 (2012); S. T. Mahmud. M. M. Saber, H. S. Alagoz, R. Bouveyron, J. Jung, and K.H. Chow, Appl. Phys. Lett. **100**, 072404 (2012).

[21] H. Sakai, K. Ito, T. Nishiyama, X. Yu, Y. Matsui, S. Miyasaka, and Y.Tokura, J. Phy. Soc. Jpn. **77**, 124712 (2008).

[22] P.T. Phong, D.H.Manh, N.V.Dang, L.V.Hong, and I.J.Lee, Physica B **407**, 3774 (2012).

[23] H. S. Alagoz, I. Živković, S. T. Mahmud, M. M. Saber, G. Perrin, J. Shandro, M. Khan, Y. Zhang, M. Egilmez, J. Jung, and K. H. Chow, Phys. Status Solidi B, **250**, s2158 (2013).

[24] Y. Ying, J. Fan, L. Pi, Z. Qu, W. Wang, B. Hong, S. Tan, and Y. Zhang, Phys. Rev. B **74**, 144433 (2006).

[25] S. Hébert, A. Maignan, C. Martin, and B. Raveau, Solid State Commun. **121**, 229 (2002).

[26] C. L. Lu, X. Chen, S. Dong, K. F. Wang, H. L. Cai, D. Li, Z. D. Zhang and J.-M. Liu, Phys. Rev. B **79**, 245105 (2009).

[27] M. M. Saber, M. Egilmez, A. I. Mansour, I. Fan, K. H. Chow, and J. Jung, Phys. Rev. B **82**, 172401 (2010).

[28] A. I. Kurbakov, J. Magn. Magn. Mater. **322** 967 (2010); S. T. Mahmud, M. M. Saber, H. S. Alagoz, J. Jung, and K. H. Chow, J. Phys. Chem. Solids **74**, 1865 (2013).

[29] Y. Tomioka, Y. Okimoto, J. H. Jung, R. Kumai, and Y. Tokura, Phys. Rev. B **68**, 094417 (2003); M. Egilmez, I. Isaac, D. D. Lawrie, K. H. Chow, and J. Jung, J. Mater. Chem. **18**, 5796 (2008).

[30] A. Rebello, and R. Mahendiran, Appl. Phys. Lett. **93**, 232501 (2008).

[31] V. Y. Ivanov, A. A. Mukhin, A. S. Prokhorov, and A. M. Balbashov, Phys. Status Solidi B **236**, 445 (2003).

[32] V. B. Naik, and R. Mahendiran, J. Appl. Phys. **110**, 053915 (2011).

[33] D. Khomskii, and L. Khomskii, Phys. Rev. B **67**, 052406 (2003).

[34] L. Zhang, C. Israel, A. Biswas, R. L. Greene, and A. de Lozanne, Science **298**, 805 (2002).

[35] M. H. Burkhardt, M. A. Hossain, S. Sarkar, Y.-D. Chuang, A. G. C. Gonzalez, A. Doran, A. Scholl, A. T. Young, N. Tahir, Y. J. Choi, S.-W. Cheong, H. A. Dürr, and J. Stöhr, Phys. Rev. Lett. **108**, 237202 (2012).

[36] Y. Murakami, H. Kasai, J. J. Kim, S. Mamishin, D. Shindo, S. Mori, and A. Tonomura, Nature Nanotechnology **5**, 37 (2010).

[37] F. Rivadulla, M. A. López-Quintela, and J. Rivas, Phys. Rev. Lett. **93**, 167206 (2004).

# Chapter 7

# Magnetocapacitance effect in the epitaxial $BaTiO_3/La_{0.66}Ca_{0.34}MnO_3$ heterostructure

## 7.1 Introduction

As discussed in chapter 1, materials that exhibit both ferroelectric and magnetic, i.e., multiferroic, properties are rare [1, 2, 3]. Besides the scientific interest in their physical properties, multiferroics are potential candidates for new applications/devices, including sensors, data storage, memory elements, and transducers [1, 2, 3, 4, 5]. Examples are: ferroelectric memories with a nondestructive magnetic reading, magnetic random access memories (MRAM) with an electrical writing procedure (MERAM), and multiple state memory elements where data are stored both in magnetic and electric polarizations [6, 7].

The single-phase multiferroics exhibit weak coupling between magnetic and electric orders [3, 7]. However, the coupling between magnetic and electric or-

ders may be significantly enhanced in the composites of ferromagnetic and ferroelectric phases [5]. Recently, epitaxial ferroelectric/manganite heterostructures have received lots of interest because charge, spin, and orbital order at the interfaces are responsible for many unusual multiferroic properties [7, 8].

Singh et al.[9] investigated the magnetoelectrical properties of $BaTiO_3/La_{0.70}Ca_{0.30}MnO_3$ perovskite-superlattice grown on $SrTiO_3$ substrates, where the deposited $La_{0.70}Ca_{0.30}MnO_3$ film of $\sim$2 nm in thickness is a ferromagnetic (FM) insulator. They observed negative magnetocapacitance (MC) effects (a decrease of capacitance or dielectric constant in a magnetic field) (see Chapter 1, Fig. 1.7), as well as negative magnetoresistance (MR) upon application of a magnetic field. They found a 3% MC effect per Tesla at 1 kHz and 100 K, whereas MC effects in some ceramics of single phase multiferroics (hexagonal rare earth manganites) were of the order of 1% per Tesla near the magnetic (antiferromagnetic) transition temperature ($\sim$ 40 K)[9]. They also observed MC effect only at low frequency (see Chapter 1, Fig. 1.7) and suggested to use the model proposed in Ref.[10], where the BTO layer is replaced by a resistance and capacitance in parallel, and the LCMO as a single resistance, and they are connected in series, to understand this low frequency MC effect. They concluded that the coupling between magnetic and dielectric orders give rise to this negative MC effect in the superlattice-based oxide multiferroic.

Later, Catalan et al.[11] proposed a Maxwell-Wagner (M-W) series capacitor model to explain the MC effect of superlattices consisting of $BaTiO_3$ and a magnetoresistive manganite (see Chapter 1, Section 1.1.3 for details). Based on the M-W theoretical model (two leaky capacitors in series, with one of the leakage components being magnetically tunable (see Chapter 1, Fig. 1.8 for details)), they calculated the dielectric constant for a superlattice combining $BaTiO_3$ and a ferromagnetic manganite and found that a large MC effect can be achieved through a combination of magnetoresistance and the M-W effect that is, strong MC effect can also be achieved without true magnetoelectric

coupling. In contrast to the mechanism of MC proposed by Singh et al. [9], Catalan et al.[11] found that a negative magnetoresistive manganite layer can produce a positive MC effect (see Chapter 1, Fig. 1.8 (b)). This is opposite in sign to the MC effect reported by Singh et al. [9]. These contradictory results raise questions about the origin of MC.

In order to understand the mechanism/origin of the MC effect and fabricate a multiferroic sample that exhibits a large MC at low magnetic field , we synthesized an epitaxial $BaTiO_3/La_{0.66}Ca_{0.34}MnO_3$ heterostructure on a $SrTiO_3$ (STO) substrate, and investigated its magnetoelectical properties. (We chose the $La_{0.66}Ca_{0.34}MnO_3$ composition because the highest Curie temperature ($T_c$) can be achieved in $LaMnO_3$-Ca for doping $x \approx 1/3$ [13]). Since atomically smooth interfaces can be obtained in heterostructures with ultrathin manganite layers, we deposited a very thin layer (16 nm) of $La_{0.66}Ca_{0.34}MnO_3$ (LCMO) on STO. It shows a metal to insulator transition (MIT) and a significant magnetoresistance at low magnetic fields. Note that a very thin LCMO film grown on STO is subjected to tensile strain, which favors the occupation of a $d_{x^2-y^2}$ $e_g$ orbitals and an orbitally ordered (OO) antiferromagnetic insulating state [14, 15], and induces phase separation (phase coexistence between ferromagnetic metal and antiferromagnetic insulator) [16, 17]. Since a magnetic field changes the MIT and phase separation in a manganite, it should also influence the properties of the interface between an LCMO manganite film and a $BaTiO_3$ (BTO) ferroelectric film.

## 7.2 Experimental Procedure

$La_{0.66}Ca_{0.34}MnO_3$ (LCMO) and $BaTiO_3$ (BTO) films were prepared by DC and RF sputter deposition. Polycrystalline sputtering targets ( $1''$ and $2''$ in diameter) of LCMO and BTO were prepared by the solid state reaction technique. A prescribed ratio of $La_2O_3$, $CaCO_3$ and $MnO_2$ powders were

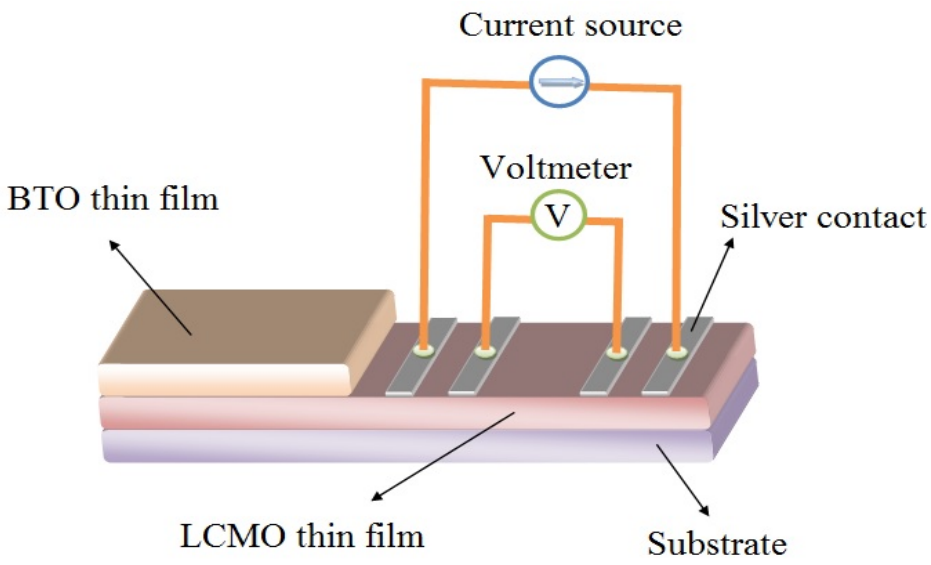


Figure 7.1: Sketch of the resistance measurement configuration for an LCMO layer of a BTO/LCMO heterostructure grown on the STO substrate.

mixed thoroughly to prepare LCMO, and a prescribed ratio of $BaCO_3$ and $TiO_2$ powders were mixed thoroughly to prepare BTO bulk samples. A detailed description of the syntheses of manganite and ferroelectric BTO samples is given in Chapter 3. In order to synthesize heterostructures composed of manganites and ferroelectrics, epitaxial LCMO (manganite) films were first deposited on (001) oriented STO substrates at 750 °C by an off-axis DC magnetron sputtering at 50 W in an oxygen-argon mixture. The working pressure of the $O_2$-Ar gas mixture was 120 mTorr with the ratio of $O_2$ and Ar partial pressures of 5:1. After the deposition, the samples were cooled down to 650 °C with a rate of 10°C per minute and subsequently annealed for 3 hours at this temperature after the chamber was filled with pure oxygen at atmospheric pressure. This was followed by cooling the samples down to room temperature at a rate of 20°C/min. Then, ferroelectric BTO layer was deposited on LCMO layers at 750 °C by an off-axis RF magnetron sputtering at 100 W in an oxygen-argon mixture, with $O_2$ and Ar pressures of 100 mTorr and 20 mTorr, respectively. Shadow masks were used to pattern the multilayers. The

film thickness was determined from the deposition time. Structural characterizations of the samples were performed at room temperature using a Rigaku X-ray diffractometer with Cu -$K_\alpha$ radiation. The out-of-plane (c-axis) lattice parameters of the films were determined from the x-ray diffraction (XRD) results and the out-of-plane lattice strains were estimated using the formula $\epsilon = (c_{film} - c_{bulk})/c_{bulk} \times 100\%$, where $c_{bulk}$ and $c_{film}$ are the c axis lattice parameters for the bulk sample and the thin film, respectively. The resistance of the 16 nm thick manganite LCMO layer as a function of temperature (77 K$-$297 K) was measured using a four probe method (see Fig. 7.1 for resistance measurement configuration). The silver contacts were sputtered onto the samples using an RF magnetron source. The Ag electrodes with an area of $\sim 1mm^2$ were also sputtered onto the BTO film. The Ag electrodes served as the top electrodes and the LCMO layer served as the bottom electrode for the ferroelectric and capacitance measurements (see Chapter 3, Fig. 3.8). Capacitance and dielectric loss of the samples were measured using the Agilent 4284A precision LCR meter. The electric field dependent polarization loops, P(E) of the samples were measured using a home built Sawyer-Tower circuit. The average remnant polarization ($P_r$) and the coercive field ($E_c$) were calculated using the formulas $P_r = (|P_{r+}| + |P_{r-}|)/2$ and $E_c = (|E_{c+}| + |E_{c-}|)/2$ , where $P_{r+}$ and $P_{r-}$ are positive and negative remnant polarizations, and $E_{c+}$ and $E_{c-}$ are positive and negative coercive fields, respectively. MC and MR were calculated using the formulas $MC(\%) = ((C(H) - C(H = 0T))/C(H = 0T)) \times 100\%$ and $MR(\%) = ((R(H) - R(H = 0T))/R(H = 0T)) \times 100\%$, where C(H) and R(H) are the capacitance and the resistance, respectively, in a magnetic field H.

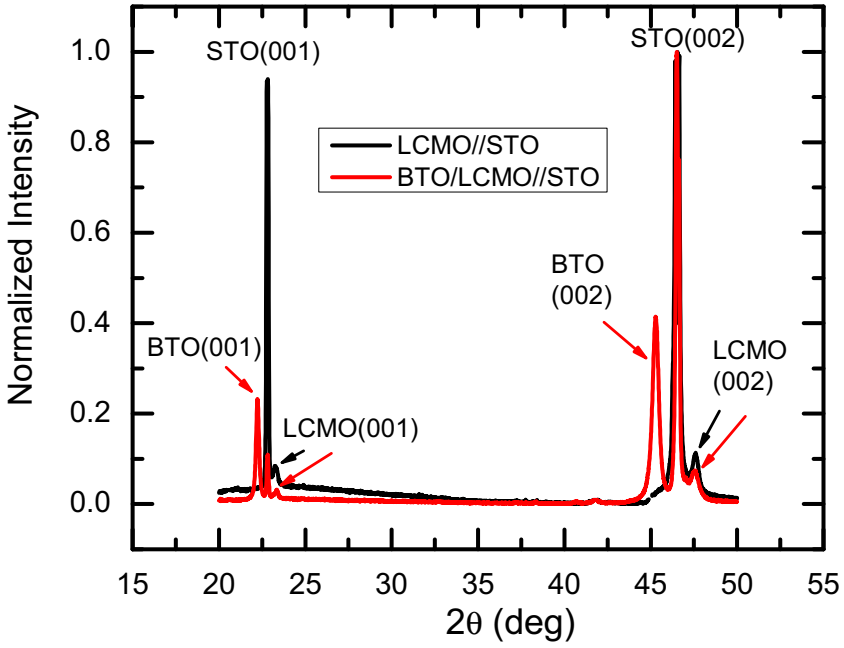


Figure 7.2: XRD patterns at room temperature for LCMO layer and BTO/ LCMO bilayer heterostructure grown on STO (001) substrate.

## 7.3 Results and discussion

Fig. 7.2 shows the XRD patterns of the BTO/LCMO heterostructure grown on an STO (001) substrate. Only the (00$l$) peaks of LCMO and BTO films are observed, indicating that both LCMO and BTO layers have grown epitaxially on the STO surface. The calculated out-of-plane (c-axis) lattice parameter for thin LCMO (16 nm thick) layer is $c_{film} \simeq 0.381$nm, while that for LCMO bulk sample is $c_{bulk} \simeq 0.386$nm (The c-axis lattice strain $\epsilon$ is 1.3% ( This is a compressive strain)). The larger lattice constant (0.3905nm) of the STO substrate causes an in-plane tensile strain, resulting in a compressive out-of-plane lattice strain in the LCMO film grown on the STO substrate. The calculated c-axis lattice parameter for BTO 360nm thick films is $c_{film} \simeq$ 0.402nm, which is close to the bulk value at room temperature $c_{bulk} \simeq 0.403$nm [18].

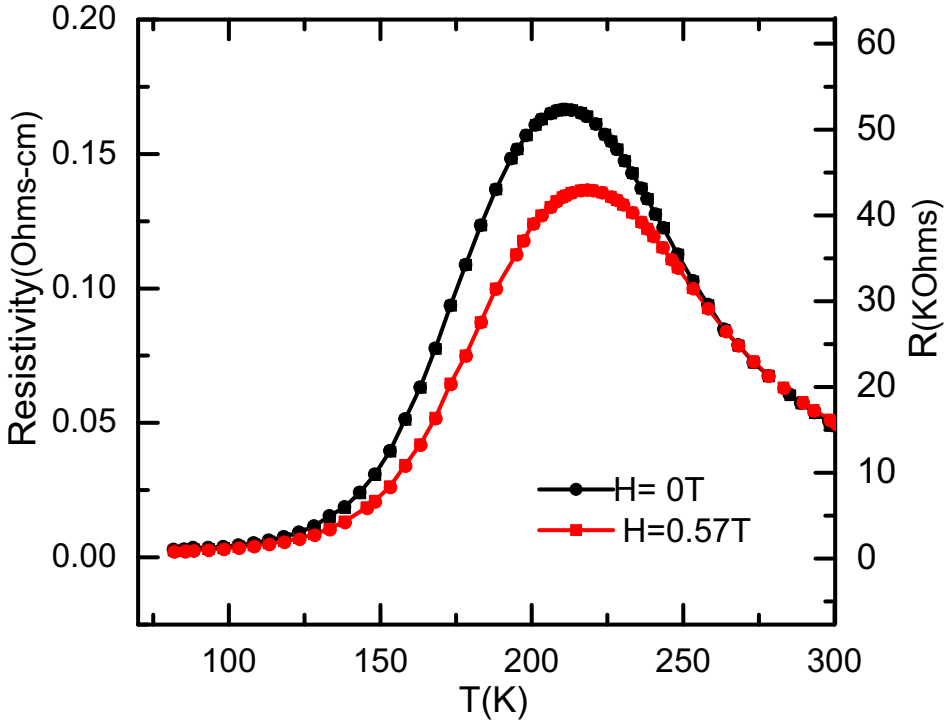


Figure 7.3: Resistivity/Resistance as a function of temperature in a zero magnetic field (H) and a field of H=0.57T, for LCMO layer of BTO/LCMO heterostructure grown on STO.

Fig. 7.3 shows the temperature dependent resistivity $\rho(T)$ (and the resistance R(T)) for the LCMO layer in the BTO/LCMO heterostructure measured at 0T and 0.57T. The LCMO layer shows an MIT at temperature $T_{MIT}$ = 212K. The applied magnetic field decreases the resistivity of the sample and shifts the $T_{MIT}$ to higher temperature (see Fig. 7.3). The sample exhibits a large negative MR (34%) in a small applied magnetic field of 0.57T, indicating the existence of magnetic property/ferromagnetism in the bilayer heterostructure.

Fig. 7.4 (a) and Fig. 7.4 (b) show the polarization- electric field (P-E) hysteresis loop of the heterostructure measured at room temperature (297K) and liquid nitrogen temperature (77K), respectively. At room temperature, the sample exhibits a large remnant polarization of $P_r = 3.6\mu c/cm^2$ and apparent coercive electric field of $E_c$ = 221kV/cm, whereas at 77K, $P_r = 3.4\mu c/cm^2$ and

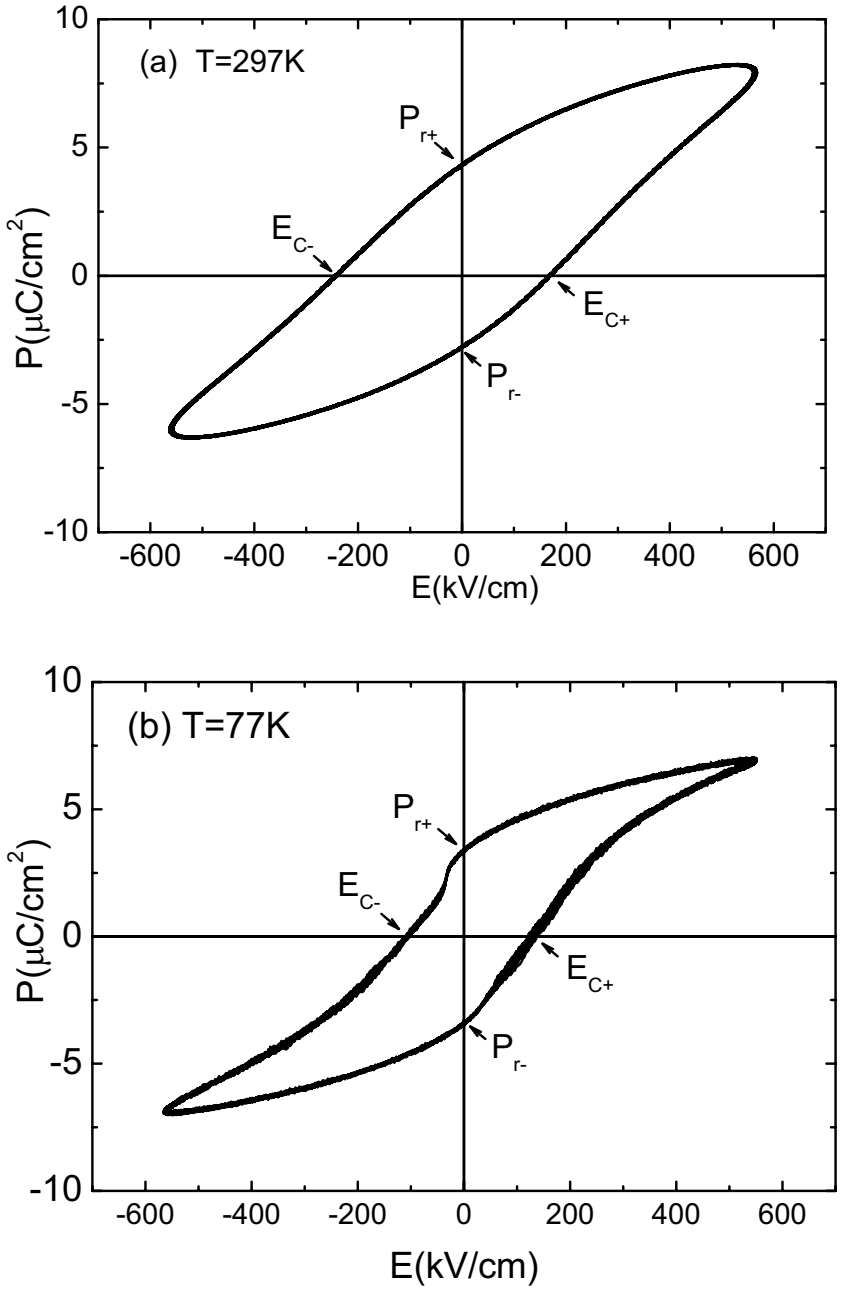


Figure 7.4: Ferroelectric hysteresis loop (P(E)) of the BTO/LCMO//STO heterostructure measured at a frequency of 125Hz for (a) room temperature (297K) and (b) liquid nitrogen temperature (77K).

$E_c$ = 121kV/cm. These results are consistent with previous studies of BTO film [19, 20]. We will return to the discussion of this temperature dependent P-E hysteresis loop later. The well-shaped P(E) hysteresis loops observed at two different temperatures confirm the existence of the ferroelectricity/ferroelectric property in the bilayer heterostructure at room temperature and low temperature.

The data shown in Fig. 7.5(a) illustrate whether or not this BTO/LCMO bilayer heterostructure is a multiferroic. Note that a ferroelectric sample does not show any change of the capacitance in an applied magnetic field. The presence of this non-magnetic feature in BTO has been confirmed by measuring the capacitance of our bulk BTO sample in a magnetic field. We did not observe any change of the capacitance in an applied magnetic field for a bulk BTO sample (see the inset of Fig. 7.5(a)). Fig. 7.5(a) shows the temperature dependent capacitance of the heterostructure in a zero field and a field of 0.57T. The sample undergoes two successive structural transitions (rhombohedral to orthorhombic at 180K and orthorhombic to tetragonal at 290K) and *a significant increase in the capacitance in the vicinity of MIT when a magnetic field is applied*. We observed similar structural transition (rhombohedral to orthorhombic at 205K and orthorhombic to tetragonal at 292K) in our bulk BTO samples (see the inset of Fig. 7.5(a)). The structural transition temperatures of BTO are in a good agreement with previous studies of bulk BTO [18, 22, 23]. The structural transition temperatures in the BTO thin film are different from those observed in the bulk BTO. This could be caused by the strain in the LCMO/STO structure. The intriguing change in the capacitance observed in the bilayer heterostructure in a magnetic field is the so-called MC effect.

The BTO shows paraelectricity above 408K (which is known as the Curie temperature, $T_c$ at which the spontaneous polarization disappears [18, 22, 23] ) and ferroelectricity below 408K (see Fig. 3.10 in Chapter 3 for $T_c$). The para-

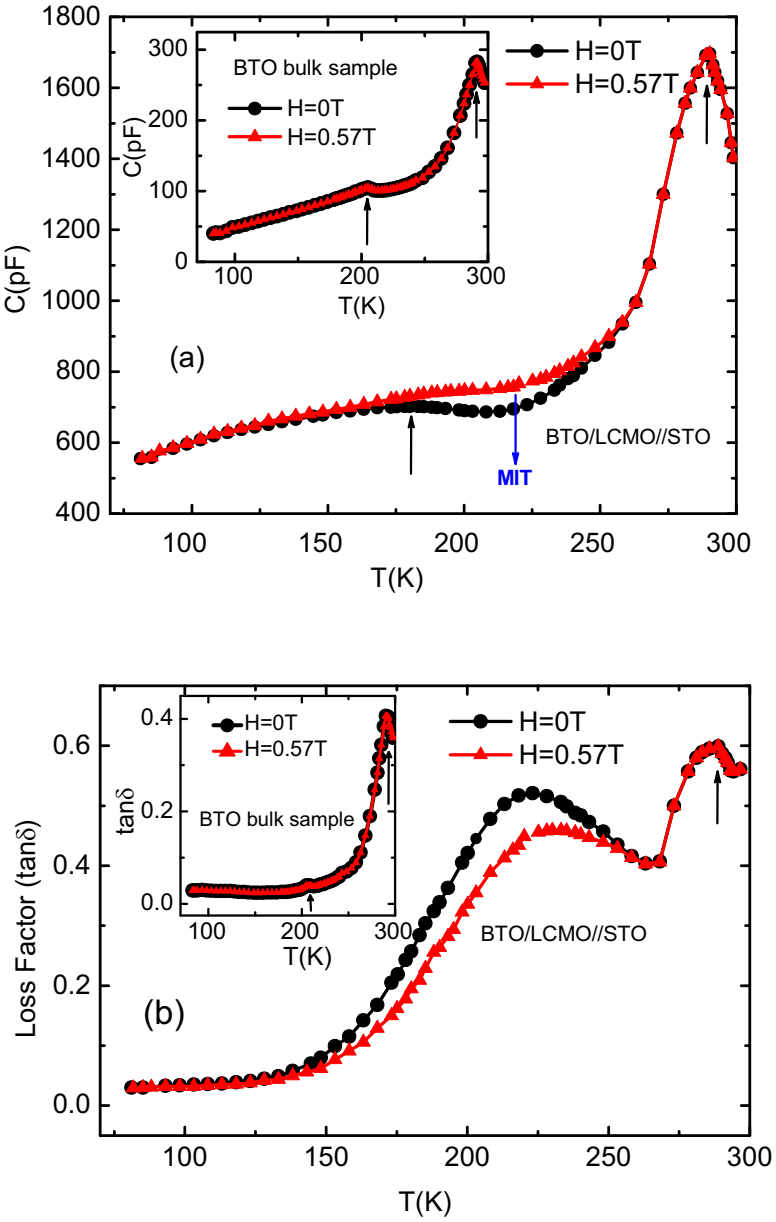


Figure 7.5: (a) The capacitance and (b) the loss factor ($\tan\delta$) as a function of temperature for the BTO/LCMO//STO heterostructure measured at a frequency of 1kHz in zero field and a field of 0.57T. The insets show the temperature dependent capacitance and loss factor ($\tan\delta$) for BTO bulk sample. The upward vertical arrows indicate the structural transition temperatures of the heterostructure and BTO bulk sample (see the text for details). The downward arrow (blue) indicate the metal to insulator transition temperature (MIT) for the LCMO layer of BTO/LCMO//STO heterostructure at 0.57T.

electric phase (non-ferroelectric) has the cubic perovskite structure with no spontaneous electric dipole moment [18, 22, 23]. Below 408K, the movement of the $Ti^{4+}$ ion relative to the $O^{2-}$ ion in the $TiO_6$ octahedra is considered to be responsible for the creation of a spontaneous electric dipole moment and ferroelectricity in BTO. The successive structural transitions from cubic paraelectric to tetragonal/orthorhombic/rhombohedral ferroelectrics are accompanied by a displacement of Ti ions with respect to the oxygen octahedra, leading to a distortion of the structure and an abrupt change in the dimensions of the crystal unit cell [18]. The structural distortions and the ionic shifts due to the change in temperature influence the electric dipole moments, dipole orientation and spontaneous polarization, leading to larger dielectric constants or capacitance response near the structural transition temperatures.

Fig. 7.5(b) shows the temperature dependent loss factor ($\tan\delta$) of the heterostructure in zero field and a field of 0.57T. It can be useful in clarifying the origin of the MC effect in the BTO/LCMO bilayer heterostructure. For the purpose of understanding the temperature dependent loss factor behavior in the BTO/LCMO bilayer heterostructure, we plotted the temperature dependent loss factor of the BTO bulk sample (see the inset of Fig. 7.5(b)). For the bulk BTO, the maximum loss factor occurs at the structural transition temperature 292K (and a small loss factor peak appears at the structural transition temperature 205K) and there is no change in the loss factor in a magnetic field (see the inset of Fig. 7.5(b)). In contrast, the maximum loss factor occurs around the MIT (212K) and at the structural transition temperature (290K) for the BTO/LCMO bilayer heterostructure (see Fig. 7.5(b)). The external magnetic field reduces the loss factor and shifts the loss peak around the MIT to high temperature in the heterostructure (see Fig. 7.5(b)), giving rise to a negative magnetoloss (ML) ( defined as $ML(\%) = ((\tan\delta(H) - \tan\delta(0T))/(\tan\delta(0T)) \times 100\%$, where $\tan\delta(H)$ and $\tan\delta(0T)$ are the loss factors with and without magnetic field) (see Fig. 7.6(b)).

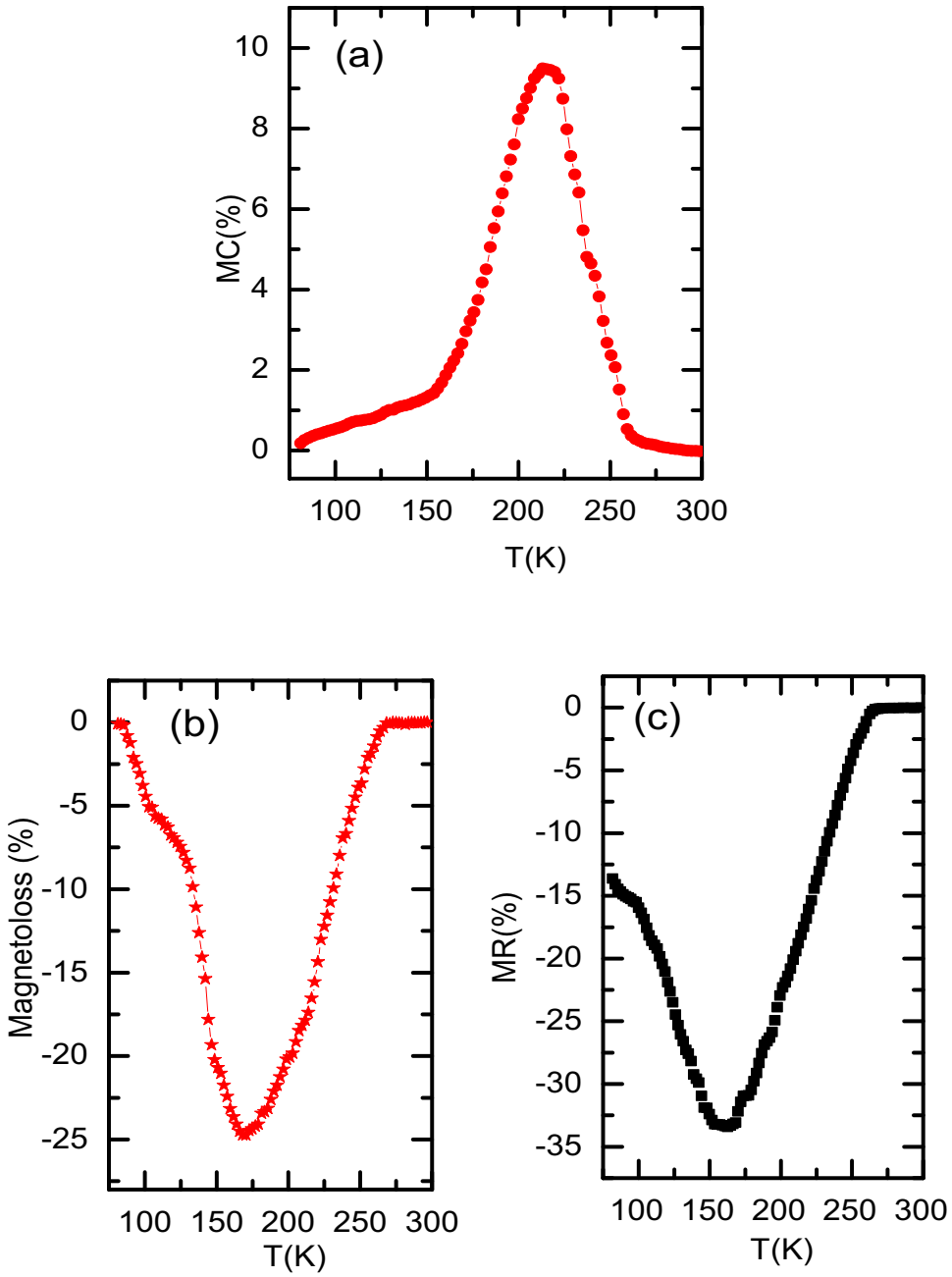


Figure 7.6: (a) Magnetocapacitance (MC), and (b) Magnetoloss as a function of temperature for the BTO/LCMO//STO heterostructure. (c) Magnetoresistance (MR) as a function of temperature for the manganite LCMO layer of BTO/LCMO//STO heterostructure .

This implies that the loss factor in the heterostructure is directly affected by the resistivity of the LCMO layer and by the magnetic field. Fig. 7.6(a) and (b) show the temperature dependent MC (which is observed between 77 K and $\sim$ 270 K) and ML (which is also observed between 77 K and $\sim$ 270 K) of the hetrostructure, respectively, and Fig. 7.6(c) shows the temperature dependent MR for the LCMO layer of the BTO/LCMO//STO heterostructure. We found a pronounced positive MC, negative ML and negative MR in the vicinity of MIT in our bilayer BTO/LCMO heterostructure.

We now discuss possible reasons for our observations. Recent measurements [14, 15, 16, 17, 24] on LCMO have found that a very thin film of LCMO grown on the STO substrate is subjected to the in-plane tensile strain, which favours the A-type OO-antiferromagnetic insulating (AFI) state and induces phase separation in the LCMO epitaxial film. Our XRD analysis also confirms the strong in-plane biaxial tensile strain in the LCMO film grown on STO, resulting in a 1.3% uniaxial compressive strain along the c-axis. The metal-insulator transition temperature is extremely sensitive to biaxial strain that have an impact on the Mn-O bond lengths as well as the Mn-O-Mn bond angles. In LCMO perovskite manganites, Mn ions are surrounded by O octahedra, and in high-spin configuration the Mn $t_{2g}$ states are filled and the electrically active orbitals are Mn $d_{x^2-y^2}$ $e_g$ and Mn $d_{3z^2-r^2}$ $e_g$. The tensile strain stretches the in-plane Mn-O bond lengths and so that the overlapping between Mn 3d and O 2p orbitals is reduced. As a result, the degeneracy of the Mn $e_g$ orbitals is lifted by lowering the $x^2-y^2$ orbitals. The strain/deformation of the $MnO_6$ octahedra due to the film (LCMO)-substrate (STO) mismatch (+1.2%) enhances the Jahn-Teller distortion (see Chapter 2, section 2.2) and increases the localization of charge carriers in the LCMO films. As a result, the double exchange interaction is weakened, and the appearance of the AFI state leads to a decrease of $T_{MIT}$ (212K) in the thin film compared to that in the bulk (270K). Since MIT in a very thin LCMO layer is percolative in

nature, the large negative MR observed in the vicinity of MIT (see Fig. 7.3) is the result of melting of AF clusters by a magnetic field, which in turn enhances the volume of the ferromagnetic metallic (FMM) phase as well as the percolative conduction paths.

The remnant polarization and the coercive field of the sample are different at temperatures 297K and 77K (see Fig. 7.4). In general, ferroelectric material contains electric dipole moments and multiple domains (a domain is a small region of a ferroelectric, in which all the electric dipole moments have the same orientation) that have two or more orientational states in the absence of an electric field. The domains are separated by interfaces called domain walls. The electric dipole moments can be aligned/switched by an applied electric field. The P-E hysteresis loop in the BTO at a fixed temperature (as shown in Fig. 7.4 (a,b)) is mainly due to the growth of parallel/antiparallel domains under the ac electric field. Such growth occurs by motion of the domain walls and nucleation of new domains. From the structural point of view, the onset of polarization in the BTO perovskite ferroelectrics is described by the shifts of $Ti^{4+}$ and $O^{2-}$ ions relative to the large $Ba^{2+}$ cations [25]. The structural transitions of our heterostructure are also evident in the C(T) measurement (see Fig. 7.5(a)). For example, the sample structure is tetragonal at 297K and rhombohedral at 77K [18]. The structural transition is accompanied by changes in the dimensions of the crystal unit cell, resulting in the change of the lattice strain [25], which can affect the domain wall motion and polarization. The variation of temperature modifies lattice parameters and strain, dipole moments and dipole orientations, and consequently the P(E) hysteresis loop / polarization and coercive field. For an ideal P(E) hysteresis loop, $E_{c+} = E_{c-}$, and $P_{r+} = P_{r-}$. We also see a shift of the P(E) hysteresis loops (i.e., $E_{c+} \neq E_{c-}$ and $P_{r+} \neq P_{r-}$) in Fig. 7.4, which may be due to the two different electrodes at the BTO interfaces (such as the Ag layer on the top and LCMO layer at the bottom). The work functions of metallic electrodes and dielectric material are

different, and they have different density of charge carriers. Charge can build up at the two interfaces due to different permittivity and conductivity with different relaxation times. The two different electrodes at the BTO interfaces can create asymmetrical charge defects/trapped electrons at the interfaces [25]. The charge defects and trapped electrons inhibit the domain-wall motion [25] and thus affect the shape of the P(E) hysteresis loops.

In order to explain a large MC observed in the vicinity of the MIT (see Fig. 7.5(a) and Fig. 7.6(a)), we refer to the mechanism previously reported by Catalan et al. in Ref.[11]. Maxwell-Wagner space charge can be trapped at the electrode-ferroelectric interfaces, grain boundaries or phase-separated clusters yielding a capacitance/dielectric response [11]. Note that the thin LCMO film is phase separated (PS). It is used as a bottom electrode for the capacitance measurement and also as a magnetic layer in the bilayer heterostructure (see Fig. 3.8 in chapter 3). Its resistance is $\sim 5.3 \times 10^4 \Omega$ at MIT (see Fig. 7.3). We consider that the effective capacitance response in our heterostructure comes from the BTO layer, the interface between BTO and LCMO, and the LCMO electrode [26]. Because of the negative sign of the magnetoresistance in the LCMO, the electrode resistance becomes smaller in a magnetic field. It allows the current to flow through the LCMO electrode, resulting in a voltage drop occurring across the highly resistive BTO layer and the BTO-LCMO interface (for example, the resistivity of the BTO layer is $\rho = 10^5 - 10^8 \Omega$cm [11] and that of the LCMO film is $10^{-1} \Omega$cm; the BTO-LCMO interface should have higher resistivity compared to the LCMO electrode because of the charge, spin, and orbital reconstructions [8, 27]). The interface resistivity is also affected by the magnetic field due to the phase separation in the LCMO [26]. The magnetic field thus reduces the dielectric thickness (a thickness of the BTO-LCMO heterostructure having high resistivity and yielding a capacitance/dielectric response to an electric field) [11, 28] (see Fig. 1.8 in Chapter 1), and also increases the effective area of the electrode by melting the AFI phase in the

phase separated LCMO. As the result, the measured capacitance in the heterostructure increases with an increasing applied magnetic field (capacitance $\propto$ electrode area/dielectric thickness).

The behaviour of the loss factor in the heterostructure in a magnetic field also supports the mechanism of the MC described above. The resistance of the LCMO thin film and the interface are major factors which affect the value of the measured loss in the vicinity of the MIT. The loss factor decreases with an increasing magnetic field (see Fig. 7.5(b)), implying that the voltage drop decreases across the LCMO layer and the interface and most of the voltage drop occurs across the highly resistive BTO layer. We thus conclude that the 'positive' MC (an increase of capacitance with magnetic field)(see Fig. 7.5(a) and Fig. 7.6(a)) in the bilayer heterostructure is mainly due to the effect of the interface between the LCMO and BTO layers and the negative MR effect of the phase separated LCMO. This is consistent with Catalan et al.'s arguments based on the Maxwell-Wagner model (see Chapter 1, Fig. 1.8 for details). As mentioned earlier, Singh et al. reported the observation of a 3% MC effect per Tesla at 1kHz and 100K in the BTO/LCMO superlattice. In contrast MC in our bilayer heterostructure is close to 10% at 1kHz and 212K in a field of 0.57T.

Finally, we return to the results of Singh et al.[9], who studied the magnetoelectrical properties of $BaTiO_3/La_{0.70}Ca_{0.30}MnO_3$ heteroepitaxial superlattice (composed of 25 repeated units of BTO(6nm)/LCMO(2nm) bilayer with LCMO as the bottom electrode) grown on an STO substrate, and reported the observation of a 'negative' MC effect (a decrease of capacitance in a magnetic field) (see Chapter 1, Fig. 1.7) in the negative magnetoresistive heteroepitaxial superlattice. They concluded that the coupling between magnetic and dielectric orders gave rise to this negative MC effect. This mechanism is different from that reported by Catalan et al.[11]. However, the detailed mechanism of the origin of the negative MC in an applied magnetic field was not provided

by Singh et al.[9].

The positive MC observed in our measurement is in contrast to Singh et al.'s negative MC observed in the heteroepitaxial multilayer superlattice. The mechanism of this 'negative' MC is puzzling. The discrepancy between our measurement and Singh et al.'s could be due to the difference in the thickness of BTO/LCMO layers and the number of BTO-LCMO interfaces (Singh et al.'s heteroepitaxial superlattice is composed of 25 repeated units of an 'ultra-thin' BTO (6 nm) /LCMO(2 nm) bilayer that has 25 BTO-LCMO interfaces, whereas in our measurement the epitaxial heterostructure is composed of one unit of BTO(360 nm) /LCMO(16 nm) bilayer that has only one BTO-LCMO interface). The extreme sensitivity of the MC to these factors is certainly interesting, and requires further investigation of the BTO/LCMO epitaxial heterostructure by decreasing the thickness of the layers and increasing the number of BTO-LCMO interfaces.

## 7.4 Summary

We have successfully synthesized an epitaxial $BaTiO_3/La_{0.66}Ca_{0.34}MnO_3$ bilayer heterostructure on a $SrTiO_3$ (STO) substrate, and investigated its structural and magnetoelectical properties. The heterostructure exhibits well-shaped ferroelectric polarization at room temperature and at 77K. Its MC reaches $\sim 10\%$ at the MIT (212K) in a magnetic field of 0.57T, which is opposite in sign and larger than the MC (3% per Tesla at 100K) found in a $BaTiO_3/La_{0.70}Ca_{0.30}MnO_3$ multilayer heterostructure by other groups (Singh et al.[9]). Our results demonstrate that the observed 'positive' MC in the bilayer manganite/ferroelectric heterostructure is due to negative magnetoresistive effects, (consistent with Catalan et al.'s arguments based on the Maxwell-Wagner model [11, 28]), which can be controlled by the strain induced phase separation and by the external magnetic field. The colossal magnetocapaci-

tance effect at room temperature can be achieved by choosing optimized ferroelectric and magnetoresistive materials.

# Bibliography


[1] R. Ramesh, and N. A. Spaldin, Nature Mater. **6**, 21 (2007).

[2] C. A. F. Vaz, J. Phys.: Condens. Matter. **24**, 333201 (2012).

[3] S.-W. Cheong, and M. Mostovoy, Nature Mater.**6**, 13 (2007).

[4] H. Béa, M. Gajek, M. Bibes, and A. Barthélémy, J. Phys.: Condens. Matter. **20**, 434221 (2008).

[5] G. Srinivasan, E. T. Rasmussen, J. Gallegos, R. Srinivasan, Yu. I. Bokhan, and V. M. Laletin, Phys. Rev. B **64**, 214408 (2001).

[6] F. Yen, C. dela Cruz, B. Lorenz, E. Galstyan, Y. Y. Sun, M. Gospodinov, and C. W. Chu, J. Matter. Res. **22**, 2163 (2007).

[7] J. Ma , J. M. Hu , Z. Li , and C.-W. Nan, Adv. Mater.**23**, 1062 (2011).

[8] C. A. F. Vaz, J. Hoffman, Y. Segal, J.W. Reiner, R. D. Grober, Z. Zhang, C. H. Ahn, and F. J. Walker, Phys. Rev. Lett. **104**, 127202 (2010).

[9] M. P. Singh, W. Prellier, Ch. Simon, and B. Raveau, Appl. Phys. Lett. **87**, 022505 (2005).

[10] P. Murugavel, D. Saurel, W. Prellier, Ch. Simon, and B. Raveau, Appl. Phys. Lett. **85**, 4424 (2004).

[11] G. Catalan, Appl. Phys. Lett. **88**, 102902 (2006).

[12] M. Clausse, Colloid & Polymer Sci. **253**, 1020 (1975).

[13] Y. M. Xiong, G. Y. Wang, X. G. Luo, C. H. Wang, X. H. Chen, X. Chen and C. L. Chen, J. Appl. Phys. **97**, 083909 (2005).

[14] N. L. Guo, J. Li, Y. F. Wei, Y. Zhang, L. M. Cui, L. Zhao, Y. R. Jin, H. Y. Tian, Hui Deng, G. P. Zhao, and D. N. Zheng, J. Appl. Phys. **112**, 013907 (2012).

[15] A. Baena, L. Brey, and M. J. Calderón, Phys. Rev. B **83**, 064424 (2011).

[16] J. Klein, J. B. Philipp, G. Carbone, A. Vigliante, L. Alff, and R. Gross, Phys. Rev. B **66**, 052414 (2002).

[17] L. Abad, V. Laukhin, S. Valencia, A. Gaup, W. Gudat, L. Balcells, and B. Martinez, Adv. Funct. Mater. **17**, 3918 (2007).

[18] G. H. Kwei, A. C. Lawson, S. J. L. Billinge and S.-W. Cheong, J. Phys. Chem. **97**, 2368 (1993).

[19] H. H. Wieder, Phys. Rev. **99**, 1161 (1955).

[20] A.L. Meier, A.Y. Desai, L. Wang , T.J. Marks and B.W. Wessels, J. Mater. Res. **22**, 1384 (2007).

[21] D. Khomskii, Physics **2**, 20 (2009).

[22] N. G. Kim, Y. S. Koo, C. J. Won, N. Hur, J. H. Jung, J. Yoon, Y. Jo, and M. H. Jung, J. Appl. Phys. **102**, 014107 (2007).

[23] K. Kinoshita, and A. Yamaji, J. Appl. Phys. **47**, 371 (1976).

[24] E. Rozenberg, V. Markovich, Ya. Yuzhelevskii, G. Gorodetsky and M. Ziese, J. Appl. Phys. **95**, 7103 (2004).

[25] D. Damjanovic, Rep. Prog. Phys. **61**, 1267 (1998).

[26] S. Yang, S. Dong, Y. Liu, Y. Yao, Y. Yin, and X. Li, J. Appl. Phys. **114**,034102 (2013).

[27] H. Lu, T. A. George, Y. Wang, I. Ketsman, J. D. Burton, C.-W. Bark, S. Ryu, D. J. Kim, J. Wang, C. Binek, P. A. Dowben, A. Sokolov, C.-B. Eom, E. Y. Tsymbal, and A. Gruverman, Appl. Phys. Lett. **100**, 232904 (2012).

[28] G. Catalan, and J. F. Scott, Nature **448**, doi:10.1038/nature06156 (2007).

# Chapter 8

# Summary

Manganite, a complex system in the correlated electron physics, has recently attracted lots of interest because of its colossal magnetoresistance, rich electric and magnetic phase diagrams and promising applications in electronics and nanodevices. This complex material is also exciting because it manifests intrinsic phase separation (phase coexistence of ferromagnetic metal, antiferromagnetic insulator or paramagnetic insulator phases) and a strong coupling interaction between charge, orbital, lattice, and spin degrees of freedom. The effects of external stimuli such as electric field/current excitation, magnetic fields, Mn-site doping, and strain on the physical properties of perovskite manganites (bulk and epitaxial thin films) were investigated in order to achieve understanding and control of properties suitable for applications. They are summarized in the sections below:

(I) The dependence of a materials electrical resistance on the magnitude of an electric field/current is known as electroresistance (ER). This property is of scientific interest and also has ramifications for applications such as those involving non-volatile memory elements. Following the first report [1] related to the high electric field-induced melting of charge ordering, several authors suggested that Joule heating could lead to a current-induced ER in manganites. Recently, interesting ER results were obtained by Rebello *et al.* [2] and

Mohan *et al.* [3] on $Sm_{0.60}Sr_{0.40}MnO_3$ and $Sm_{0.55}Sr_{0.45}MnO_3$, respectively. Rebello *et al.* investigated the ER of $Sm_{0.60}Sr_{0.40}MnO_3$ using dc current and concluded that the results could be caused primarily by Joule heating. Mohan *et al.* investigated the ER of $Sm_{0.55}Sr_{0.45}MnO_3$ using pulsed current (dc current for a few milliseconds) and reported an observation of giant intrinsic ER in $Sm_{0.55}Sr_{0.45}MnO_3$. They explained this result using the percolative mechanism of phase separation. This results on $Sm_{0.60}Sr_{0.40}MnO_3$ and $Sm_{0.55}Sr_{0.45}MnO_3$ raise questions about the origin of ER. In order to better understand the origin of ER, we developed a technique that allowed us to precisely measure the 'intrinsic' ER of a material. This technique had been utilized to measure the ER of the two compositions mentioned above. The comparison study of the intrinsic ER of $Sm_{0.60}Sr_{0.40}MnO_3$ and $Sm_{0.55}Sr_{0.45}MnO_3$ led us to pursue further study of the ER of $Sm_{0.60}Sr_{0.40}MnO_3$ to probe the possible mechanisms involved using chemical doping. These topics are summarized below in sections 8.1 and 8.2.

(II) Time dependent (relaxation) effects in ER or colossal magnetoresistive manganites influence their physical properties and may limit their technological applicability. To our knowledge, experiments have not revealed an explicit mechanism responsible for the relaxation effect in manganites. In order to understand the effect of the relative amounts of the ferromagnetic metallic (FMM) and non-FMM phases on the relaxation of resistivity, we studied the time dependent electrical transport of several manganites in which the relative fraction of FMM and non-FMM phases were modified. This topic is summarized below in Section 8.3.

(III) Single-phase multiferroics exhibit weak magneto-electric effects. Recently, epitaxial ferroelectric/manganite heterostructure has received lots of interest because charge, spin, and orbital order at the interfaces is responsible for many unusual multiferroic properties. Besides the scientific interest in their physical properties, multiferroics are potential candidates for new appli-

cations/devices, including sensors or multistate memories. The dependence of a materials capacitance on the magnitude of a magnetic field is known as the magnetocapacitance (MC), and the MC effect is usually used to determine whether or not a material exhibits multiferroic properties. Based on the Maxwell-Wagner model, Catalan *et al.*[4] reported that the negative magnetoresistive manganite layer can produce a positive MC effect in a sample consisting of the $BaTiO_3$ and manganite layers. This is opposite in sign to the MC effect found in $BaTiO_3/La_{0.70}Ca_{0.30}MnO_3$ heteroepitaxial superlattices by Singh *et al.* [5]. This contradictory result raised questions about the mechanism of the MC. In order to understand the mechanism of the MC effect and fabricate a multiferroic sample that exhibits a large MC effect at low magnetic fields, we synthesized the epitaxial $BaTiO_3/La_{0.66}Ca_{0.34}MnO_3$ heterostructure on a $SrTiO_3$ (STO) substrate, and investigated its magnetoelectical properties. This topic is summarized below in Section 8.4.

## 8.1 Intrinsic electroresistance of $Sm_{0.60}Sr_{0.40}MnO_3$ and $Sm_{0.55}Sr_{0.45}MnO_3$

The *intrinsic* electroresistance of $Sm_{0.60}Sr_{0.40}MnO_3$ and $Sm_{0.55}Sr_{0.45}MnO_3$, synthesized in the same way, was investigated by passing short current pulses through these materials. The goal of these experiments was to drastically reduce the Joule heating contribution to the measured electroresistance. The resulting electroresistance depends on the magnitude of the current, and undergoes larger changes in the $Sm_{1-x}Sr_xMnO_3$, $x = 0.40$ sample compared to those in the $x = 0.45$ sample. Other studies have noted that at low temperatures the $x = 0.40$ sample has a phase separated ferromagnetic metallic (FMM) ground state with the A-type antiferromagnetic (AF) and small amounts of CE-type (charge ordered) AF clusters, whereas the low temperature ground state in the $x = 0.45$ sample is homogeneous and ferromagnetic metallic. This

is consistent with our observation that the $x = 0.45$ sample had a lower peak resistivity and higher metal to insulator transition ($T_{MIT}$) than the $x = 0.40$ one. We attributed the difference in change in the electroresistance to the contrasting homogeneity of these two compositions.

Our estimates of the electroresistance ( $\sim$45% and $\sim$10% for $x = 0.40$ and $x = 0.45$, respectively) are dramatically smaller than the electroresistance in the same compositions previously measured by others ( $\sim$ 2500% for $x = 0.45$ [3]). The huge difference between our measurements and those of Ref. [3] is not fully understood. The morphology of the polycrystalline bulk samples, which are sensitive to the preparation conditions (such as sintering temperature, annealing time, sintering atmosphere, and pressure applied during preparation of pellets), as well as the quality of the contacts used for the electrical transport measurements are just some of the factors that may influence their resistivities and their dependence on the magnitude of the current (for instance, the sample in Ref. [3] has higher resistivity and lower $T_{MIT}$ than ours).

It is also important to establish whether the controlling parameter is the current or the current density when analyzing the intrinsic ER in manganites. It was found that for each composition plots of the intrinsic electroresistance versus current density measured in the samples with different dimensions and resistances coincide, whereas this does not happen when plots of the electroresistance versus current magnitude are constructed. These results confirm that the current density is indeed the relevant universal parameter for controlling the intrinsic electroresistance of these manganites. Even though these experiments were carried out for $Sm_{1-x}Sr_xMnO_3$ only, they are likely to be applicable to other manganites. The experimental technique to precisely measure the *intrinsic* ER of a material is described in Chapter 4 and can be used to understand and tailor electroresistive materials for applications.

## 8.2 Disorder enhanced intrinsic electroresistance in $Sm_{0.60}Sr_{0.40}Mn_{1-x}Fe_xO_3$

Investigations of $Sm_{1-x}Sr_xMnO_3$ (SSMO) revealed that the changes in the *intrinsic* electroresistance are much more significant in $Sm_{0.60}Sr_{0.40}MnO_3$ compared to those in $Sm_{0.55}Sr_{0.45}MnO_3$, hinting that spatial inhomogeneities related to the multiphase coexistence are important in determining the intrinsic ER in SSMO. Therefore, we tuned the existing disorder/inhomogeneity in $Sm_{0.60}Sr_{0.40}MnO_3$ by Fe doping on the Mn site to probe the mechanisms responsible for the ER. The Mn-site doping by Fe has attracted interest since the ionic size of $Fe^{3+}(3d^5{:}t_{2g}^3e_g^2)$ is almost identical to that of $Mn^{3+}(3d^4{:}t_{2g}^3e_g^1)$. This minimizes the effects of lattice distortion upon substitution, and more readily reveals phenomena associated with changes in the electronic configuration. We found that the intrinsic ER has dramatically increased with an increasing Fe content in $Sm_{0.60}Sr_{0.40}Mn_{1-x}Fe_xO_3$ ($0 \leq x \leq 0.02$), while it has decreased with an increasing magnetic field.

Replacement of some $Mn^{3+}(3d^4{:}t_{2g}^3e_g^1)$ with $Fe^{3+}(3d^5{:}t_{2g}^3e_g^2)$ in $Sm_{0.60}Sr_{0.40}Mn_{1-x}Fe_xO_3$ induces the antiferromagnetic (AF) coupling between $Fe^{3+}$ and $Mn^{4+}$ ions and leads to a competition between the AF superexchange (a antiferromagnetic insulating interaction between $Mn^{3+}$ and $Mn^{3+}$ ions or between $Fe^{3+}$ and $Mn^{4+}$ ions) and the ferromagnetic (FM) double exchange (a ferromagnetic metallic interaction between $Mn^{3+}$ and $Mn^{4+}$ ions). Consequently, there is a decrease in the $e_g$ electron hopping which in turn increases the resistivity and decreases the metal-to-insulator transition temperature ($T_{MIT}$) and Curie temperature ($T_C$) of the Fe doped SSMO system. Moreover, the existence of a small amount of Fe, randomly distributed in the SSMO manganites, has been associated with the formation of different size-distributed new AF clusters. Fe doping in SSMO, therefore, enhances the disorder (spin disorder) in the magnetic structure of the system resulting in a more inhomo-

geneous system. It is known that percolation between randomly distributed ferromagnetic metallic (FMM) clusters plays an important role in determining the conduction properties of phase separated manganites. When a current is applied to a phase separated sample, the boundaries between metallic and insulating regions are strongly influenced. The electric field associated with the applied current changes the relative volume fractions of metallic and insulting regions in a phase separated system because accumulation of conducting electrons in the metallic/insulating boundaries causes the interface to move. If the boundaries of the FMM clusters are close together, links between them may be created and/or new filamentary conduction paths may be formed which, in turn, decreases the resistivity to a high current applied to the sample. In a more inhomogeneous sample, i.e., with higher Fe concentration, the electric field associated with an applied current creates a larger relative perturbation of coexisting inhomogeneous magnetic states. The larger tendency to develop filamentary conduction paths and/or decrease the barrier height for charge carrier tunneling results in a more dramatic change in the intrinsic ER with Fe doping in SSMO. Application of a magnetic field to a manganite enhances the magnetic homogeneity of the sample through a melting of the insulating state and a subsequent increase in the FMM state. Hence, the intrinsic ER is expected to be suppressed by a magnetic field. The results imply that the intrinsic electroresistance increases with the inhomogeneity of the sample.

As mentioned earlier, the ER effect in manganites is of scientific interest and also has ramifications for applications such as those involving non-volatile memory elements. These results can be useful for understanding the mechanism of the ER, as well as the phase-separated manganites in general.

## 8.3 Disorder controlled time dependent electrical transport in doped $Sm_{0.60}Sr_{0.40}MnO_3$ and $(Sm_{0.5}Gd_{0.5})_{0.55}Sr_{0.45}MnO_3$ manganites

The time dependence of electrical resistivity has been investigated systematically in Fe, $BaTiO_3$ (BTO), and Ru doped $Sm_{0.60}Sr_{0.40}MnO_3$ (SSMO), SSMO+BTO and $(Sm_{0.5}Gd_{0.5})_{0.55}Sr_{0.45}MnO_3$ (SGSMO). The goal of these experiments was to understand the effect of the relative amount of FMM and non-FMM phases on the relaxation of resistivity in order to control it. As discussed in previous chapters, $Sm_{1-x}Sr_xMnO_3$ with $x \sim 0.40$ composition possesses a number of unique electronic and magnetic properties (for instance, large ER [6], low field CMR [7], giant magnetostriction [7] and a huge magnetocaloric effect [8]) compared to other manganites. To the best of our knowledge, time dependent electric properties have not been studied before for this important manganite. We doped the $Sm_{0.60}Sr_{0.40}MnO_3$ (SSMO) manganite with Fe ( on the Mn site) and also introduced BTO into the pristine manganites to enhance the amount of the non-FMM phases in the manganite system. Recent investigation of the effects of Ru doping (on the Mn site) on the magneto-transport of $(Sm_{0.5}Gd_{0.5})_{0.55}Sr_{0.45}MnO_3$ (SGSMO) revealed that a small amount of Ru doping increases the FMM phase of the system, moving the system away from the spin-glass-like insulating state [9]. We also chose this known Ru doped manganite system to study the effect of the FMM phase on the relaxation of resistivity.

Replacing some Mn with Fe leads to antiferromagnetic (AF) coupling between $Fe^{3+}$ and $Mn^{4+}$ ions and introduces magnetic disorder into the ferromagnetic metallic (FMM) ground state of the SSMO manganite system. Substituting the BTO, a nonmagnetic insulating material, into the SSMO manganites induces disorder or strain in the system. The BTO doping also produces an

additional energy barrier (an increase in the carrier scattering) to the electrical transport in SSMO manganites. On the other hand, the presence of the valence states $Ru^{4+}(4d^4{:}t_{2g}^4e_g^0)$ and $Ru^{5+}(4d^3{:}t_{2g}^3e_g^0)$ in Ru doped SGSMO leads to an increase in the $Mn^{3+}(3d^4{:}t_{2g}^3e_g^1)$/ $Mn^{4+}(3d^3{:}t_{2g}^3e_g^0)$ ratio (increased $e_g$ electron density) and provides another ferromagnetic coupling pair $Mn^{3+}$- $Ru^{5+}$, in addition to the $Mn^{3+}$- Mn $^{4+}$ one. Ru doping of SGSMO thus promotes FMM states and destroys the inherent short-ranged charge ordered/orbital ordered AF insulating (AFI) clusters, leading to a homogeneous magnetic system.

It was found that the relaxation rates of resistivity ($S$) are large when the SSMO is doped with Fe and BTO; however, they are suppressed by Ru substitution in SGSMO. A competition of the coexisting magnetic clusters (for example FMM, AFI) implies a frustration at FMM/AF insulating phase boundaries and its metastability, and a continuous variation in the coexisting phase fractions with time leads to the relaxation of resistivity in our phase-separated manganite system. Fe and BTO doping not only increase the insulating phase in volume but also increase the number of (magnetically disordered) interfaces between FMM and AFI clusters in the samples. In more disordered/inhomogeneous magnetic systems (Fe doped SSMO and BTO doped SSMO+BTO), the intercluster spin frustration and phase transformation are more pronounced resulting in a faster relaxation of resistivity. The opposite trend is observed in Ru doped SGSMO samples, where a decrease in the intrinsic inhomogeneity/disorder or intercluster spin frustration result in a dramatic decrease in the time decay of the resistivity.

The appearance of a strong phase competition, the easy phase transformation due to the small energy barrier between coexisting phases, and the reorientation of magnetic moments/spins in the vicinity of ferromagnetic metal to paramagnetic insulator transition ($T_{MIT}$) and AF ordering temperature ($T_A$) result in faster resistivity relaxation, giving rise to the negative and positive peaks in $S(T)$ around the $T_A$ and $T_c/T_{MIT}$, respectively. A large negative

relaxation rate of resistivity was found at low temperatures near $T_A$ . On the other hand, a large positive relaxation rate of resistivity was found near $T_c$ or $T_{MIT}$ for all three manganite systems. The FMM phase dominates over the AFI phase in the low temperature region. At low temperatures (around $T_A$), the fraction of FMM domains is smaller than its corresponding equilibrium value, and its volume increases with time, leading to a negative relaxation rate of resistivity. On the other hand, FMM double exchange interaction weakens near the $T_{MIT}/T_c$ due to the high thermal energy, and break-up of large FMM domains and the appearance of additional domain walls lead to a positive relaxation rate of resistivity around $T_{MIT}$. Note that the newly created domain walls act as scattering centers for the carriers and increase the resistivity.

Both the negative and positive relaxation of resistivity ($S_{min}$ near $T_A$ and $S_{max}$ near $T_c/T_{MIT}$) depend strongly on the thermal hysteresis width $\Delta T$ (defined as an extent of the inhomogeneous magnetic state or disorder in a manganite system), which can be controlled either by an increasing amount of FMM phases or by an increasing amount of non-FMM phases. Doping SSMO with Fe and BTO causes a more inhomogeneous/disorder magnetic system as evidenced by an increase of the $\Delta T$ with an increasing Fe and BTO content in SSMO. On the other hand, doping SGSMO with Ru makes a more homogeneous magnetic system as evidenced by a decrease of $\Delta T$ with an increasing Ru content in SGSMO. The interplay between the intrinsic disorder and strong electronic and magnetic correlations in the mixed-valent manganites frustrate the nucleation, giving rise to the observed doping dependence of the resistive relaxation. The data obtained on these three systems revealed a gradual exponential-like increase of the $S_{min}$ and $S_{max}$ with an increasing $\Delta T$. These results imply that the relaxation of resistivity in manganites depends on $\Delta T$, that is, it can be tuned by modifying the relative amount of the FMM and non-FMM phases.

## 8.4 Magnetocapacitance effect in the epitaxial $BaTiO_3/La_{0.66}Ca_{0.34}MnO_3$ heterostructure

Our epitaxial $BaTiO_3/La_{0.66}Ca_{0.34}MnO_3$ (BTO/LCMO) heterostructure deposited on a $SrTiO_3$ (STO) substrate revealed well-shaped ferroelectric polarization at room and low temperatures (77K), and $\sim$ 10% magnetocapacitance at the MIT (212K) under a magnetic field of 0.57T. This is larger than the MC (3% per Tesla at 100K) found in the $BaTiO_3/La_{0.70}Ca_{0.30}MnO_3$ heteroepitaxial superlattice by Singh *et al.* [5]. Our results demonstrate that the observed positive magnetocapacitance in the bilayer manganite/ferroelectric heterostructure is mainly a negative magnetoresistive effect that can be controlled by strain induced phase separation and by an external magnetic field. This is consistent with Catalan *et al.*'s arguments based on the Maxwell-Wagner model [4]. The colossal magnetocapacitance effect at room temperature can be achieved by choosing optimized ferroelectric and magnetoresistive materials. The ferroelectric and manganite bilayer heterostructure manifests the electric field dependence of ferroelectric polarization and a notable magnetocapacitance effect under a magnetic field (i.e., the sample responds to both electric and magnetic fields). This magnetocapacitance effect in an epitaxial heterostructure could be of use in future electronic devices (for example, multifunctional sensors).

The positive MC, observed in the bilayer heterostructure composed of BTO(360nm)/LCMO(16nm) of our study is in contrast to Singh *et al.*'s negative MC observed in the multilayer heterostructure composed of 25 repeated units of 'ultrathin' BTO(6nm)/LCMO(2nm) bilayers. The mechanism of this 'negative' MC is puzzling and still not fully understood. The discrepancy between our measurements and those of Singh *et al.*'s could be due to a number of factors such as the difference in the thickness of BTO/LCMO layers and the number of BTO-LCMO interfaces (Note that Singh et al.'s heteroepitaxial

superlattice has 25 BTO-LCMO interfaces, whereas in our measurement the epitaxial heterostructure has only one BTO-LCMO interface.) The extreme sensitivity of the MC to these factors is certainly intriguing, and requires further investigation of the BTO/LCMO epitaxial heterostructure by decreasing the thickness of the layers or by increasing the number of BTO-LCMO interfaces. Due to limited time, such experiments could not be performed.

# Bibliography


[1] A. Asamitsu, Y. Tomioka, H. Kuwahara, and Y. Tokura, Nature **388**, 50 (1997).

[2] A. Rebello and R. Mahendiran, Appl. Phys. Lett. **96**, 152504 (2010).

[3] R. Mohan, N. Kumar, B. Singh, N. K. Gaur, S. Bhattacharya, S. Rayaprol, A. Dogra, S. K. Gupta, S. J. Kim, and R. K. Singh, J. Alloys and Compd. **508**, L32 (2010).

[4] G. Catalan, Appl. Phys. Lett. **88**, 102902 (2006).

[5] M. P. Singh, W. Prellier, Ch. Simon, and B. Raveau, Appl. Phys. Lett. **87**, 022505 (2005).

[6] S.T. Mahmud. M. M. Saber, H. S. Alagoz, R. Bouveyron, J. Jung, and K.H. Chow, Appl. Phys. Lett. **100**, 072404 (2012).

[7] A. I. Abramovich, L. I. Koroleva and A. V. Michurin, J. Phys.: Condens. Matter **14** L537 (2002).

[8] A. Rebello, and R. Mahendiran, Appl. Phys. Lett. **93** 232501 (2008).

[9] H. S. Alagoz, I. Živković, S. T. Mahmud, M. M. Saber, G. Perrin, J. Shandro, M. Khan, Y. Zhang, M. Egilmez, J. Jung, and K. H. Chow, Phys. Status Solidi B, **250**, s2158 (2013).

# Works Cited


1. A. Asamitsu, Y. Tomioka, H. Kuwahara, and Y. Tokura, Nature **388**, 50 (1997).

2. A. A. Wagh, P. S. A. Kumar, H. L. Bhat, and S. Elizabeth, J. Appl. Phys. **108**, 063703 (2010).

3. A. Baena, L. Brey, and M. J. Calderón, Phys. Rev. B **83**, 064424 (2011).

4. A. I. Abramovich, L. I. Koroleva and A. V. Michurin, J. Phys.: Condens. Matter **14** L537 (2002).

5. A. I. Abramovich, L. I. Koroleva, A. V. Michurin, O. Y. Gorbenko, and A. R. Kaul, Physica B **293**, 38 (2000).

6. A. I. Kurbakov, A. V. Lazuta, V. A. Ryzhov, V. A. Trounov, I. I. Larionov, C. Martin, A. Maignan, and M. Hervieu, Phys. Rev. B **72**, 184432 (2005).

7. A. I. Kurbakov, A.V. Lazuta, and V. A. Ryzhov, J. Phys.: Conf. Ser. **200**, 012099 (2010).

8. A. I. Kurbakov, J. Magn. Magn. Mater. **322** 967 (2010).

9. A. J. Millis, Nature **392**, 147 (1998).

10. A. J. Millis, P. B. Littlewood, and B. I. Shraiman, Phys. Rev. Lett. **74**, 5144 (1995).

11. A. J. Millis, Phil. Trans. R. Soc. Lond. A **356**, 1473 (1998).

12. A. Kumar and J. Dho, J. Appl. Phys. **110**, 093901 (2011).

13. A. Odagawa, T. Kanno, H. Adachi, H. Sato, I. H. Inoue, H. Akoh, M. Kawasaki, and Y. Tokura, Thin Solid Films **486**, 75 (2005).

14. A. Rebello and R. Mahendiran, Appl. Phys. Lett. **94**, 112107 (2009).

15. A. Rebello and R. Mahendiran, Appl. Phys. Lett. **96**, 152504 (2010).

16. A. Rebello, and R. Mahendiran, Appl. Phys. Lett. **93** 232501 (2008).

17. A. S. Alexandrov, A. M. Bratkovsky, and V.V. Kabanov, Phys. Rev. Lett. **96**, 117003 (2006).

18. A. S. Alexandrov, and A. M. Bratkovsky, Phys. Rev. Lett. **82**, 141 (1999).

19. A. S. Carneiro, F. C. Fonseca, T. Kimura, and R. F. Jardim, J. Phys.: Condens. Matter **20**, 215203 (2008).

20. A. S. Carneiro, R. F. Jardim, and F.C. Fonseca, Phys. Rev. B **73**, 012410 (2006).

21. A. L. Meier, A.Y. Desai, L. Wang , T.J. Marks and B.W. Wessels, J. Mater. Res. **22**, 1384 (2007).

22. A.-M. H.-Gosnet, and J.-P. Renard, J. Phys. D: Appl. Phys. **36**, R127 (2003).

23. B. Fisher, J. Genossar, K. B. Chashka, L. Patlagan, and G. M. Reisner, Appl. Phys. Lett. **88**, 152103 (2006).

24. B. Naik, and R. Mahendiran, J. Appl. Phys. **110**, 053915 (2011).

25. C. A. F. Vaz, J. Phys.: Condens. Matter. **24**, 333201 (2012).

26. C. A. F. Vaz, J. Hoffman, Y. Segal, J.W. Reiner, R. D. Grober, Z. Zhang, C. H. Ahn, and F. J. Walker, Phys. Rev. Lett. **104**, 127202 (2010).

27. C. B. Sawyer and C. H. Tower, Phys. Rev. Phys. **35**, 269 (1935).

28. C. Hao, B. Zhao, G. Kuang, and Y. Sun , Phys. Status Solidi B **248**, 2921 (2011).

29. C. Martin, A. Maignan, M. Hervieu, and B. Raveau, Phys. Rev. B **60**, 12191 (1999).

30. C. Zener, Phys. Rev. B **82**, 403 (1951).

31. D. Damjanovic, Rep. Prog. Phys. **61**, 1267 (1998).

32. D. Khomskii, and L. Khomskii, Phys. Rev. B **67**, 052406 (2003).

33. D. Khomskii, Physics **2**, 20 (2009).

34. I. D. Luzyanin, V. A. Ryzhov, D. Yu. Chernyshov, A. I. Kurbakov, V. A. Trounov, A. V. Lazuta, V. P. Khavronin, I. I. Larionov, and S. M. Dunaevsky, Phys. Rev. B **64**, 094432 (2001).

35. D. Niebieskikwiat, J. Tao, J. M. Zuo, and M. B. Salamon, Phys. Rev. B **78**, 014434 (2008).

36. E. Dagotto, T. Hotta, and A. Moreo, Phys. Rep. **344**, 1 (2001).

37. E. Rozenberg, V. Markovich, Ya. Yuzhelevskii, G. Gorodetsky and M. Ziese, J. Appl. Phys. **95**, 7103 (2004).

38. Y. F. Chen, M. Ziese, and P. Esquinazi, Appl. Phys. Lett. **88**, 222513 (2006).

39. F. Rivadulla, M. A. López-Quintela, and J. Rivas, Phys. Rev. Lett. **93**, 167206 (2004).

40. K. F. Wang, Y. Wang, L. F. Wang, S. Dong, D. Li, Z. D. Zhang , H. Yu, Q. C. Li, and J.-M. Liu, Phys. Rev. B **73**, 134411 (2006).

41. F. Yen, C. dela Cruz, B. Lorenz, E. Galstyan, Y. Y. Sun, M. Gospodinov, and C. W. Chu, J. Matter. Res. **22**, 2163 (2007).

42. G. Catalan, and J. F. Scott, Nature **448**, doi:10.1038/nature06156 (2007).

43. G. Catalan, Appl. Phys. Lett. **88**, 102902 (2006).

44. I. G. Deac, S. V. Diaz, B. G. Kim, S.-W. Cheong, and P. Schiffer, Phys. Rev. B **65**, 174426 (2002).

45. N. G. Kim, Y. S. Koo, C. J. Won, N. Hur, J. H. Jung, J. Yoon, Y. Jo, and M. H. Jung, J. Appl. Phys. **102**, 014107 (2007).

46. G. Singh-Bhalla, A. Biswas, and A. F. Hebard, Phys. Rev. B **80**, 144410 (2009).

47. G. Srinivasan, E. T. Rasmussen, J. Gallegos, R. Srinivasan, Yu. I. Bokhan, and V. M. Laletin, Phys. Rev. B **64**, 214408 (2001).

48. G. Y. Wang, X. H. Chen, T. Wu, X. G. Luo, W. T. Zhang, and G. Wu, Phys. Rev. Lett. **100**, 146402 (2008).

49. J. B. Goodenough, J. Appl. Phys. **81**, 5330 (1997).

50. H. Béa, M. Gajek, M. Bibes, and A. Barthélémy, J. Phys.: Condens. Matter. **20**, 434221 (2008).

51. H. Jain and A. K. Raychaudhuri, Appl. Phys. Lett. **93**, 182110 (2008).

52. G. H. Kwei, A. C. Lawson, S. J. L. Billinge and S.-W. Cheong, J. Phys. Chem. **97**, 2368 (1993).

53. H. Lu, T. A. George, Y. Wang, I. Ketsman, J. D. Burton, C.-W. Bark, S. Ryu, D. J. Kim, J. Wang, C. Binek, P. A. Dowben, A. Sokolov, C.-B. Eom, E. Y. Tsymbal, and A. Gruverman, Appl. Phys. Lett. **100**, 232904 (2012).

54. H. S. Alagoz, I. Živković, S. T. Mahmud, M. M. Saber, G. Perrin, J. Shandro, M. Khan, Y. Zhang, M. Egilmez, J. Jung, and K. H. Chow, Phys. Status Solidi B, **250**, s2158 (2013).

55. H. Sakai and Y.Tokura, Appl. Phys. Lett. **92**, 102514 (2008).

56. H. Sakai, K. Ito, T. Nishiyama, X. Yu, Y. Matsui, S. Miyasaka, and Y.Tokura, J. Phy. Soc. Jpn. **77**, 124712 (2008).

57. W. H. Shah, and S. K. Hasanain, J. Appl. Phys. **108**, 113907 (2010).

58. H. H. Wieder, Phys. Rev. **99**, 1161 (1955).

59. J. C. Loudon, N. D. Mathur, and P. A. Midgley, Nature **420**, 797 (2002).

60. J. Klein, J. B. Philipp, G. Carbone, A. Vigliante, L. Alff, and R. Gross, Phys. Rev. B **66**, 052414 (2002).

61. J. Ma , J. M. Hu , Z. Li , and C.-W. Nan, Adv. Mater.**23**, 1062 (2011).

62. J. Tao, D. Niebieskikwiat, M. B. Salamon, and J. M. Zuo, Phys. Rev. Lett. **94**, 147206 (2005).

63. J.-S. Zhou, J. B. Goodenough, A. Asamitsu, and Y. Tokura, Phys. Rev. Lett. **79**, 3234 (1997).

64. J.-W. Cai, C. Wang, B.-G. Shen, J.-G. Zhao, and W.-S Zhan, Appl. Phys. Lett. **71**, 1727 (1997).

65. J.-Z. Wang, J.-R. Sun, Q.-Y. Dong, G.-J. Liu, B.-G. Shen, Solid State Commun. **149**, 325 (2009).

66. K. A. Shaykhutdinov, D. A. Balaev, S. V. Semenov, S. I. Popkov, A. A. Dubrovskiy, N. V. Sapronova and N. V. Volkov, J. Phys. D: Appl. Phys. **44**, 255001 (2011).

67. K. Dörr, J. Phys. D: Appl. Phys., **39**, R125 (2006).

68. K. Kinoshita, and A. Yamaji, J. Appl. Phys. **47**, 371 (1976).

69. K. Seshan, Handbook of Thin-film Deposition Process and Techniques, Noyes Publications, (2002).

70. P. K. Siwach, H. K. Singh, and O. N. Srivastava1, J. Phys.: Condens. Matter **20**, 273201 (2008).

71. L. Abad, V. Laukhin, S. Valencia, A. Gaup, W. Gudat, L. Balcells, and B. Martinez, Adv. Funct. Mater. **17**, 3918 (2007).

72. Y. L. Chang, Q. Huang, and C. K. Ong, J. Appl. Phys. **91**, 789 (2002).

73. L. Ghivelder, and F. Parisi, Phys. Rev. B **71**, 184425 (2005).

74. L. Ghivelder, R. S. Freitas, M. G. das Virgens, M. A. Continentino, H. Martinho, L. Granja, M. Quintero, G. Leyva, P. Levy, and F. Parisi, Phys. Rev. B **69**, 214414 (2004).

75. L. Hu, Y. P. Sun, B. Wang, Z. G. Sheng, X. Luo, X. B. Zhu, Z. R. Yang, W. H. Song, J. M. Dai, Z. Z. Yin, and W. B. Wu, J. Appl. Phys. **106**, 083903 (2009).

76. L. K. Leung, A. H. Morrish, and B. J. Evans, Phys. Rev. B **13**, 4069 (1976).

77. C. L. Lu, X. Chen, S. Dong, K. F. Wang, H. L. Cai, D. Li, Z. D. Zhang and J.-M. Liu, Phys. Rev. B **79**, 245105 (2009).

78. L. Zhang, C. Israel, A. Biswas, R. L. Greene, and A. de Lozanne, Science **298**, 805 (2002).

79. J. M. Barandiarán, F. J. Bermejo, J. Gutiérrez, and L. F. Baquín, Journal of Non-crystalline Solids **353**, 757 (2007).

80. M. Clausse, Colloid & Polymer Sci. **253**, 1020 (1975).

81. M. Coey, Nature **430**, 155 (2004).

82. M. Egilmez, I. Isaac, D. D. Lawrie, K. H. Chow, and J. Jung, J. Mater. Chem. **18**, 5796 (2008).

83. M. Egilmez, K.H. Chow, and J.A. Jung, Mod. Phys. Lett. B, **25**, 697 (2011).

84. M. Egilmez, K.H. Chow, J. Jung, and Z. Salman, Appl. Phys. Lett., **90**, 162508 (2007).

85. M. Egilmez, M. Abdelhadi, Z. Salman, K. H. Chow, and J. Jung, Appl. Phys. Lett. **95** 112505 (2009).

86. M. Egilmez, M. M. Saber, A. I. Mansour, R. Ma, K. H. Chow, and J. Jung, Appl. Phys. Lett. **93**, 182505 (2008).

87. M. Egilmez, M. M. Saber, M. Abdelhadi, K. H. Chow, and J. Jung, Phys. Lett. A **375**, 4049 (2011).

88. M. H. Burkhardt, M. A. Hossain, S. Sarkar, Y.-D. Chuang, A. G. C. Gonzalez, A. Doran, A. Scholl, A. T. Young, N. Tahir, Y. J. Choi, S.-W. Cheong, H. A. Dürr, and J. Stöhr, Phys. Rev. Lett. **108**, 237202 (2012).

89. M. K. Srivastava, M. P. Singh, A. Kaur, F. S. Razavi, and H. K. Singh, J. Appl. Phys. **110** 123922 (2011).

90. M. K. Srivastava, M. P. Singh, P. K. Siwach, A. Kaur , F. S. Razavi , H. K. Singh, Solid State Commun., **152** 138 (2012).

91. M. M. Saber, M. Egilmez, A. I. Mansour, I. Fan, K. H. Chow, and J. Jung, Phys. Rev. B **82**, 172401 (2010).

92. M. M. Vijatović, J. D. Bobić, B. D. Stojanović, Science of Sintering, **40**, 235 (2008).

93. M. Nikolo, Am. J. Phys. **63**, 57 (1995).

94. M. Ohring, Material Science of Thin Films, Academic Press (2002).

95. M. P. Singh, W. Prellier, Ch. Simon, and B. Raveau, Appl. Phys. Lett. **87**, 022505 (2005).

96. M. Quintero, F. Parisi, G. Leyva, and L. Ghivelder, J. Phys.: Condens. Matter **20**, 345204 (2008).

97. M. Sirena, L. B. Steren, and J. Guimpel, Phys. Rev. B **64**, 104409 (2001).

98. M. Uehara, and S.-W. Cheong, Europhys. Lett. **52**, 674 (2000).

99. M. Uehara, S. Mori, C. H. Chen, and S.-W. Cheong, Nature **399**, 560 (1999).

100. N. Kambhala, P. Viswanath, and S. Angappane, Appl. Phys. Lett. **103** 102408 (2013).

101. N. Kozlova, K. Dörr, D. Eckert, A. Handstein, Y. Skourski, T. Walter, K.-H. Müller, and L. Schultz , J. Appl. Phys. **93**, 8325 (2003).

102. N. L. Guo, J. Li, Y. F. Wei, Y. Zhang, L. M. Cui, L. Zhao, Y. R. Jin, H. Y. Tian, Hui Deng, G. P. Zhao, and D. N. Zheng, J. Appl. Phys. **112**, 013907 (2012).

103. C. N. R. Rao and P. V. Vanitha, Curr. Opin. Solid State Mater. Sci. **6**, 97 (2002).

104. C. N. R. Rao, J. Phys. Chem. B, **104**, 5877 (2000).

105. N. S. Bingham, P. J. Lampen, T. L. Phan, M. H. Phan, S. C. Yu, and H. Srikanth, J. Appl. Phys. **111** 07D705 (2012).

106. O. Z. Yanchevskii, O. I. V'yunov, A. G. Belous, and A. I. Tovstolytkin, Low Temp. Phys. **32**, 134 (2006).

107. C. P. Adams, J. W. Lynn, Y. M. Mukovskii, A. A. Arsenov, and D. A. Shulyatev, Phys. Rev. Lett. **85**, 3954 (2000).

108. P. Levy, F. Parisi, L. Granja, E. Indelicato, and G. Polla, Phys. Rev. Lett. **89**, 137001 (2002).

109. P. Murugavel, D. Saurel, W. Prellier, Ch. Simon, and B. Raveau, Appl. Phys. Lett. **85**, 4424 (2004).

110. P.T. Phong, D.H.Manh, N.V.Dang, L.V.Hong, and I.J.Lee, Physica B **407**, 3774 (2012).

111. R. A. Lewis, Appl. Phys. Lett. **92** 184102 (2008).

112. S. R. Bakaul, B. F. Miao, W. Lin, W. Hu, A. David, H. F. Ding, and T. Wu, Appl. Phys. Lett. **101**, 012408 (2012).

113. R. Mohan, N. Kumar, B. Singh, N. K. Gaur, S. Bhattacharya, S. Rayaprol, A. Dogra, S. K. Gupta, S. J. Kim, and R. K. Singh, J. Alloys and Compd. **508**, L32 (2010).

114. R. Ramesh, and N. A. Spaldin, Nature Mater. **6**, 21 (2007).

115. P. S. Devi, A. Kumar, D. Bhattacharyay, S. Karmakar, and B. K. Chaudhuri, Jpn. J. Appl. Phys. **49** 083001 (2010).

116. R. S. Freitas, L. Ghivelder,F. Damay, F. Dias, and L. F. Cohen, Phys. Rev. B **64**, 144404 (2001).

117. S. D. Bhame, V. L. J. Joly, and P. A. Joy , Phys. Rev. B **72**, 054426 (2005).

118. S. Hébert, A. Maignan, C. Martin, and B. Raveau, Solid State Commun. **121**, 229 (2002).

119. S. M. Yusuf, M. Sahana, M. S. Hegde, K. Dörr, and K.-H. Müller , Phys. Rev. B **62**, 1118 (2000).

120. S. Mercone, R. Frésard, V. Caignaert, C. Martin, D. Saurel, C. Simon, G. André, P. Monod, and F. Fauth, J. Appl. Phys. **98**, 023911 (2005).

121. S. Mori, C. H. Chen, and S.-W. Cheong, Nature **392**, 473 (1998).

122. S. T. Mahmud, M. M. Saber, H. S. Alagoz, J. Jung, and K. H. Chow, J. Phys. Chem. Solids **74**, 1865 (2013).

123. S. T. Mahmud, M. M. Saber, H. S. Alagoz, K. Biggart, R. Bouveyron, Mahmud Khan, J. Jung, and K. H. Chow, Appl. Phys. Lett. **100**, 232406 (2012).

124. S. T. Mahmud. M. M. Saber, H. S. Alagoz, R. Bouveyron, J. Jung, and K.H. Chow, Appl. Phys. Lett. **100**, 072404 (2012).

125. S. Y. Wang, and J. Gao, EPL **97** 57009 (2012).

126. S. Yang, S. Dong, Y. Liu, Y. Yao, Y. Yin, and X. Li, J. Appl. Phys. **114**,034102 (2013).

127. S.-W. Cheong, and M. Mostovoy, Nature Mater.**6**, 13 (2007).

128. T. Chatterji, Colossal Magnetoresistive Manganites, Kluwer Academic Publishers, (2004).

129. T. Wu, S. B. Ogale, J. E. Garrison, B. Nagaraj, A. Biswas, Z. Chen, R. L. Greene, R. Ramesh, T. Venkatesan, and A. J. Millis, Phys. Rev. Lett. **86**, 5998 (2001).

130. V. S. Kumar, and R. Mahendiran, J. Appl. Phys. **109**, 023903 (2011).

131. V. Y. Ivanov, A. A. Mukhin, A. S. Prokhorov, and A. M. Balbashov, Phys. Status Solidi B **236**, 445 (2003).

132. X. J. Chen, H.-U. Habermeier, and C. C. Almasan, Phys. Rev. B **68**, 132407 (2003).

133. Y. M. Xiong, G. Y. Wang, X. G. Luo, C. H. Wang, X. H. Chen, X. Chen and C. L. Chen, J. Appl. Phys. **97**, 083909 (2005).

134. Y. Murakami, H. Kasai, J. J. Kim, S. Mamishin, D. Shindo, S. Mori, and A. Tonomura, Nature Nanotechnology **5**, 37 (2010).

135. Y. Nishi, Current Applied Physics **11**, e101 (2011).

136. Y. Tokura and N. Nagaosa, Science **288**, 462 (2000).

137. Y. Tokura, Rep. Prog. Phys. **69** 797 (2006).

138. Y. Tomioka, H. Hiraka, Y. Endoh, and Y. Tokura, Phys. Rev. B **74**,104420 (2006).

139. Y. Tomioka, X. Z. Yu, T. Ito, Y. Matsui, and Y.Tokura, Phys. Rev. B **80**, 094406 (2009).

140. Y. Tomioka, Y. Okimoto, J. H. Jung, R. Kumai, and Y. Tokura, Phys. Rev. B **68**, 094417 (2003).

141. Y. Yamato, M. Matsukawa, Y. Murano, R. Suryanarayanan, S. Nimori, M.Apostu, A. Revcolevschi, K. Koyama, and N. Kobayashi, Appl. Phys. Lett. **94**, 092507 (2009).

142. Y. Ying, J. Fan, L. Pi, Z. Qu, W. Wang, B. Hong, S. Tan, and Y. Zhang, Phys. Rev. B **74**, 144433 (2006).

143. Y.-D. Chuang, A. D. Gromko, D. S. Dessau, T. Kimura, and Y. Tokura, Science **292**, 5521 (2001).

144. Z. Huang, G. Gao, F. Zhang, X. Feng, L. Hu, X. Zhao, Y. Sun, W. Wua, J. Magn. Magn. Mater. **322** 3544 (2010).